LUND UNIVERSITY

Microfluidic Preparation and Transport of Long DNA using Pillar Arrays

Ström, Oskar

2023

Microfluidic Preparation and Transport of Long DNA using Pillar Arrays

OSKAR STRÖM
DIVISION OF SOLID STATE PHYSICS | FACULTY OF ENGINEERING | LUND UNIVERSITY

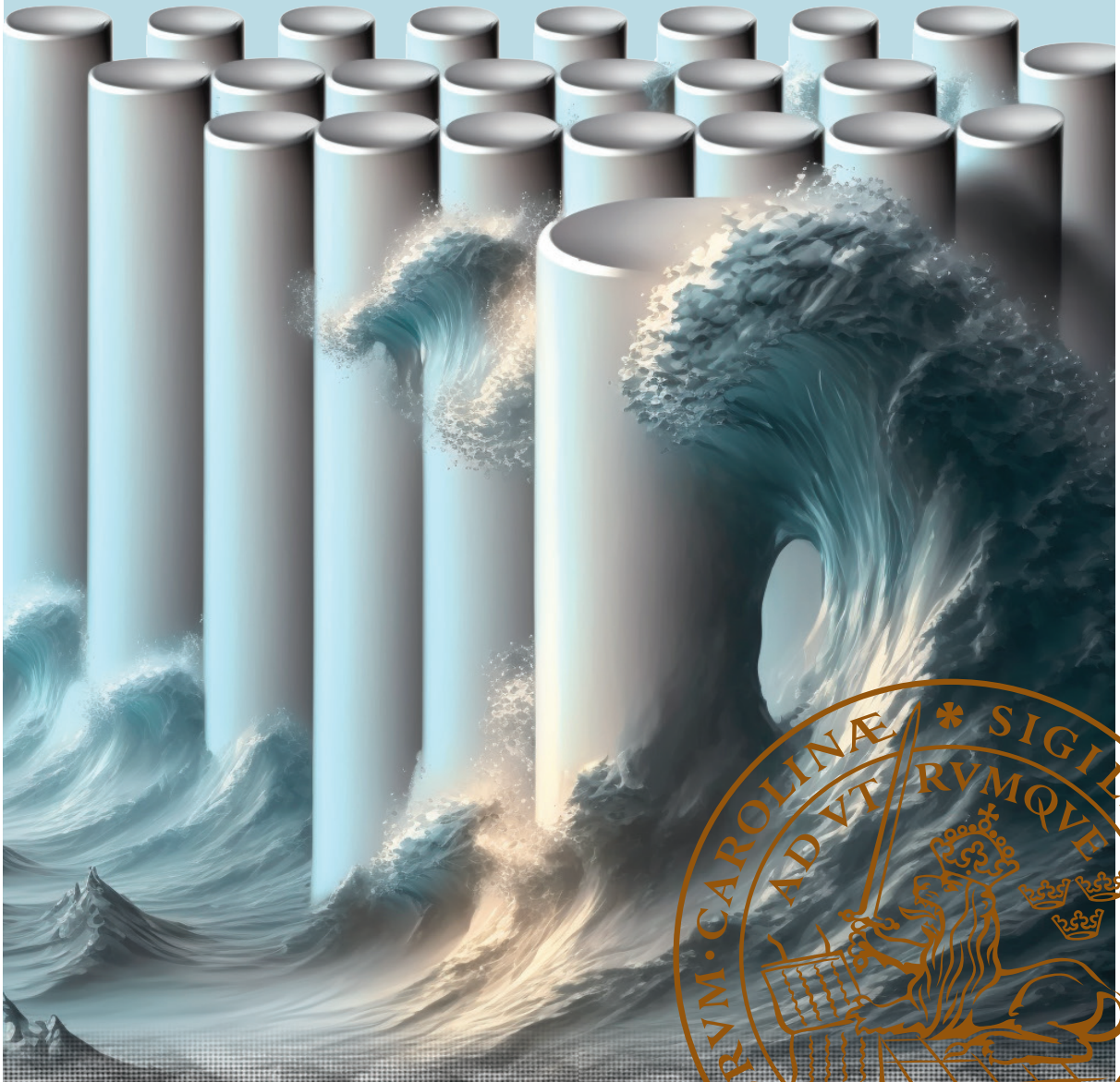

Printed by Media-Tryck, Lund 2023 NORDIC SWAN ECOLABEL 3041 0903

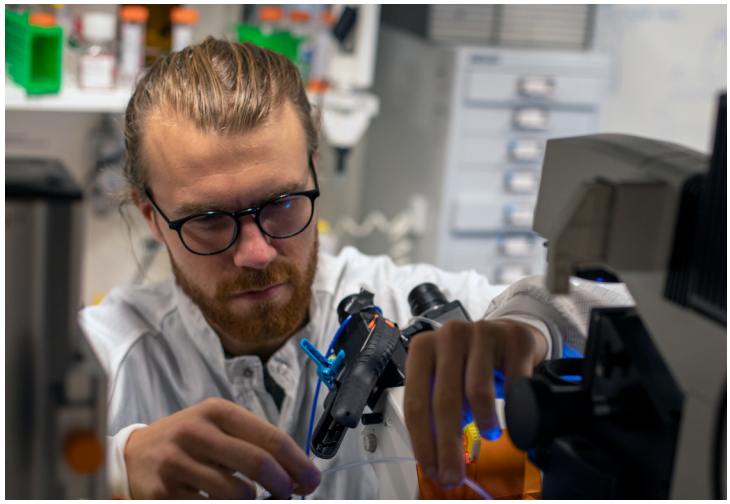

Modern sequencing technology has revolutionized the availability of genomic data. This thesis is about improving its sample preparation as it has long been an important bottleneck. Both about developing cheaper, faster and more automatized tools but also about understanding new physical phenomena that arise when using the tools.

LUND UNIVERSITY

Faculty of Engineering
Department of Physics
Division of Solid State Physics

ISBN 978-91-8039-389-8

Microfluidic Preparation and Transport of Long DNA using Pillar Arrays

Oskar Ström

LUND
UNIVERSITY

DOCTORAL DISSERTATION

Doctoral dissertation for the degree of Doctor of Philosophy (PhD) at the Faculty of Engineering at Lund University to be publicly defended on Friday February 10th 2023 at 09.15 in Rydbergssalen, Department of Physics, Sölvegatan 14.

Faculty opponent
Kevin Dorfman, University of Minnesota, Minneapolis, MN, USA

Organization LUND UNIVERSITY	**Document name** Doctoral Thesis
	Date of issue 2023-02-10
Author(s) Oskar Ström	Sponsoring organization

Title and subtitle

Microfluidic Preparation and Transport of Long DNA using Pillar Arrays

Abstract

This thesis presents a set of microfluidic tools and experimental studies for preparing (> 20 kbp) for genetic analysis as well as the transport of high-concentration, long-DNA solutions in pillar arrays.

Long-DNA sample preparation with conventional gel-based techniques is slow (tens of hours to days) and laborious. If size-selective separation is to be achieved, it is also expensive. Long-DNA preparation is essential for detecting genetic sequences that ranges above kilobase pairs such as large scale structural variations. These can in turn be important for diagnosing genetic diseases.

Deterministic lateral displacement (DLD) has been used to prepare the long DNA. DLD is a continuous microfluidic separation method. Long-DNA separation in DLD has previously been thought to be limited to very low flow velocities (up to 40 µm/s) and thus low throughput. In this work, we show that it is possible to displace long DNA up to a mean flow velocity of approximately 34 mm/s. This increases the separation throughput immensely (one to five orders of magnitude in throughput compared to other microfluidic techniques) which makes it possible to collect enough separated sample after a few minutes to hours, depending on the post-separation analysis method. We explore the effect of high concentration and show that long-DNA separation can both be enhanced and lessened as a consequence of concentration-based effects. We also integrate long-DNA isolation in DLD with subsequent surface stretching of the isolated DNA molecules. Combining the analysis on-chip after the separation eliminates any problematic sample transfer steps and allows the analysis to work with dilute samples of only a few hundred molecules.

Novel elastic flow phenomena have been discovered. Large-scale ordered regular DNA waves have been observed to emerge in pillar arrays when trying to increase the throughput of DNA separation in DLD. It is possible that these waves could either improve separation or worsen it and thus set the limits for it. A large part of the presented work aimed to understand the emergence and character of these waves. The peaks of these waves consist of high local DNA concentration with the DNA strands stretched and oriented with the wave fronts. These have been found to occur at high flow velocity, u, and high concentration to overlap concentration ratio (C/C^*). We have explored the wave onset in C/C^* and u by changing the polymer length, concentration and ionic strength of the buffer. These waves arise together with periodic cycles of growth and shedding of masses of DNA that collect in the pillar gaps in the flow direction.

We also show that the macroscopic and microscopic DNA flow patterns in micro pillar arrays depend highly on the pillar distribution and the pillar shape. By changing the pillar array distribution to hexagonal instead of quadratic, large-scale chaotic zig-zag patterns are observed. By changing the distribution to a disordered one, no large-scale flow pattern is observed. We speculate that the induction or avoiding of a large-scale flow pattern could be useful for different degrees of mixing. By changing the pillar shape from circular cross-section to a triangular one, we form large waves of only one orientation instead of two. The large waves appear in a different orientation depending on the flow direction. In addition, the microscopic vortex behavior emerges at different flow velocities for the two directions as well as with different flow resistances. This could be exploited in microfluidic components such as one-way valves or pumps.

Key words

Long-DNA Separation, Sample Preparation, Microfluidics, Micropillar Arrays, Elastic Turbulence

Classification system and/or index terms (if any)

Supplementary bibliographical information	**Language** English
ISSN and key title	**ISBN** 978-91-8039-389-8 (print) 978-91-8039-390-4 (pdf)
Recipient's notes	**Number of pages** Price
	Security classification

Signature  Date 2023-12-21

Microfluidic Preparation and Transport of Long DNA using Pillar Arrays

Oskar Ström

LUND
UNIVERSITY

Front cover: Fluorescent micrograph of DNA Waves in a Quadratic Array melting into an artistic illustration of water waves in a pillar array. The artistic illustration has been generated with Midjourney.

Back cover: The author (Oskar Ström) working in his lab with the fluorescent microscope. Photographer: Jason Beech.

Division of Solid State Physics
Department of Physics
Faculty of Engineering
Lund University

ISBN 978-91-8039-389-8 (print)
ISBN 978-91-8039-390-4 (pdf)

Printed in Sweden by Media-Tryck, Lund University
Lund 2023

This too shall pass

Abstract

This thesis presents a set of microfluidic tools and experimental studies for preparing long DNA (> 20 kbp) for genetic analysis as well as the transport of high-concentration long-DNA solutions in pillar arrays.

Long-DNA sample preparation with conventional gel-based techniques is slow (tens of hours to days) and laborious. If size-selective separation is to be achieved, it is also expensive. Long-DNA preparation is essential for detecting genetic sequences that ranges above kilobase pairs such as large-scale structural variations. These can in turn be important for diagnosing genetic diseases.

Deterministic lateral displacement (DLD) has been used to prepare the long DNA. DLD is a continuous microfluidic separation method. Long DNA separation in DLD has previously been thought to be limited to very low flow velocities (up to 40 μm/s) and thus low throughput. In this work, we show that it is possible to displace long DNA up to a mean flow velocity of approximately 34 mm/s. This increases the separation throughput immensely (one to five orders of magnitude in throughput compared to other microfluidic techniques) which makes it possible to collect enough separated sample after a few minutes to hours, depending on the post-separation analysis method. We explore the effect of high concentration and show that long-DNA separation can both be enhanced and lessened as a consequence of concentration-based effects. We also integrate long-DNA isolation in DLD with subsequent surface stretching of the isolated DNA molecules. Combining the analysis on-chip after the separation eliminates any problematic sample transfer steps and allows the analysis to work with dilute samples of only a few hundred molecules.

Novel elastic flow phenomena have been discovered. Large-scale ordered regular DNA waves have been observed to emerge in pillar arrays when trying to increase the throughput of DNA separation in DLD. It is possible that these waves could either improve separation or worsen it and thus set the limits for it. A large part of the presented work aimed to understand the emergence and character of these waves. The peaks of these waves consist of high local DNA concentration with the DNA strands stretched and oriented with the wave fronts. These have been found to occur at high flow velocity, u, and high concentration to overlap concentration ratio (C/C^*). We have explored the wave onset in C/C^* and u by changing the polymer length, concentration and ionic strength of the buffer. These waves arise

together with periodic cycles of growth and shedding of masses of DNA that collect in the pillar gaps in the flow direction.

We also show that the macroscopic and microscopic DNA flow patterns in micro pillar arrays depend highly on the pillar distribution and the pillar shape. By changing the pillar array distribution to hexagonal instead of quadratic, large-scale chaotic zig-zag patterns are observed. By changing the distribution to a disordered one, no large-scale flow pattern is observed. We speculate that the induction or avoiding of a large-scale flow pattern could be useful for different degrees of mixing. By changing the pillar shape from circular cross-section to a triangular one, we form large waves of only one orientation instead of two. The large waves appear in a different orientation depending on the flow direction. In addition, the microscopic vortex behavior emerges at different flow velocities for the two directions as well as with different flow resistances. This could be exploited in microfluidic components such as one-way valves or pumps.

Graphical Abstract

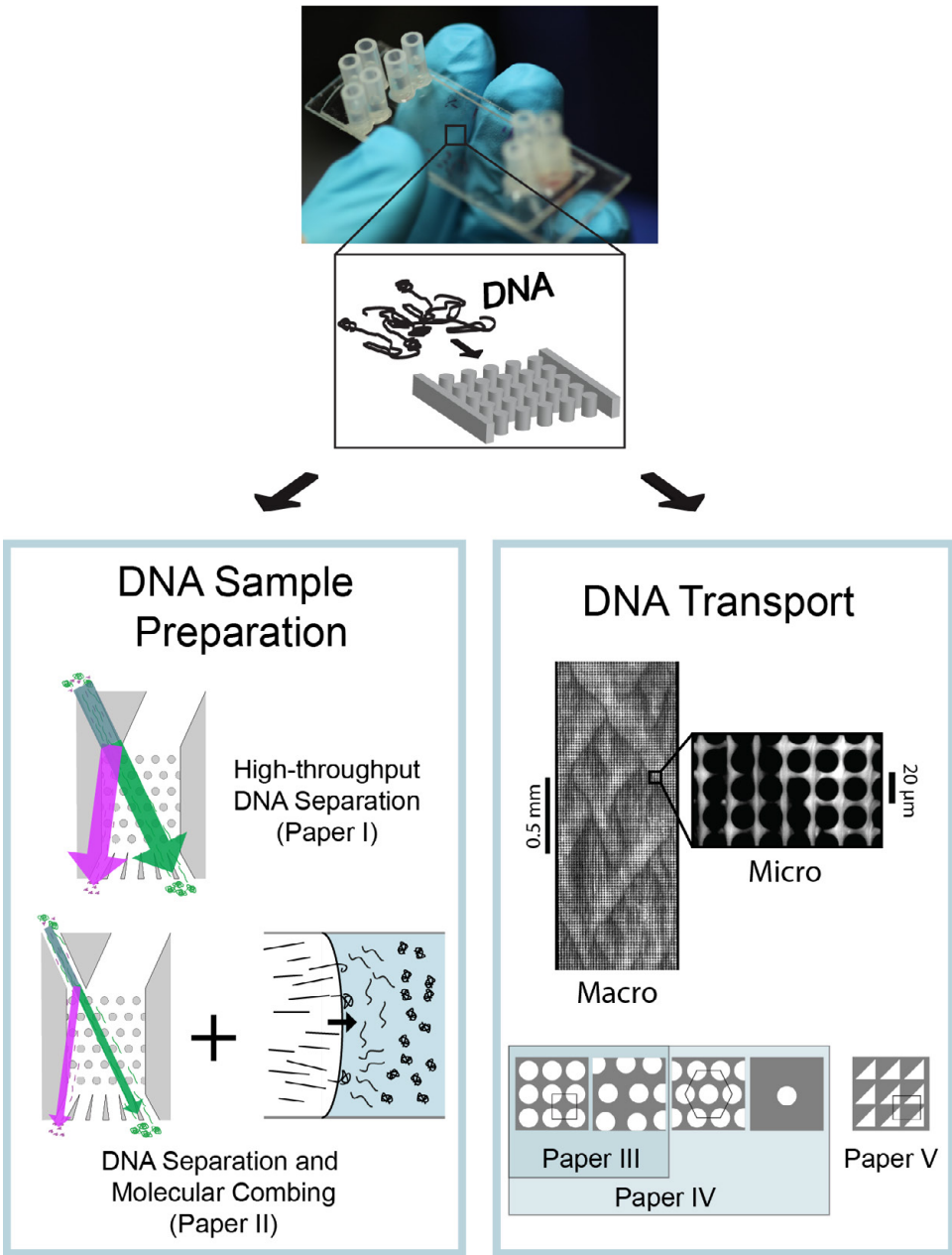

Populärvetenskaplig sammanfattning på svenska

I mitt arbete har jag studerat rörelsen hos deoxiribonukleinsyra eller DNA. DNA är en polymer, d.v.s. det är en lång kedja av mindre enheter, som för DNA kallas för baspar. I varje av dina ca 30 triljoner celler finns ca 2×3 miljarder av dessa baspar [1]. Längden DNA från en cell är hela 2 m då varje baspar är ca 0.34 nm långt. Detta motsvarar ca 200 tur och retur-resor till solen för allt DNA i hela din kropp.

Genom att ta reda på din DNA-sekvens kan vi ta reda på information om din biologi. Vi kan ta reda på om du har några genetiska sjukdomar eller vilken genetisk risk du har för ärftliga sjukdomar. Genom att analysera mikroorganismers DNA kan vi ta reda på vilken sort det är och vad för slags gener de bär på. Det är viktigt att ta reda på hur farliga mikrorganismer som infekterat din kropp är för att kunna ge en så snabb och effektiv behandling som möjligt. Mikroorganismerna kanske är resistenta mot antibiotika eller andra mediciner. Om så vore fallet kan man istället behandla dig med andra läkemedel.

Det är därmed viktigt att ha verktyg som snabbt kan ta reda på vad för gener du eller inkräktande mikrober bär på. Problemet är att dagens metoder är för långsamma. I många fall krävs cellodling eller DNA kopiering, t. ex. polymeraskedjereaktion (PCR). I mitt arbete fokuserar jag på långa DNA trådar. Det är trådar längre än 20 kbp eller ca 7 mikrometer, motsvarande ca 14 gånger kortare än bredden av ett genomsnittligt hårstrå. I nuläget så förbereds prover för lång DNA i geler där olika långa DNA rör sig olika snabbt. Den tekniken är långsam (ca 24 timmar), är dyr, fungerar bara med mycket DNA prov och kräver mycket manuellt arbete.

I detta arbete hanterar jag DNA-trådarna med hjälp av mikrofluidik. I mikrofluidik manipulerar man ämnen i mikroskopiska kanaler i chip gjorde av plast, gummi eller glas, i storleksordningen av ett hårstrås bredd, tillverkade med hjälp av avancerad renrumsteknik. Genom att utnyttja små dimensioner behöver vi inte använda så mycket prov eller spendera så mycket material på instrumenten. Genom massproduktion kan de små chippen bli riktigt billiga och tillgängliga för alla. De går att automatisera och de är i de flesta fall mycket snabba då proven bara behöver röra sig eller reagera över mycket små avstånd i kanalerna. Då

chippen är små och portabla kan de användas på plats, i hemmet eller ute i fält, precis som ett graviditetstest eller ett covid19-antigentest. Man behöver då inte längre skicka in sina prover för analys i ett centraliserat labb. Mikrofluidik-utvecklingen jämförs ibland med datorrevolutionen. Komponenterna för datorerna har blivit ofantligt mycket mindre och datorerna som följd har blivit miljontals gånger kraftfullare och snabbare. Förr så tog en dator upp ett helt rum. Nu får man plats med en i sin byxficka. Samma sak kan nu komma att ske med medicinsk teknik.

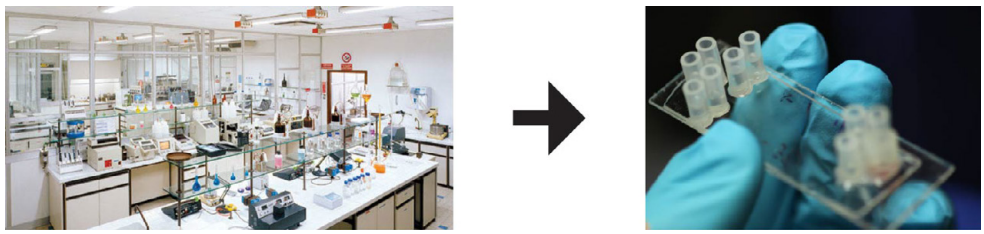

Medicinrevolutionen där instrument och personal i ett centraliserat lab övergår till små, bärbara mikrofluidiska chip. Den vänstra bilden är tagen av ett kemilab, reproducerad med tillåtelse av UCLA. Den högra bilden är en av chippen jag tillverkat i labbet.

I mitt avhandling presenterar jag mina resultat där jag använt mikrofluidik för att manipulera DNA. Jag har fokuserat mitt arbete på sortering av DNA molekyler efter molekyllängd. Jag har även kombinerat DNA sortering med efterföljande utsträckning på en yta, ett sätt för att kunna läsa av DNA-generna direkt i mikroskop.

När jag försökte sortera mer prov på kortare tid upptäckte jag underliga vågor (se bokens framsida). Vi i forskningsgruppen var häpna och hade aldrig sett något liknande i forskarlitteraturen. Dessa vågor var så spännande så jag lade andra hälften av mina doktorandstudier på att studera dem på olika sätt. Vågorna uppkommer när hundratals små virvlar, fyllda av DNA, frigörs från utrymmet mellan pelare och interagerar med varandra. Vågtopparna består av hög koncentration av utsträckta DNA-trådar, riktade längs med vågens färdriktning. Vågorna kan vara både nyttiga och användbara för t.ex. blandning av prov eller vara något att undvika för exempelvis sortering. Det är därför viktigt att kartlägga under vilka förhållanden de bildas.

Referenser

1. Sender, R., S. Fuchs, and R. Milo, Revised estimates for the number of human and bacteria cells in the body. PLoS biology, 2016. 14(8): p. e1002533.

List of Publications

The most important parts of the work of this thesis are described in the following manuscripts (denoted Papers I–V in the text). Note that the papers are listed by subject and not chronologically. The author contribution statements have been written according to CRediT (Contributor Roles Taxonomy), see credit.niso.org for role descriptions.

I. High-throughput Separation of Long DNA in Deterministic Lateral Displacement Arrays

Oskar E. Ström, Jason P. Beech, and Jonas. O. Tegenfeldt

Micromachines, 2022. **13**(10): p. 1754.

Conceptualization, O.E.S., J.P.B., and J.O.T.; Data Curation, O.E.S.; Formal Analysis, O.E.S.; Funding Acquisition, J.O.T.; Investigation, O.E.S.; Methodology, O.E.S., J.P.B., and J.O.T.; Project Administration, J.O.T.; Resources, J.O.T.; Software, O.E.S.; Supervision, J.P.B., and J.O.T.; Validation, O.E.S., J.P.B., and J.O.T.; Visualization, O.E.S., J.P.B., and J.O.T.; Writing - Original Draft, O.E.S., J.P.B., and J.O.T.; Writing - Reviewing & Editing, O.E.S., J.P.B., and J.O.T.

II. Long DNA Isolation and Imaging using Lateral Displacement Arrays Integrated with DNA combing

Oskar E. Ström, Jason P. Beech, and Jonas. O. Tegenfeldt

Extended abstract at 23rd International Conference on Miniaturized Systems for Chemistry and Life Sciences, MicroTAS 2019 (pp. 771-772).

Conceptualization, O.E.S., J.P.B., and J.O.T.; Data Curation, O.E.S; Formal Analysis, O.E.S.; Funding Acquisition, J.O.T.; Investigation, O.E.S., and J.P.B.; Methodology, O.E.S., J.P.B., and J.O.T.; Project Administration, J.O.T.; Resources, J.O.T.; Software, O.E.S.; Supervision, J.P.B., and J.O.T.; Validation, O.E.S., J.P.B., and J.O.T.; Visualization, O.E.S., J.P.B., and J.O.T.; Writing - Original Draft, O.E.S., J.P.B., and J.O.T.; Writing - Reviewing & Editing, O.E.S., J.P.B., and J.O.T.

III. Short and Long-range Cyclic Patterns in Flows of DNA Solutions in Microfluidic Obstacle Arrays

Oskar E. Ström, Jason P. Beech, and Jonas. O. Tegenfeldt

Submitted for publication (2022)

Conceptualization, O.E.S., J.P.B., and J.O.T.; Data Curation, O.E.S; Formal Analysis, O.E.S.; Funding Acquisition, J.O.T.; Investigation, O.E.S., and J.P.B.; Methodology, O.E.S., J.P.B., and J.O.T.; Project Administration, J.O.T.; Resources, J.O.T.; Software, O.E.S.; Supervision, J.P.B., and J.O.T.; Validation, O.E.S., J.P.B., and J.O.T.; Visualization, O.E.S., J.P.B., and J.O.T.; Writing - Original Draft, O.E.S., J.P.B., and J.O.T.; Writing - Reviewing & Editing, O.E.S., J.P.B., and J.O.T.

J.P.B. measured the relaxation time.

IV. Geometry-dependent Elastic Flow Dynamics in Micropillar Arrays

Oskar E. Ström, Jason P. Beech, and Jonas. O. Tegenfeldt

Manuscript (2023)

Conceptualization, O.E.S., J.P.B., and J.O.T.; Data Curation, O.E.S.; Formal Analysis, O.E.S.; Funding Acquisition, J.O.T.; Investigation, O.E.S.; Methodology, O.E.S., J.P.B., and J.O.T.; Project Administration, J.O.T.; Resources, J.O.T.; Software, O.E.S.; Supervision, J.P.B., and J.O.T.; Validation, O.E.S., J.P.B., and J.O.T.; Visualization, O.E.S., J.P.B., and J.O.T.; Writing - Original Draft, O.E.S., J.P.B., and J.O.T.; Writing - Reviewing & Editing, O.E.S., J.P.B., and J.O.T.

J.P.B. measured the relaxation time.

V. Broken Symmetries in Microfluidic Pillar Arrays are Reflected in a Flowing DNA Solution across Multiple Length Scales

Jason P. Beech*, Oskar E. Ström*, and Jonas. O. Tegenfeldt

**Joint first authorship*

Submitted for publication (2022)

Conceptualization, O.E.S., J.P.B., and J.O.T.; Data Curation, O.E.S. and J.P.B.; Formal Analysis, O.E.S. and J.P.B.; Funding Acquisition, J.O.T.; Investigation, O.E.S., and J.P.B.; Methodology, O.E.S., J.P.B., and J.O.T.; Project Administration, J.O.T.; Resources, J.O.T.; Software, O.E.S. and J.P.B.; Supervision, J.P.B., and J.O.T.; Validation, O.E.S., J.P.B., and J.O.T.; Visualization, O.E.S., J.P.B., and J.O.T.; Writing - Original Draft, O.E.S., J.P.B., and J.O.T.; Writing - Reviewing & Editing, O.E.S., J.P.B., and J.O.T.

J.P.B. designed and fabricated the devices and measured the relaxation time.

Acknowledgements

I am most grateful for my supervisor, Jonas, who has given me my position and who has supported and challenged me in so many ways. He has forced me to think independently and be creative. I am equally grateful to my co-supervisor, Jason, who has been there for me in the lab and always available with insightful and intelligent comments, ideas and feedback in scientific discussions. My PhD experience would not have been the same without him.

I am also grateful for the other members (or past members) of the Tegenfeldt research group. Bao, Kush, Stefan, Enrico, Elham, Esra, Wouter, Trung, Fei Fei, Elke and Max. Stefan together with Kush supervised me in the lab and taught me the intricacies of experimental microfluidics. I am truly glad to have had Bao as my lab mate, helping me when I am in need and always available for fika or lunch breaks.

I want to thank the members and the past members of the weekly biogroup meetings for thoughtful and interesting presentations and discussions. They gave my feedback and support of my work when I presented it. They include Christelle, Heiner, Jonas, Laura, Mercy, Martin, Frida, Therese, Roman, Jingyuan, Pradheebha, Ivan, Regina, Julia, Patrik, Rubina, Jingyuan, Diogo, Mokhtar, Mariia and Damiano.

I want to acknowledge and thank all my collaborators in the projects Beyondseq and NanoDiaBac. I am grateful to Fredrik Westerlund, Yuval Ebenstein, Tobias Ambjörnsson, Albertas Dvirnas, Jens Krog and Vilhelm Müller for interesting meetings, discussions and collaborations. A special thanks to Margarita Gomila and Jordi Lalucat that let me spend a week in their lab, teaching me cell culturing and Pulsed Field Gel Electrophoresis.

I could not have fabricated my devices in the cleanroom without the aid of the cleanroom staff. Thanks a lot Anders Kvennefors, Bengt Meuller, Dmitry Suyatin, George Rydnemalm, Håkan Lapovski, Ivan Maximov, Maria Huffman, Mariusz Graczyk and Sara Ataran for helping me.

My lab computers and my personal laptop never stop breaking down. I am thankful to have had Johanna Mosgeller, Alfons Eriksson och Andreas Bergelin to solve all IT difficulties.

I thank Jonas Johansson and Adam Burke for supporting me during tough times and helping me clarifying issues I had with my PhD studies.

I am grateful for all the administrators of FTF that have helped me walk through the jungle of bureaucracy. These include Abdul-Rehman Hakim, Louise Baldetorp, Mia Hedin, Anastasiia Anastasis, Charlotte Solberg, Gerda Rentschler and Marica Kolobaric.

I am also grateful to have spent time with so many nice colleagues. To name a few (there are many more): Jonatan, Sven, Lukas, Irene, Neimantas, Artis, Malin, Antti, Athanasios, David B, David A, Egor, Kristi, Florinda, Sebastian, Harald, Linnéa, Markus, Markus, Markus, Max, Pau, Simon, Hossein, Stephanie, Alfons, Bengt, Charlotte, Håkan, Mats-Erik, Maria, Adam, Knut, Martin, Ville and Sara. A special thanks to the colleagues of the H/C corridor (and David) – without you, my daily life would not have been as enjoyable.

I am also incredibly grateful for friends and family supporting me outside of working hours. Especially Dino, who inspired me and kept me motivated just by existing.

Finally, I am most grateful to the Swedish and European Union taxpayers that have funded my research through the funding agencies and the University.

Preface

The PhD thesis represents the entirety of the work, including the work presented in the licentiate thesis.

List of Acronyms and Notations

Symbol/Acronym/ Abbreviation	Description
$\boldsymbol{a}$	Acceleration [ms^{-2}]
A	Adenine
ALD	Atomic Layer Deposition
ASSURED	Affordable, Sensitive, Specific, User-friendly Rapid and robust, Equipment-free and Deliverable.
b	Kuhn Length [m]
BAC	Bacterial Artificial Chromosome
BME	β-mercaptoethanol
C	Cytosine
C	DNA Concentration
C^*	Overlap Concentration
C_e	Entanglement concentration
C^{**}	Crossover Concentration
D	Diffusion coefficient [$\mathrm{m}^2\mathrm{s}^{-1}$]
D_c	Critical Diameter in DLD [m]
De	Deborah Number
D_Z	Diffusion coefficient based on the Zimm Model [$\mathrm{m}^2\mathrm{s}^{-1}$]
DLD	Deterministic Lateral Displacement
DNA	Deoxyribonucleic Acid
dsDNA	Double-stranded DNA
El	Elasticity number
EMCCD	Electron multiplying charged coupled device
F	Force [N]
FEM	Finite Element Method
FJC	Freely-jointed chain
FSHD	Facioscapulohumeral Muscular Dystrophy
G	Gap length between pillars in microarrays [m]
G	Guanine

HSV	Hue, Saturation and Value (model)
h	Channel depth [m]
k_B	Boltzmann constant [JK^{-1}]
I	Ionic strength [mM] or [M]
l	Length [m]
L	Contour length [m]
l_0	Characteristic length scale (often the hydraulic diameter of the channel.) [m]
l_p	Persistence Length [m]
l_p'	Bare Persistence Length [m]
N	Periodicity of a DLD array
N_K	Number of Kuhn segments
N_{bp}	Number of base pairs of a polymer chain
NGS	Next-generation sequencing
OSF	Odijk-Skolnick-Fixman (theory)
P	Polarization Emission Ratio
PDMS	Polydimethylsiloxane
PEG	Polyethylene glycol
PEO–PPO–PEO	Poly(ethylene oxide)–poly(propylene oxide)–poly(ethylene oxide)
PFGE	Pulsed-field gel electrophoresis
PFOTS	Trichloro (1H,1H,2H,2H-PerFluoroOcTyl) Silane
Q	Flow rate [m^3s^{-1}]
R	Radius of a solid object encompassing a DNA molecule [m]
r	Radius [m]
R_e	End-end distance of a polymer [m]
R_F	Flory radius [m]
R_G	Radius of gyration [m]
R_h	hydraulic resistance [$m^5s^{-1}N^{-1}$]
Re	Reynolds number
SMRT	Single Molecule, Real Time (Sequencing)
T	Thymine
T	Temperature [K] or [°C]
T_θ	Theta temperature [K] or [°C]
T4 DNA	Bacteriophage T4 GT7 DNA, 165 600 bp
τ_{relax}	Relaxation time [s]

TE	Tris EDTA (buffer)
u	Fluid velocity [ms^{-1}]
u_0	Characteristic velocity [ms^{-1}]
w	Channel width [m]
w_{eff}	Effective width [m]
Wi	Weissenberg number
WLC	Wormlike chain
x	Lateral position along the array or the stretched DNA length
YOYO-1	Tetracationic homodimer of Oxazole Yellow (fluorescent dye)
z	Chain interaction Parameter
$\Delta\lambda$	Array row shift [m]
Δp	Pressure difference [mbar]
ε	Array row shift fraction [m^{-1}]
ζ_Z	Zimm Friction or drag coefficient
η	Dynamic viscosity [Nsm^{-1}]
θ	Displacement angle in DLD [°]
λ	Center-center distance of obstacles [m]
λ DNA	Lambda-bacteriophage DNA, 48 502 bp
ρ	Density [$\mathrm{kg\ m}^{-3}$]
τ	Shear stress [Nm^{-2}]
ν	Flory exponent
$\dot{\gamma}$	Shear rate [s^{-1}]

Table of Contents

Abstract ..... **i**

Populärvetenskaplig sammanfattning på svenska ..... **v**

List of Publications ..... **vii**

Acknowledgements ..... **xi**

Preface ..... **xiii**

List of Acronyms and Notations ..... **xv**

Table of Contents ..... **xix**

1. Introduction **1**

1.1 Thesis Aims 1

1.2 Tools for Long DNA Sample Preparation and Transport 1

1.3 Summary of Main Achievements 6

1.4 Thesis Structure 7

2. Microfluidics Theory **9**

3. DNA Polymer Properties in Equilibrium **15**

3.1 Introduction to DNA 15

3.2 DNA Size 16

3.3 High-concentration DNA 19

4. DNA Extension and Relaxation **23**

4.1 Force-extension Relationship 23

4.2 DNA Molecules in Flow 25

4.3 DNA Relaxation 26

4.4 DNA Stretching for Optical Mapping 28

5. DNA Separation in Deterministic Lateral Displacement **31**

5.1 Background 31

5.2 Deterministic Lateral Displacement 32

5.3 Critical Size 34

5.4 Impact of Diffusion 35
5.5 Displacement of DNA 36
5.6 Throughput 40
5.7 Flow-induced DNA Fragmentation 41

6. Viscoelastic fluids in Pillar Arrays 43

6.1 Viscoelastic fluids 43
6.2 Introduction to Elastic Turbulence 46
6.3 Elastic Turbulence around Single Pillars 47
6.4 Elastic Turbulence in Pillar Arrays 49
Effect of Sample Composition 49
Effect of Array Geometry 50
Effect of Pillar and Pore Shape 53

7. Device Fabrication and Experimental Details 55

7.1 Device Fabrication 55
Device Design 56
Mold Fabrication – UV lithography 56
Mold Fabrication – Maskless Photolithography 57
Replica Molding 58
Surface Modifications 58
7.2 DNA Samples 59
7.3 Running the Experiments 61
Microfluidic Devices 61
Single Molecule Epifluorescence Microscopy 62
Dual-channel Color/Polarization setup 64

8. Conclusions 65

8.1 Paper I: High-throughput Separation of Long DNA in Deterministic Lateral Displacement Arrays 66
8.2 Paper II: Long DNA Isolation and Imaging using Lateral Displacement Arrays Integrated with DNA combing 68
8.3 Paper III: Short and Long-range Cyclic Patterns in Flows of DNA Solutions in Microfluidic Obstacle Arrays 70
8.4 Paper IV: Geometry-dependent Elastic Flow Dynamics 72
8.5 Paper V: Broken Symmetries in Microfluidic Pillar Arrays are Reflected in a Flowing DNA Solution across Multiple Length Scales 74

9. Outlook 77
9.1 Device Integration 77
9.2 Separation Throughput 77
9.3 Separation of Clinical Samples 78
9.4 Elastic Effects 78
9.5 From Lab to Patient 79
Appendix 1: Lab Protocols 81
1.1 UV Lithography Protocol 81
1.2 Maskless Photolithography Protocol 83
1.3 Cyclo Olefin Polymer Glass Coating 84
1.4 Replica Molding 85
1.5 Troubleshooting: Fabrication and Experimentation 88
1.6 DNA Staining 90
Appendix 2: Numerical Simulations 91
Appendix 3: Data Analysis 93
3.1 Background Subtraction 93
3.2 Ionic Strength Calculation 94
3.3 Analysis of Polarization Images 95
Appendix 4: Pressure Control System Schematics for Paper II 97
Appendix 5: 2D Fourier Analysis 99
References 101
Papers 111

1. Introduction

1.1 Thesis Aims

The aims of this thesis are three-fold. The first aim is to develop sample preparation methods for long-DNA analysis that overcomes the limitations of the conventional systems in terms of processing time, cost and manual labor. The methods are both to be used for stand-alone long-DNA sample preparation and towards a fully integrated microfluidic chip that both prepares and analyzes DNA. The second aim is to investigate new elastic flow phenomena which could improve or set the limitations for microfluidic DNA systems. The third aim is to document my work and to build a foundation of knowledge for follow-up experiments.

1.2 Tools for Long DNA Sample Preparation and Transport

Deoxyribonucleic acid (DNA) is the code of life. The information to create and maintain a living being is encoded in this polymer. It is stored in almost every cell of your body. Its structure (see Figure 1.1) was discovered to be double-helical by Francis Crick, James Watson, Maurice Wilkins and Rosalind Franklin in 1953 [1]. From that time, the science and technology of genetic analysis has been developing at an accelerating rate. In 2003, the human genome project was completed where the entire human genome was sequenced [2]. Since then, sequencing technology has revolutionized accessibility to genetic data.

Mapping and sequencing DNA have become increasingly important in biology and medicine. Identifying, tracking, and understanding the expression of genes are crucial to modern biology. By accessing an individual's genome, we gain information about underlying health risks and the prevalence of genetic disorders or variations. This form of personalized medicine can be used preventively to minimize negative patient outcomes[1]. Similarly, we can gain precise and accurate

[1] It should be noted that the strict ethical and privacy measures should be taken to ensure that such information about an individual's genome is not misused.

information of the type of infectious disease one is suffering from by analysing the DNA of disease-causing microorganisms. By analysing and identifying the plasmids a bacterium is carrying we gain knowledge of the prevalence of antibiotic resistance genes. Knowing what specific disease or resistance gene that is present is crucial in order to give the patient the right treatment. The sooner the right treatment is given for a disease one has contracted, the lower the chances of severe negative health consequences and the higher the likelihood of survival.

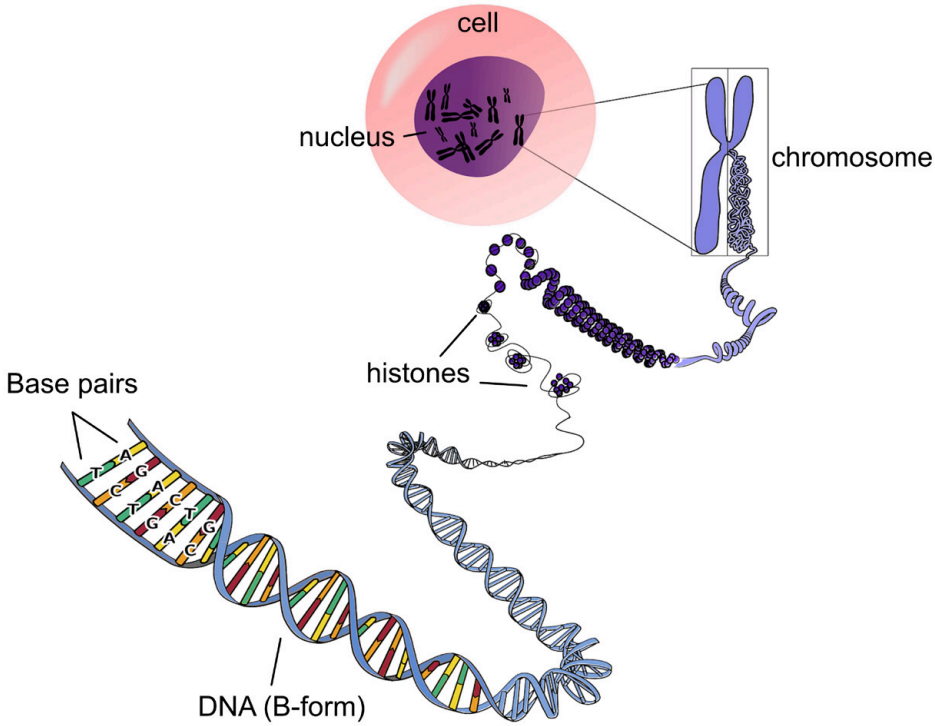

Figure 1.1. Structure of DNA. From base pairs to condensed chromosomes in the cell nucleus of eukaryotic cells. The figure is acquired from pixabasy.com, in the public domain.

Longer DNA strands (see the text box on the following page) can contain information that shorter strands cannot. Sequencing only shorter strands may result in failure to detect long-range genomic aberrations such as structural variations [3]. Such variations include (among others): insertions, deletions, inversions and copy number variations (varying number of copies of a particular gene). These are important to genetic diseases such as facioscapulohumeral muscular dystrophy (FSHD) type 1. FSHD type 1 appears in an individual if the number of continuous repeats of 3.3 kbp genetic units is too low (FSHD appears if the number is less than 10 whereas unaffected individuals have 11 to 150 units)[4]. If the sequencing

relies only on short reads, it can be impossible to detect the number of continuous repeats and the genetic disease cannot be diagnosed.

In order to accurately ascertain the sequence of long DNA, several commercial long-read technologies have been developed with different resolving powers, ranging from thousands of bases down to individual bases. These include nanopore sequencing [5], single molecule real time (SMRT) sequencing [6], optical DNA mapping in nanochannels [7], and linked-read sequencing [8]. They can be used to aid short read sequencing by providing a scaffold or to be used on their own. In order for them to work efficiently, it is important that long-DNA samples are properly prepared and free from contaminants.

Long DNA

The upper length limit of DNA separation in standard gel electrophoresis is around 20 000 bp. DNA molecules longer than this will essentially migrate in a size-independent manner and are referred to as "long". [9]

There is a number of processing steps that has to be carried out in order to obtain genetic information of long DNA from a biological sample. Figure 1.2 illustrates the typical steps.

The conventional method of preparing long DNA is gel immobilization [10]. Cells of interest are encapsulated in a gel and are then subject to a number of processing steps, including lysis and washing. Thereafter, the gel is digested and the DNA strands are recovered with drop dialysis. By using a gel, the genomic DNA is protected from high shear forces present during liquid handling of DNA [11]. However, the long diffusion distances through the gel for reagents and waste products makes the method overly time-consuming. The high number of manual steps makes it also labor intensive and tedious.

Modern approaches for long-DNA preparation are much faster. Affinity-based sample preparation kits such as PacBio's Nanobind have shown to yield high quality long DNA that lead to record read lengths.

If a selected length of long DNA is desired, length-based separation is needed after the gel immobilization step. The gold standard is pulsed-field gel electrophoresis (PFGE) [10]. It separates DNA molecules by letting them migrate under the influence of an electric field in a network of pores. Using pulsed electric fields in multiple directions allows the technique to overcome the length-based limit of approximately 20 kbp of standard gel electrophoresis [9]. However, the low electric field strengths and the long re-orientation times makes the technique slow and tedious. This step adds about one additional day to the already day-long gel-based preparation. In addition to being time-consuming, PFGE requires an expensive instrument and involves many manual steps performed by a trained

professional. While modern versions of PFGE, that are faster and simpler to use, have been developed (see *e.g.* the products of Sage Science), they still have many hours up to days of run time and high sample losses (65%–75%[12]).

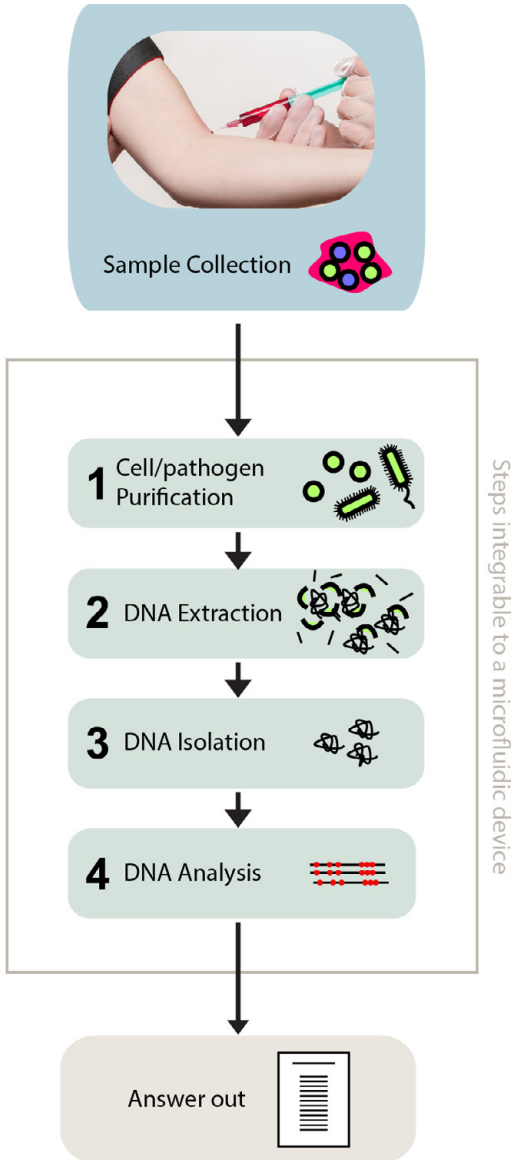

Figure 1.2. General steps needed to obtain genetic information of long DNA from biological samples.

Microfluidics has the potential of replacing the conventional gel-based approaches. Microfluidic devices consist of systems of micrometer-sized channels where the sample can be manoeuvred into different compartments where it is subject to chemical and physical actions. The short distances make diffusion times very short and any analysis or manipulation step rapid. The distances for diffusion to act in gel plugs are about $10 - 100$ times longer than what they are in microfluidic systems (several mm compared to a few to hundreds of micrometers). This translates to 100–10,000 times longer diffusion times. By relying on microscale channels, the devices can be made small and portable. The small scale also makes it possible to work with tiny amounts of samples. It can often be the case that the sample quantity is limited or a minimal biopsy is preferred during sample collection. When following the development of e.g. a tumour and collecting multiple samples over time, dealing with small samples make the whole procedure considerably simpler and could reduce the chances of infection. The devices, usually made out of tiny quantities of plastic, can be made inexpensive by mass-production. Lastly, multiple components of the sample processing can be integrated into the same device, making the whole sample processing and analysis more efficient without sample loss or other complications during the sample transfer steps.

While microfluidics come with a series of advantages, there is a lack of high-throughput microfluidic sample preparation for long-DNA analysis. Most systems need to be run at miniscule flow velocities which makes it impossible to collect enough sample for subsequent analysis after the preparation step. It is possible to overcome this problem by parallelizing a high number of devices as demonstrated by Wunsch et al.[13]. However, massive parallelization comes with its own complications such as having to design and fabricate a highly complex system with fluidic connections between all the parallel devices. In this work, we aim towards improving the throughput of long-DNA preparation in two ways. By increasing the sample volume that is processed in each moment in time as well as increasing the sample concentration itself.

This work is centered around manipulating and transporting DNA across micro pillar arrays. Such arrays have been shown to be extraordinary simple and useful when it comes to DNA separation. They are continuous (in contrast to the batch-based gel preparation methods) and separate the DNA spatially (in contrast to gel electrophoresis which is only temporal). These include the Brownian ratchet [14], DNA prism [15] and Deterministic Lateral Displacement (DLD) [16]. While they have demonstrated separation within a rather short timeframe, they have all been shown to separate DNA at insufficiently low throughput for post-separation collection and off-chip analysis (see subchapter 5.6 and Table 5.1). DLD has been used for the separation work in this thesis. It is exceedingly simple as it only requires a fluid flow for it to work. Moreover, it exhibits very high separation resolution and separation tunability.

Polymer solutions, especially those that contain long strands, can display interesting elastic flow behavior in microfluidic systems. Elastic instabilities and elastic turbulence can emerge. These could either be beneficial or detrimental for the system. Elastic effects have been shown to be useful for mixing of reagents in microfluidic channels that otherwise is difficult to achieve due to the laminar, non-mixing, nature of the flow [17]. However, such effects can also be very damaging to systems that rely on laminar flow to work, such as DLD. Elastic instabilities could perturb the flow and thus also the particle trajectories in the device and potentially negatively impact the separation. These effects can also be useful to study on their own account to improve the understanding of polymer flow in microchannels.

1.3 Summary of Main Achievements

This work is split into three separate parts. The first one is long-DNA preparation in the form of separation and isolation of long DNA in Deterministic Lateral Displacement (DLD) arrays. The second is the integration of long-DNA isolation and surface-stretching on a microfluidic chip. The third one is the study of high-concentration DNA transport across micro pillar arrays and the elastic effects that emerged.

In **Paper I**, we demonstrate that we can displace and separate long DNA in DLD devices at ultra-high flow velocities where the DNA strands extended to a large degree. High-velocity, long-DNA separation in micrometer-sized devices was previously not thought possible due to the long-DNA extension making differently long DNA molecules behave similarly in the device. We show that we can improve the volumetric and sample throughput four orders of magnitude compared to previous work (up to 24 µL/h or 760 µg/h for 166 kbp from 48.5 kbp compared to ~0.04 µl/h and ~0.12 ng/h [16], see Table 5.1 for details). This allows for a rapid process and makes post-separation collection and analysis possible. We explore the effect of high DNA concentrations and show that is can both enhance and lessen displacement and thus separation.

In **Paper II** we demonstrate that we can integrate long-DNA isolation in DLD with a DNA analysis technique, surface-based DNA stretching. This eliminates the sample transfer step between the two techniques and makes the entire process ultra-fast as only a few hundred stretched DNA strands are needed in surface-based stretching to achieve a large enough statistical foundation for genetic analysis. This device is a step towards a fully integrated system which is simple, fast, efficient and cheap.

During the efforts to increase the sample throughput in the pillar arrays of paper I, we discovered that some DNA solutions formed periodic waves of high

concentration and extension with aligned DNA strand orientation. The waves appeared in up to two orientations for long DNA (> 48.5 kbp in length), at high flow velocity and high DNA concentration. The investigation of the waves in a quadratic array is the basis of **Paper III**. In it, we studied the waves as a function of flow rate, buffer composition (ionic strength and solvent viscosity), concentration and molecular length. We find that the waves only occur at high concentration to overlap concentration ratios, C/C^*, or at higher solvent viscosity. We also observe periodic cycles of vortex growth and shedding and believe that their shedding of DNA mass is closely related to the waves.

Paper IV follows up on paper III and compares the high-concentration, long-DNA flow pattern in a quadratic array to those in a hexagonal and disordered arrays and a device with sparsely distributed pillars. We find that instead of waves, large zigzag fluctuations appear in a hexagonal array and no large-scale flow patterns form in the disordered array. In the quadratic, disordered and sparse arrays, a periodic cycle of growth and shedding of vortices in the pillar gaps is observed. Their interaction or lack of interactions are likely to give rise to waves or be the reason for the lack of waves in the arrays.

In **Paper V**, we have made the pillars in a quadratic array of triangular cross-section instead of circular. The broken symmetry due to the triangular pillars leads to asymmetric wave formation and dynamics of the flow that depend on flow direction. This work shows that the waves are highly dependent on the pillar design and gives insight in the mechanisms of the wave formation.

1.4 Thesis Structure

The work presented in this thesis is divided into fourteen parts: nine chapters and five papers. What follows is a brief description of the chapter contents:

Chapter 1 gives a background to and states the importance of the work.

Chapter 2 describes the underlying microfluidic theory needed to understand the basic flow in the devices.

Chapter 3 gives a brief description of the polymer properties of individual DNA strands and high-concentration DNA solutions. It especially focuses on how size can be described for DNA.

Chapter 4 delves into the extension and relaxation of DNA strands. It deals with the force-extension relationship and the dynamics of relaxation and DNA in shear and extensional flow. Both flow types occur in the pillar arrays of this work This chapter ends with giving an overview of stretching techniques for optical DNA mapping.

Chapter 5 introduces the microfluidic separation technique, Deterministic Lateral Displacement (DLD) and describes how long DNA is likely to behave in its platform. The displacement mechanism, methods for improving throughput and potential flow-induced fragmentation are also discussed.

Chapter 6 describes the properties of viscoelastic fluids and their flow around both single pillars and across pillar arrays. Elastic turbulence, that is a central theme in the Papers III–V, is introduced and reviewed.

Chapter 7 presents how and with what means the experimental results were achieved. This includes device design, sample preparation, microfabrication and running the experiments.

Chapter 8 wraps up the thesis and draws conclusions paper by paper.

Chapter 9 concludes the thesis by giving an outlook on future research.

2. Microfluidics Theory

This chapter introduces the microfluidic theory that is needed to understand the flow that occur in microfluidic channels.

Microfluidics is the science and technology of manipulating and controlling fluids at the microscale.

A **fluid**, either a gas or a liquid, is a material that continuously deforms under an applied shear stress or external force.

What happens to the flow of water when you constrict it to a microchannel? In everyday life, a fluid, like water, displays turbulent flow and mixes readily. In the micro-world, the flow instead becomes laminar and predictable. The concepts of laminar and turbulent flow can more easily be understood by comparing the flow of water to that of honey. Imagine a scenario in which you are stirring a spoon in a glass full of either of the liquids. If the honey is very viscous, the force of the stirring would be transferred to the glass itself. The honey would barely move while the glass would follow the rotational movement of the spoon. In comparison, the water flows much more easily than the honey does. The glass with water does not move at all while the water flows chaotically around with the movement of the spoon. The flow in the honey is laminar, while the flow in the water is turbulent.

In microchannels, the internal friction of the fluids plays a much larger role than what it does in the macroscopic everyday world. Similar to how honey would drip in a laminar way from a jar, the flow in microchannels can be seen to be divided up into individual stream lanes, *laminae*. If you would let two colored streams of water flow next to each other in a microchannel, they would not mix like they would in a macro setting. Rather, they would just flow next to each other. Figure 2.1 illustrates this phenomenon.

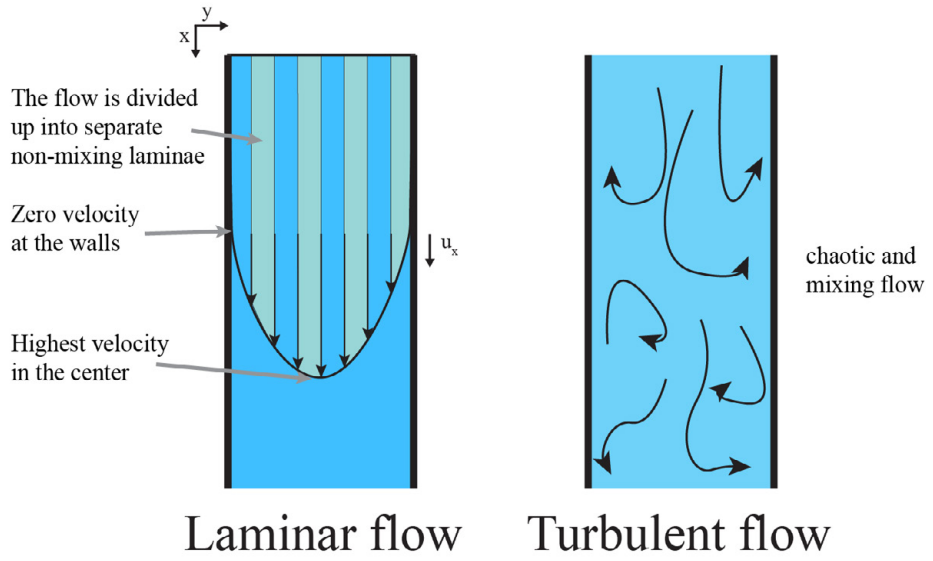

Figure 2.1. Illustration of laminar and turbulent flow. Laminar flow is divided into ordered, parallel laminae whereas turbulent flow is chaotic and mixing. Note that in reality, the laminae are infinitely thin. The figure is based on a similar figure in [18] with permission.

At microchannel walls during pressure-driven flow, the fluid velocity is zero. This is called the no-slip boundary condition. No one has ever directly been able to confirm its existence but it has been validated through indirect means [19]. As a consequence, the fluid flowing through the channel will develop a parabolic flow profile with the highest velocity in the center of the channel, see Figure 2.1. This shape of the flow profile is important for the flow dynamics of complex objects like long polymers. It will affect the degree of extension and rotation experienced by the object. See subchapter 4.2 for how the shear flow affects the motion of DNA.

The motion of fluids is described by the Navier-Stokes equation. These are essentially a continuum version of Newton's second law of motion ($m\boldsymbol{a} = \boldsymbol{F}$) [20]:

$$\rho\left[\left(\frac{\partial \boldsymbol{u}}{\partial t}\right) + (\boldsymbol{u}\cdot\nabla)\boldsymbol{u}\right] = -\nabla p + \eta\nabla^2\boldsymbol{u} + \boldsymbol{f} \tag{2.1}$$

where ρ is the density of the fluid, $\boldsymbol{u}$ is the fluid velocity, p is the pressure and η is the dynamic viscosity. The left side of the equation describes changes in fluid momentum. The first term, $\rho\frac{\partial \boldsymbol{u}}{\partial t}$, expresses change in velocity over time for a given position (local acceleration) whereas the second term, $\rho(\boldsymbol{u}\cdot\nabla)\boldsymbol{u}$, expresses change in velocity as the fluid moves from one place to another (convective

acceleration). The first term on the right side, $-\nabla p$, describes the pressure gradient. The second term, $\eta\nabla^2\boldsymbol{u}$, describes the viscous effects while the third, $\boldsymbol{f}$, expresses body forces such as gravity or electrostatic forces.

In microchannels, we can assume that the flow velocity is so much smaller compared to the speed of sound that we can treat the fluid as incompressible. The density is then assumed to be constant in time and space. This is expressed with the continuity equation:

$$\nabla \cdot \boldsymbol{u} = 0 \tag{2.2}$$

In the devices, we control the flow rate of the liquid by applying a pressure difference across the channel, Δp. The volumetric flow rate of the liquid, Q, follows from the Hagen-Poiseuille law, $\Delta p = R_h Q$, where R_h is the hydraulic resistance or friction. The lower the resistance that is present for the liquid under a given pressure difference, the faster will be its rate of flow. The hydraulic resistance of a channel with a rectangular cross-section with depth h and width w, and length L, using a fluid with viscosity η can be approximated to [20]:

$$R_h \approx \frac{12\eta L}{wh^3}\left(\frac{1}{1-0.63h/w}\right) \tag{2.3}$$

This approximation is valid when $h < w$. If the depth is much smaller than the width, the error rate becomes very low. For example, when $h = w/2$, the relative error is down to 0.2%. When $h = w$, the error is instead 13%. See the microfluidic textbook by Bruus for more accurate resistance calculations [20]. Equation (2.3) is useful when designing the resistances of the channel to make the flow balanced between inlets or outlets.

The flow profile in a microchannel, as illustrated in Figure 2.1, is parabolic. By combining the no-slip boundary condition and equation (2.1) with the inertial term disregarded, we end up with the following description of the flow velocity along the channel direction, x:

$$u_x(y) = u_{x,max}\left[1-\left(1-\frac{2y}{w}\right)^2\right] \tag{2.4}$$

where w is the channel width, $0 < y < w$.

The flows that are generated in this work has mainly been a combination of shear and elongational (or extensional) flow. Simple shear flow only has a velocity gradient perpendicular to the direction of the flow, whereas pure extensional flow only has a velocity gradient in the direction of the flow. Simple shear flow can be

seen as a superposition of extensional and rotational flow, as depicted in Figure 2.2.

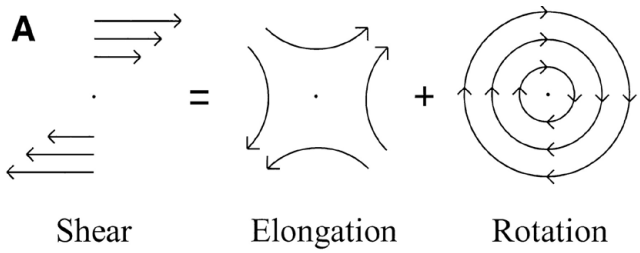

Figure 2.2. An illustration of shear flow, which is a superposition of purely elongational (or extentional) and purely rotational flow. From [21]. Reprinted with permission from AAAS.

To understand the concept of shear, one can again compare the flow of water and honey. Applying the same external force, the resulting shear rate will be much lower for honey than for water. The fluid layers in the honey then slide past each other more slowly compared to what they would do in water.

The rate at which the laminae or layers of the flow move past each other is called the shear rate, $\dot{\gamma}$. It is the rate of the fluid deformation as a result of an external force, giving rise to a shear stress, τ:

$$\dot{\gamma} = \frac{\tau}{\eta} = \frac{\partial u_x}{\partial y} \tag{2.5}$$

$\dot{\gamma}$ describes the flow velocity gradient perpendicular to the flow. It can be difficult to estimate $\dot{\gamma}$ in a complex microchannel geometry such as a micropillar array. The expression $\dot{\gamma} \approx \langle u \rangle / l$ gives a rough estimate, where $\langle u \rangle$ is the mean flow velocity and l is the channel width.

In a microchannel flow, the shear rate inversely follows that of the flow velocity. At the channel walls, the shear rate is the highest while being at a minimum in the center of the channel. By combining equations (2.4) and (2.5) we come to the following expression for the shear rate:

$$\dot{\gamma}(y) = \left(\frac{4u_{x,max}}{w}\right)\left(1 - \frac{2y}{w}\right) \tag{2.6}$$

For practical work with microfluidics, it is useful to know if the flow of a given fluid in a given geometry at a given flow velocity exhibits a laminar or turbulent behavior. A rough idea can be obtained from the Reynolds number, *Re*:

$$Re = \frac{\rho l_0 u_0}{\eta} \tag{2.7}$$

where ρ is the density of the fluid, η is the viscosity of the fluid, l_0 is the characteristic length scale (often the hydraulic diameter of the channel) and u_0 is the characteristic velocity (often the average flow velocity). *Re* describes the relative impact of inertial forces to that of viscous ones in the system. With small *Re* ($<< 1$), as used in this thesis (from 10^{-6} up to 10^{-1}), we can neglect the inertial forces [first and second term in equation (2.1)] and assume a laminar flow. At *Re* of approximately 1 – 1000, inertial effects can become noticeable. They include Dean flow and non-turbulent inertial vortices which have been exploited for particle separation [22]. At *Re* above approximately 2000, the flow becomes turbulent with random flow velocities in time and space [23]. By changing the fluid from water to honey, *Re* can be increased a few thousand times with the higher viscosity of honey.

3. DNA Polymer Properties in Equilibrium

"DNA neither cares nor knows. DNA just is. And we dance to its music."

— Richard Dawkins, River Out of Eden: A Darwinian View of Life

In this thesis, long DNA polymers are the objects of interest. What follows is a brief summary of important DNA polymer properties in equilibrium, relevant to the work presented here. The first part of this chapter describes dilute solutions where the molecules are seen in isolation without interacting with other molecules. The second part concerns with high-concentration solutions where molecule-molecule interactions are significant. Note that in my work, the polymers are never close to being in an equilibrium. There is always a flow that forces them into different conformations. However, understanding the polymer properties in equilibrium is useful to comprehend how polymers could behave in non-equilibrium systems. For more details on single polymer dynamics, see the excellent review by Schroeder from 2018 [24].

3.1 Introduction to DNA

Deoxyribonucleic acid or DNA consists of two helices wrapped around each other. Each helix consists of a negatively charged sugar-phosphate backbone bound to building blocks or bases. There are four bases: adenine (A), thymine (T), guanine (G) and cytosine (C). A binds to T and C to G. Figure 3.1 shows both a schematic and a molecular illustration of DNA. The stability of DNA is both due to hydrogen bonds between the bases but also due to base stacking. Extended sequences of one of the base pairs will affect the mechanical properties of the polymer, *e.g.* A-tracts will cause kinks in the strands [25]. However, the polymers used in this work is on the first order homogenous and treated as independent of the base pair sequence.

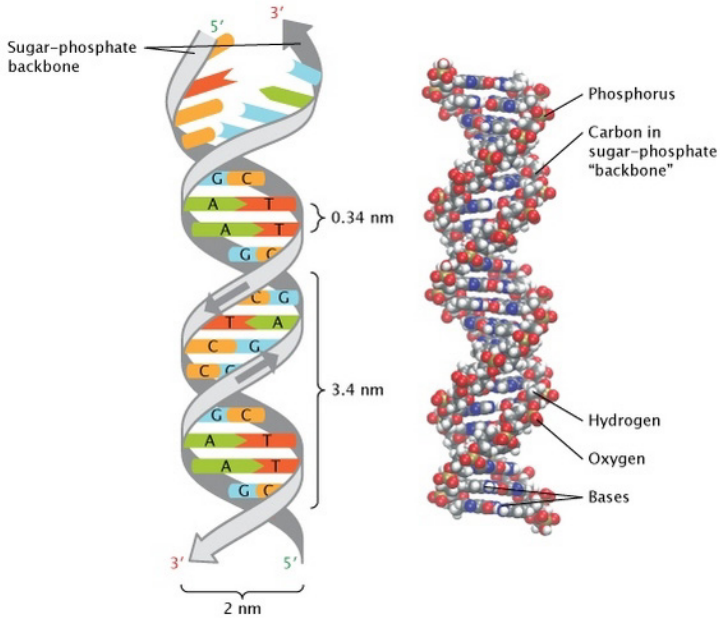

Figure 3.1. Structure of DNA. *Left panel shows the schematic representation of the double helix in its most common structure, B-DNA. The right panel shows the molecular representation of the left. Reprinted with permission from [26]. © 2013 Nature Education.*

3.2 DNA Size

DNA is about 2 nm in bare width, with each base pair 0.34 nm long for its most common structure, B-DNA as shown in Figure 3.1. Ten base pairs (3.4 nm) make up a pitch in the right-handed helix [27]. In this work, fluorescent intercalating molecules (YOYO-1, see subchapter 7.3) are added to the DNA molecules in order to visualize them. Note that the DNA molecule length is extended with 0.51 nm for every YOYO-1 dye molecule that is intercalated into the chain. The extension is up to approximately 38% with full saturation of one intercalating dye molecules per four base pairs [28]. Figure 3.2 shows a dye molecule bound to DNA. Note how the dye molecule is inserted between the base pairs and thereby elongates the chain. As dye molecules are added during the experiments, it is important to take this extension into account when the DNA size is calculated.

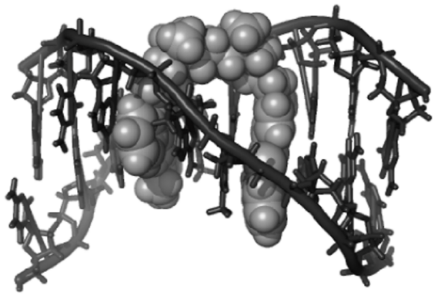

Figure 3.2. Nuclear magnetic resonance (NMR) image of the YOYO-1 analogue TOTO-1 bound to DNA. The image is reproduced from Nyberg *et al.* [29] whereas the NMR data is from Spielmann *et al.* [30] (no permission required).

In solution, long polymers curl up into a blob. The size of this blob is determined by the strand stiffness. Polymer stiffness is characterized by the persistence length, l_p. The persistence length is the length scale below which a polymer can be considered a stiff rod. A more formal definition describes it as the length scale at which the correlation of the tangent-tangent vector of the polymer decays [31]. For bare DNA, it is about 50 nm [9]. Note that the persistence length remains unaffected by the intercalation of YOYO-1 [28]. However, it depends on the ionic strength of the buffer, I, according to Odijk–Skolnick–Fixman (OSF) theory as [32-34]:

$$l_p = l_p' + \frac{0.0324M}{I} \tag{3.1}$$

where $l_p' = 50$ nm is the bare persistence length. l_p doubles when the salt concentration is decreased from high [$I \approx 30$ mM, 5×Tris EDTA (TE) buffer] to low ($I \approx 0.6$ mM, $0.1\times TE$).

For a rough estimate of the mechanical dynamics of a polymer, the freely-jointed chain (FJC) model can be used. It is simple but useful. It treats the polymer as ideal, meaning that interactions between polymer segments that come close to each other physically are not taken into account [35]. With the FJC model, a polymer is seen as a chain of N_K stiff, rod-like segments, with no limits in the range of bond angles. With this model, the segments have equal probability to fluctuate in all directions. The orientation of neighbouring segments do not affect each other at all. The segment length is called the Kuhn length, b, and is twice the persistence length. The contour length, L, is the polymer length at full extension and is given by:

$$L = l_{bp}N_{bp} = bN_K \tag{3.2}$$

where N_{bp} is the number of base pairs with length l_{bp}. The contour length of a bare λ DNA molecule (48.5 kbp) is 16.5 μm and 22.7 μm when saturated with YOYO-1 fluorophores (1:4 fluorophores per base pair).

Another ideal polymer model, the worm-like chain (WLC) model (also called the Kratky-Porod model) describes the polymer mechanical dynamics more accurately than the FJC model. In the WLC model, the polymer is defined as semi-flexible. It means that the chain is stiff at the length scale of a monomer but flexible at the length scale of the entire polymer. In this model, the angle of a single segment affects the angle of its neighbour compared to FJC where the segment angles are completely independent. The end-end distance of the polymer, R_e, is a measure of the size of the coiled-up polymer. The WLC model describes R_e for long chains ($L \gg l_p$) with [35]:

$$R_e = b\sqrt{N_k} = \sqrt{Ll_p} \tag{3.3}$$

Another way to characterize the size of a polymer is with the radius of gyration, R_G. The radius of gyration of a polymer is the root mean square distance of the polymer segments from its center of mass, r_{mean} [36]:

$$R_G^2 \equiv \frac{1}{N_k}\sum_{i=1}^{N_k}\langle(r_i - r_{mean})^2\rangle \tag{3.4}$$

For an ideal chain, it is given by [35]:

$$R_G = \frac{R_e}{\sqrt{6}} = b\sqrt{\frac{N_k}{6}} \tag{3.5}$$

In contrast to R_e, R_G can be easily measured experimentally. Most often by determining the Brownian motion of DNA chains using fluorescent videography (see *e.g.* the work by Smith *et al*. [37]).

The choice of solvent will affect the chain conformation. A good solvent will favor monomer-solvent interaction which causes the chain to expand. A poor solvent will do the opposite, resulting in a chain contraction. In other words, a good solvent "wants" to be with the solute and a poor solvent does not. If the solvent is too poor, the solute "hides" from the solvent by precipitating, like DNA does in ethanol. However, if the solvent is just poor enough to cancel out the monomer-monomer repulsions it is called a θ-solvent. In a θ-solvent, the chain acts ideally, as in the FJC model.

In this thesis, we have exclusively worked with good solvents (aqueous buffers). The ideal chain models, described above, make two important assumptions that are not valid at most experimental conditions. The first assumption is that the segments do not occupy any volume and thereby do not sterically hinder other segments from passing through them, which they do. The same volume of space can only be occupied once. This volume is then excluded for the rest of the chain to occupy. Secondly, the ideal chain models do not take electrostatic interactions into account. In reality, the negative-charged monomers repulse each other electrostatically, increasing the size of the polymer coil as salt concentration is lowered.

To make the model more valid for real experimental conditions, several measures are taken. An effective width, w_{eff}, is used. It includes both the steric and electrostatic interactions and can be much larger than the bare DNA width. At high salt concentration (100 mM), w_{eff} is around 5 nm while at low salt concentration (5 mM), it is as large as 20 nm. Flory also provided a scaling-law ($R_e \sim N_k^{\nu}$) where ν is the Flory exponent and the excluded volume interactions are taken into consideration [35]. When the other effects are also included, the end-end distance is denoted as the Flory radius and expressed as [31]:

$$R_F \approx \left(w_{eff} l_p\right)^{1/5} (L)^{\nu} \tag{3.6}$$

where the original value of the Flory exponent, $\nu = 3/5$. A more accurate value of ν has later been found to be 0.5877 [38]. To calculate precise values of R_g in non-ideal conditions, theoretical frameworks such as blob theory [35, 39] can be employed. In the presented papers of this thesis, a rough estimation of the non-ideal case has been made, $R_g \approx \sqrt{R_F/6}$. While this estimation is an oversimplification, it can still be used for investigating scaling relationships and give an approximate value that is good enough for the development of the microfluidic devices presented here.

3.3 High-concentration DNA

When the concentration of polymers becomes high enough, molecule-molecule interactions becomes significant, affecting the behaviour of both individual molecules and the fluid itself. Each polymer is then surrounded by a network of other polymers. Instead of being described as a coil with a given radius, the volume in which the polymer finds itself in a given moment of time can be seen as tubular. It is not unlike the space of a gel where interconnected pores form a network of tubes.

Polymer solutions can be divided into three main regimes [40] dilute, semi-dilute and concentrated (Note that other regime divisions exist [41]). See Figure 3.3 for an illustration of the first two regimes. They are called dilute if the concentration is below the overlap concentration, C^*, the threshold when the concentration is so high that the pervaded volume of the polymer chains overlap. Above this concentration, long polymers are called semidilute. While the illustration in Figure 3.3 makes the solution look quite homogeneous, it is characterized by a high degree fluctuations in polymer segment density. When the concentration is further increased (above the cross-over concentration, C^{**}), the solution will eventually reach a close to uniform density in polymer segments. Such a solution is called concentrated. Note that the cross-over concentration is generally difficult to experimentally detect and rarely reported in literature. As the concentration dependence of the chain dimensions have not been rigorously measured in this work, the term concentrated is not used. Instead, concentrations above the estimated C^* are referred to as high.

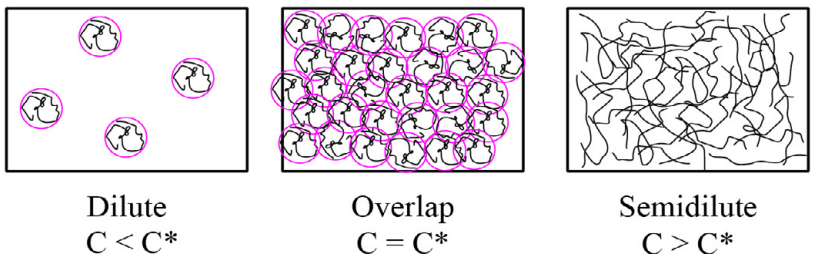

Figure 3.3. Concentration regimes for DNA. The pink circles represents the pervaded volume of the polymers. Note that in practice, the molecules in the middle box will The figure is adapted from [35].

The overlap concentration is given by [40]:

$$C^* = \frac{\mathrm{M}}{N_A} \frac{1}{\frac{4\pi}{3} R_g^3} \tag{3.7}$$

where M is the polymer molecular weight, N_A is Avogadro's constant, and R_g is the radius of gyration. C^* corresponds to the mean monomer concentration inside a single coil with radius R_g. Figure 3.4 illustrates how C^* changes with I and the number of base pairs.

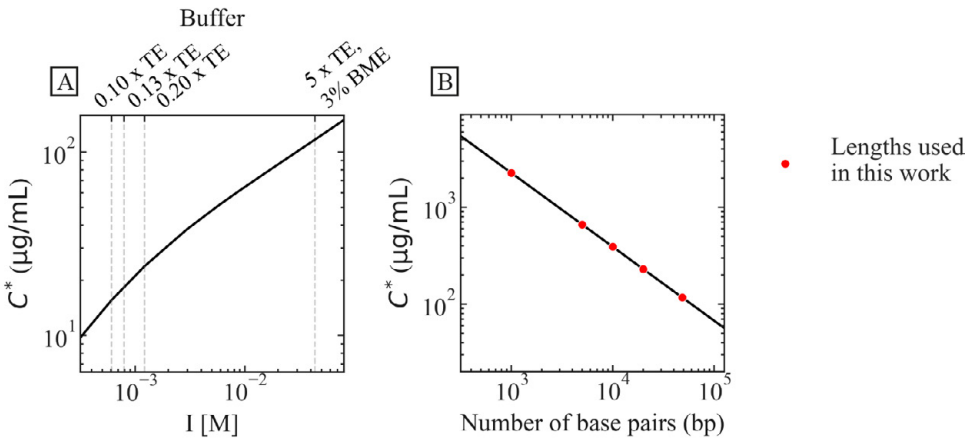

Figure 3.4. Overlap concentration as a function of Ionic strength (A) and number of base pairs (B). The calculation of C^* is based on the simplification $R_g \approx \sqrt{R_F/6}$, and $T = 23$ °C and a dye to base pair ratio of 1:200. The buffers used in this work has been marked with dashed lines in (A) and the polymer lengths used have been marked with red dots in (B).

Using equation (3.7), C^* equals 117 µg/mL for λ DNA (48.5 kbp) at high salt ($I =$ 44 mM), $T = 23$ °C and a dye to base pair ratio of 1:200, with $R_g \approx 0.5$ µm. Here, R_g is approximated using the simplification $R_g \approx \sqrt{R_F/6}$. The calculated magnitude of R_g is most likely higher than the true value. The value of C^* can be compared to the value by Pan *et al.* who determined $C^* = 44$ µg/mL using dynamic light scattering experiments and Brownian dynamics simulations. Their experiments were conducted in excess salt with chain interaction parameter, $z \approx 1$ and $T = 22°$ C [42].

Another transition concentration is the entanglement concentration, C_e ($C_e > C^*$). Above it, topological interactions dominate the dynamics of the solution. As a comparison to the C^* estimations, the entanglement concentration, C_e, for λ DNA has been showed to be both *ca.* 3–4 C^* [42, 43] and > $9C^*$ [44].

Unlike dilute solutions, the viscosity of semidilute and concentrated DNA solutions both vary with concentration. When the concentration rises above the overlap concentration, the viscosity increases drastically due to polymer entanglement [40]. While multiple power law relations of concentration and viscosity have been formulated for the temperature where the polymer solutions act ideally, $T = T_\theta$ (see [42] and [24]), it is unclear how the viscosity changes with increased concentration for other temperatures in aqueous solutions.

4. DNA Extension and Relaxation

"Ut tensio, sic vis"

Translation: "as the extension, so the force"

— Robert Hooke, 1678

In the devices of this work, the DNA samples are affected by many forces, often simultaneously. This chapter gives a brief overview on how DNA polymers extend in both flow and on surfaces. DNA relaxation is also briefly described. These concepts are important to understand the behavior of the individual DNA molecules.

4.1 Force-extension Relationship

There is an enormous number of ways a long polymer can be curled up in a relatively compact manner. Stretched out, there are much fewer possible conformations. If each conformation is given equal probability, it is much likelier that the polymer will be somewhat curled up. This purely entropic effect, will be acted against by other forces. If these forces are strong enough, the polymer will extend.

Figure 4.1 shows the extension of DNA as a function of exerted force. It starts in a coiled state and extends further and further as a larger force is exerted on it. The worm-like chain (WLC) model (see the previous chapter) describes this relationship accurately up to the overstretched regime. Marko and Siggia presented an interpolation formula based on this model [45, 46]:

$$\frac{F l_p}{k_B T} = \frac{1}{4}\left(1 - \frac{x}{L}\right)^{-2} - \frac{1}{4} + \frac{x}{L} \tag{4.1}$$

where l_p is the persistence length, F is the force, x is the extension and L is the contour length. While the WLC model describes the relationship well, the freely-jointed chain model has been shown to be able to predict the force-extension

behaviour of DNA at low forces but have failed to do this at moderate and high forces [47], as depicted in Figure 4.1.

As a DNA strand is being pulled at the two ends at higher and higher forces, the conformation changes. At low forces ($F < 0.08$ pN), the molecule is shaped as a coil and the deformability of DNA is mainly dictated by entropic elasticity [48]. At medium forces (0.08 pN $\leq F < 12$ pN), the DNA is stretched further with the bending rigidity dominating the behavior [49]. At around 12 pN, the molecules stretches to its full contour length [49]. However, it will continue to extend, if so very slightly, with higher force. Above approximately 65 pN, the DNA molecule becomes overstretched [50, 51]. DNA then transitions from the regular B-form into the S-form. At this point, DNA loses its double helical structure and opens up its base pairs. S-form is about 1.7 times the length of B-form [52].

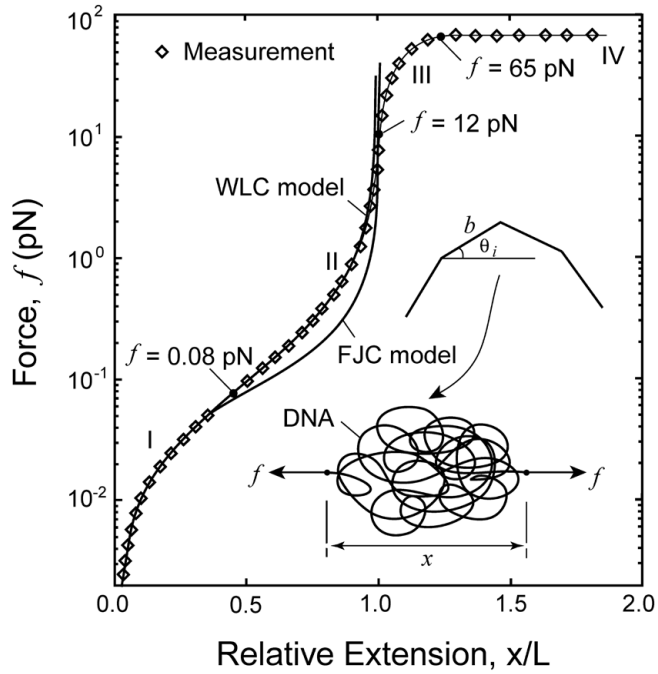

Figure 4.1. The relative extension of a DNA molecule as a function of force exherted. Four regimes have been identified: (I) entropic-elasticity domination ($F < 0.08$ pN), (II) wormlike chain (WLC, 0.08 pN $\leq F < 12$ pN), (III) contour elongation (12 pN $\leq F < 65$ pN) and (IV) B-DNA to S-DNA phase transition ($F \geq 65$ pN). Both worm-like chain (WLC) and freely-joined chain (FJC)-models are plotted to the experimental data. Reprinted with permission from Elsevier [49].

4.2 DNA Molecules in Flow

In the devices presented in this work, the type and magnitude of the flow stresses varies locally in the flow field. We can therefore expect flow dynamics elements from both shear and extensional flows.

When a DNA molecule is subject to a large enough shear flow or a flow velocity gradient perpendicular to the flow direction, it extends by the hydrodynamic drag forces acting on it along the flow direction. These drag forces overcome the entropic forces that keep the molecule in a coiled conformation as previously mentioned. As a result, the molecule is extended. However, Brownian motion can perturb the conformation so that the orientation is misaligned with the shear gradient. This will cause the molecule to rotate or tumble and return to the coiled state. Alternatively, it keeps extending for a while longer before rotating. Figure 4.2 depicts this progression in steady shear flow (constant flow velocity gradient perpendicular to the flow).

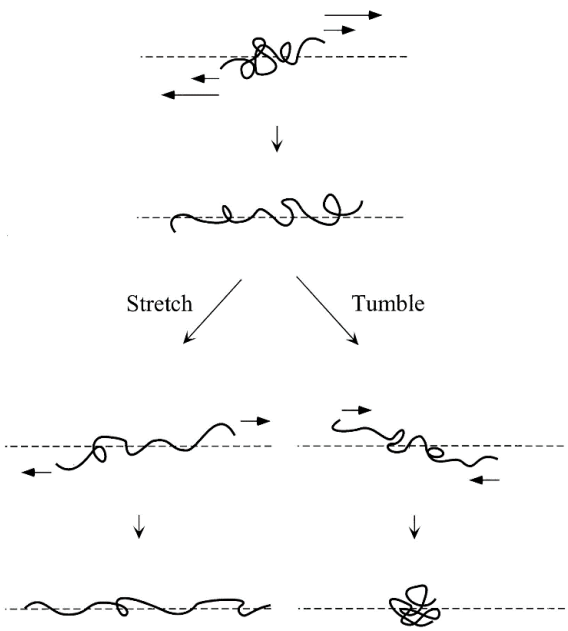

Figure 4.2. An illustration of long-DNA behavior in a steady shear flow. After an initial extension, Brownian motion can either tip the DNA to coil-up or to further extend. From [21]. Reprinted with permission from AAAS.

The tumbling frequency has been shown to be proportional to $Wi^{0.66}$ (where Wi is the Weissenberg number, see chapter 6) [53]. However, it is important to note that

the relative extension in the flow direction is not periodically repetitive like the tumbling frequency is [21].

In a pure extensional or elongational flow, there is a flow velocity gradient in the direction of the flow. A high enough strain rate elongates DNA strands, similarly to what happens in shear flow. Note however that DNA strands quickly reach full extension in extensional flow in a cross-lot geometry at high enough ($Wi > 50$) [54]. This is in contrast to shear flow where the average extension seems to saturate at around 40% [21].

The time to extension of long DNA has been shown to vary significantly between molecules of the same length. Even if subject to similar forces, the Brownian motion of the various parts of the molecules will change the conformations and the resulting extension of identical molecules is different. For example, molecules in a dumbbell conformation extend much more quickly than those that are folded like a hairpin in the direction of the flow [55]. The differing behavior of structurally identical polymers has been coined as "molecular individualism" by de Gennes [56]. This conformation-dependent dynamics have been shown to exhibit a strong conformation hysteresis, where the degree of extension under a given flow highly depends on the recent conformations [57].

4.3 DNA Relaxation

Following extension, DNA relaxes back to the energetically favourable coil conformation. The polymer relaxation time, τ_{relax}, is the time it takes for an ideal polymer chain to diffuse a distance of the order of its own size, according to the Zimm model [58]:

$$\tau_{relax} \approx \frac{R^2}{D_Z} \approx \frac{\eta}{k_B T} R^3 \approx \frac{\eta b^3}{k_B T} N^{3\nu} \tag{4.2}$$

where $R = bN^{\nu}$.

The relaxation time in equation (4.2) is from the Zimm model, where the use of a good solvent has been assumed and hydrodynamic interactions have been included. The relaxation time, τ_{relax}, has also been measured experimentally with single molecule fluorescence microscopy. In those experiments, DNA molecules were stretched out in shear flow and the relaxation back to a coiled state is observed after the flow is stopped. The relaxation time is then determined by fitting the extension-time curve to an exponential function [$x(t)^2 = c_1 \exp(-t/\tau_{relax}) + c_2$ where c_1 and c_2 are constants] [59]. For example, Smith *et al.*

measured a relaxation time of λ DNA to be 3.9 s and 19 s in a medium of 60 mPas and 220 mPas, respectively [21]. Assuming linear scaling of the relaxation time as a function of viscosity we can estimate τ_{relax} for λ DNA to be around 0.09-0.11 s for an aqueous buffer used in this thesis (1 mPas). This is about an order of magnitude lower than the value predicted using equation (4.2), *i.e.* 3.1 s. See Table 4.1 for relaxation time examples of common samples used in this work.

The Zimm and Rouse Models of Polymer Motion

The Rouse model and Zimm models are commonly referred to as "free-draining" and "non-free-draining", respectively. It means that in the Rouse model, the fluid freely passes through the polymer coil and thus "drains" it. The hydrodynamic friction or hydrodynamic interactions (HI) that the polymer experiences is then proportional to the number of polymer segments. Conversely, for the Zimm model, the fluid sees the polymer coil as an impassable solid object, with the consequence of the hydrodynamic friction proportional to the size of the coil. It then avoids "draining" the polymer interior. The Rouse model is accurate when the screening of HI is strong, such as in polymer melts or gels [35]. In this work, dilute, semidilute and entangled solutions are employed, and thus, the Zimm model is utilized.

Table 4.1. Relaxation times of DNA samples

The Zimm relaxation time from equation (4.2) and the scaled relaxation time are shown for several DNA lengths. A linear scaling of the relaxation time as a function of viscosity is assumed and the data used for the scaling are from [21]. The Zimm relaxation times are based on T = 23°C, buffer of I = 43.6 mM, unstained DNA using equation (3.6) and $R_g = \sqrt{R_F/6}$.

	1 kbp	10 kbp	48.5 kbp (λ DNA)	166 kbp (T4 DNA)
τ_{relax} (Zimm model)	3.3 ms	190 ms	3.1 s	27 s
τ_{relax} (scaled)	0.28 ms	9 ms	0.096 s	0.60 s

The relaxation of polymers in high-concentration solutions is much more complex than in the case of a dilute solution as described above. In such solutions, polymers no longer form entropically-favored coils as they do during dilute conditions. Perkins *et al.* was first to show evidence for reptation of single DNA molecules in a high-concentration (600 µg/mL) λ DNA solution. After they moved single molecules with an optical tweezer, the molecules relaxed back along their own contour, at a much slower rate than in a dilute solution [60].

The measurement of relaxation times of high-concentration solutions is complex and depends on the instrument used. In Papers III–V we used a stress-controlled

rheometer with a cone-plate geometry to measure the relaxation time of a 400 µg/mL λ DNA sample (*ca.* 1.43 s). While it gives a fluid-wide average of the relaxation time that can be used to compare the mean dynamics of the system it says little about the relaxation time of individual molecules inside the highly dynamic and flow with continuous changes in local DNA concentration viscosity and deformation rates.

4.4 DNA Stretching for Optical Mapping

A simple way of extracting genetic information coded in DNA is by fluorescently observing it. This is called optical mapping. By using different labelling schemes with fluorescent dyes or fluorophores, the overall structure of the genetic code can be revealed if the DNA is uncoiled and extended. This was achieved in Paper II, where long DNA molecules were stretched out on a surface after being isolated. While the DNA molecules in that paper were not labelled other than with non-specific fluorophores, the work proved the principle of combining sorting and stretching of long DNA. Follow-up work would use molecules labelled in a way to reveal genetic or epigenetic information.

The resolution in terms of number of base pairs of optical mapping is roughly the diffraction limited spot divided by the base pair length. By extending DNA, higher reading resolution is achieved[2]. The optical resolution using conventional fluorescence microscopy is around 300 nm or approximately 1000 base pairs for fully extended DNA.

There exist a multitude of ways to extend DNA for optical mapping. These include immobilization in a gel [61], nanochannel-based stretching [62], stretching using optical tweezers [47, 63], electrostatic surface-stretching or fluid fixation [64], DNA curtains [65, 66] and hydrophobic surface stretching or molecular combing [67, 68]. Figure 4.3 illustrates the relative extension gained from some of the commonly used methods. Among the above listed techniques, only nanochannels [69] and molecular combing [70] have been commercialized. In Paper II, molecular combing was utilized. It is described in the following two paragraphs.

[2] Assuming we have enough signal and fluorophore density, and that the DNA is not damaged in the process.

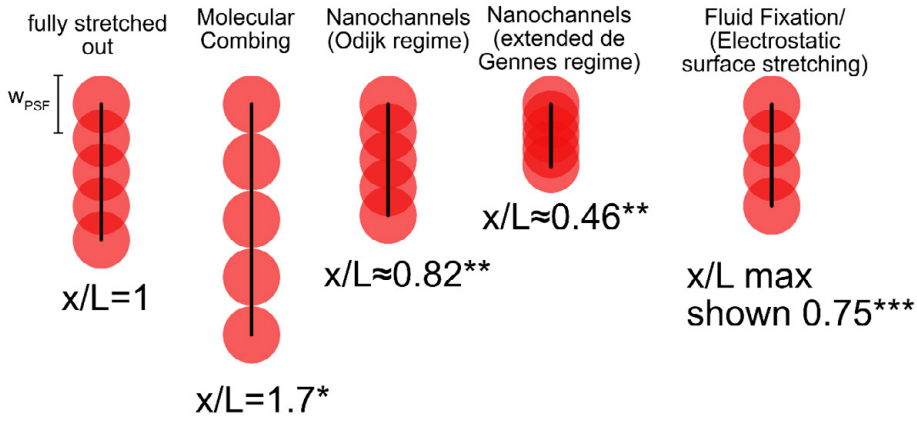

Figure 4.3. Comparison of the relative extension factor (x/L = extension/contour length) of selected DNA stretching methods Red circles corresponding to the point-spread-function of imagined dye molecules are placed with equal distance apart onto the black-colored DNA backbone. When the extension is short, the point-spread functions overlap and it is impossible to resolve the dye molecules. *Using a ZEONEX® substrate. **Using very low ionic strengths in 50 nm (Odijk regime) and 200 nm (extended de Gennes regime) wide channels [71]. ***The maximum shown relative extension using 164 kbp long DNA and a shear rate of 9000 s^{-1}. Theoretically, a longer extension could be reached if higher shear rates were used [72].

Molecular combing is based on dragging dissolved DNA molecules across a hydrophobic surface. The pH of the solution has been lowered (pH 5.5–6) to let the molecules undergo protonation [73]. The protonation opens up the DNA helix and exposes the hydrophobic interior. This happens particularly at the ends of the DNA molecule where the non-specific adsorption to hydrophobic surfaces is substantially enhanced. When the area that is covered with end-attached DNA molecules, is drained from liquid, the molecules stretch out onto the surface with the air-liquid meniscus.

In our research group, we stretch DNA using both nanochannels and molecular combing. While the nanochannel approach is effective at stretching DNA, molecular combing has a few advantages for the work in this thesis. Nanochannel-based stretching requires expensive and complex nanofabrication while the material for the molecular combing is simple and cheap to fabricate, only needing a hydrophobic surface. Molecular combing has the great advantage of providing the highest degree of information due to the high extension. With this method, B-DNA is stretched out to S-DNA, giving a relative extension (extension/contour length) of 170% [74]. This results in a high resolution of around 590 base pairs. See an example of molecularly-combed DNA molecules in Figure 4.4. These molecules exhibit a fluorescent barcode pattern that correspond to their base pair sequence. It was achieved through partial denaturation, see the work by Reisner *et al.* for more details on denaturation mapping in nanochannels [75].

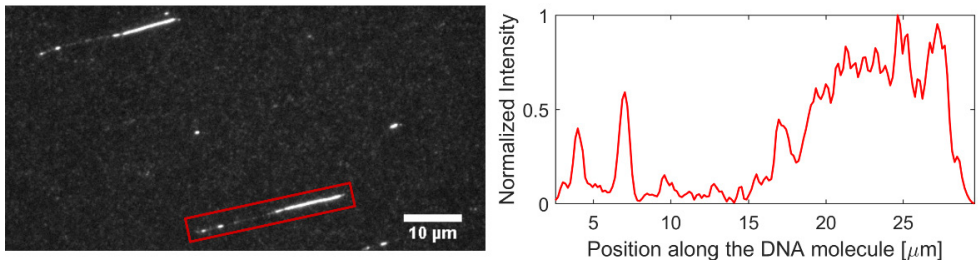

Figure 4.4. Denaturation-map of molecularly combed λ DNA molecules. Left panel shows a fluorescent micrograph of DNA molecules melt-mapped on a ZEONEX surface. Right panel shows a graph with the fluorescence intensity of the molecule with a bounding red box in the left panel.

5. DNA Separation in Deterministic Lateral Displacement

In the presented work, migration of long DNA across microarrays of pillars with circular-cross sections have been studied. The arrays have been used both as tools for length-based DNA separation in Deterministic Lateral Displacement (DLD) and for the study of elastic flow phenomena of DNA solutions. This chapter aims to give a brief introduction into the separation aspect of long DNA across DLD obstacle arrays.

5.1 Background

Gel electrophoresis, the first size-based DNA separation, was developed in the 1960s and 1970s. In the technique, the DNA sample was placed in a gel, *i.e.* a network of solid material placed in a liquid material. The microstructure is full of inter-connected pores where the DNA molecules migrate differently depending on their length under the influence of an electric field. Smaller molecules can travel faster while longer molecules travel slower due to a larger interaction with the obstacles between the pores. This is a form of chromatography, where the constituents of the mobile phase (DNA strands) are travelling at different rates in the stationary phase (gel). The DNA molecule mechanism of motion through the gel is called biased reptation. Standard gel electrophoresis works well for separating DNA shorter than 20 kbp in a practical amount of time (< 2 h). To separate strands longer than approximately 20 kbp in a reasonable time period, methods such as pulsed-field gel electrophoresis (PFGE) were developed. PFGE alternates the orientation of the electric fields which makes it possible to separate up to mega base pair long DNA. While PFGE works, it requires several days to work, it is very expensive and is dependent on trained personnel to work. Even with improved modern versions (see *e.g.* the products of Sage Science) that are cheaper, faster and automated, the run times are still in the range of tens of hours for 50 kbp samples and in the order of days for longer strands (see sagescience.com).

With the establishment of microfluidics in the 1990s, the research of size-based separation of long DNA was relocated from gels to microchannels.

Microfabrication technology allowed for well-defined structural design to the nanoscale with precise manipulation of single particles through applied forces such as hydrodynamic flow or electric fields. The migration dynamics of long DNA strands across obstacles in microchannels has been studied intensely (see the following reviews: [9, 24, 76-78]). DNA separation techniques based on novel mechanisms were developed. These include the Brownian ratchet [14], DNA prism [15] and Deterministic Lateral Displacement (DLD) [16]. DLD has been employed in this thesis and is described in more detail in the following subchapter. These techniques made it possible to continuously sort DNA into different collection buckets as they separated DNA spatially and not temporally as with gel electrophoresis. Continuous separation grants the possibility for an undisturbed automatic processing over a long time.

There are a number of factors influencing the migration dynamics of DNA across obstacle arrays. Pillar size, pillar spacing, pillar regularity and driving force type and strength are known to significantly affect the behavior of DNA. A systematic study of the effect of these parameters has not yet been carried out [78]. DNA migration through obstacle arrays thereby remains largely an unexplored area of science.

Most of the existing research has focused on DNA migration under the influence of electric fields. In this work, pressure-driven flow has instead been utilized. While it is debatable, pressure-driven flow can be seen as more practical to work with as it is the fluid together with the DNA strands that is transported rather than solely the DNA strands. This keeps the processed DNA strand concentration constant and minimize aggregation that could occur due to ultra-high sample build-up. It is important to note that the vector field of hydrodynamic flow differs significantly from that of electric fields. There is no shear gradient in an electric field in a straight microfluidic channel. Rather than extend like they would do with hydrodynamic flow, long DNA strands have been observed to compress [79]. While it is possible that both modes of migration could work for high-throughput DNA separation in DLD, it remains to be shown for electrophoresis-driven migration.

5.2 Deterministic Lateral Displacement

Deterministic Lateral Displacement (DLD) is a continuous particle sorting technique, developed by Huang *et al*. in 2004 [16]. It has been demonstrated to separate micrometer-sized particles down to a resolution of astounding ~10 nm [16]. It has been used to isolate, concentrate and sort many kinds of biological particles, see the recent reviews for an extensive overview of the DLD field [80, 81]. What makes DLD exceptional is its simplicity. It does not rely on external

forces other than the forces required to create a flow. Instead, it exploits the predictability of laminar flow combined with steric interaction of the particles with micro pillars. Figure 5.1 depicts a simplified scenario of DNA separation in DLD. A mixture of short, medium and long DNA is injected into the sample inlet. All three samples end up in different outlets after flowing across the obstacle array. Short fragments zigzag between the pillars in the direction of the flow and exit at the same lateral position as they entered the array. In contrast, longer fragments displace laterally across the array and end up in a the other end of the array. Medium long fragments however, display both zigzag and displacement events and end up in the middle outlet. While this scenario will ensue for a particular flow velocity, altering the flow velocity will change the likelihood of zigzag/displacement events and shift the trajectories and outlet positions.

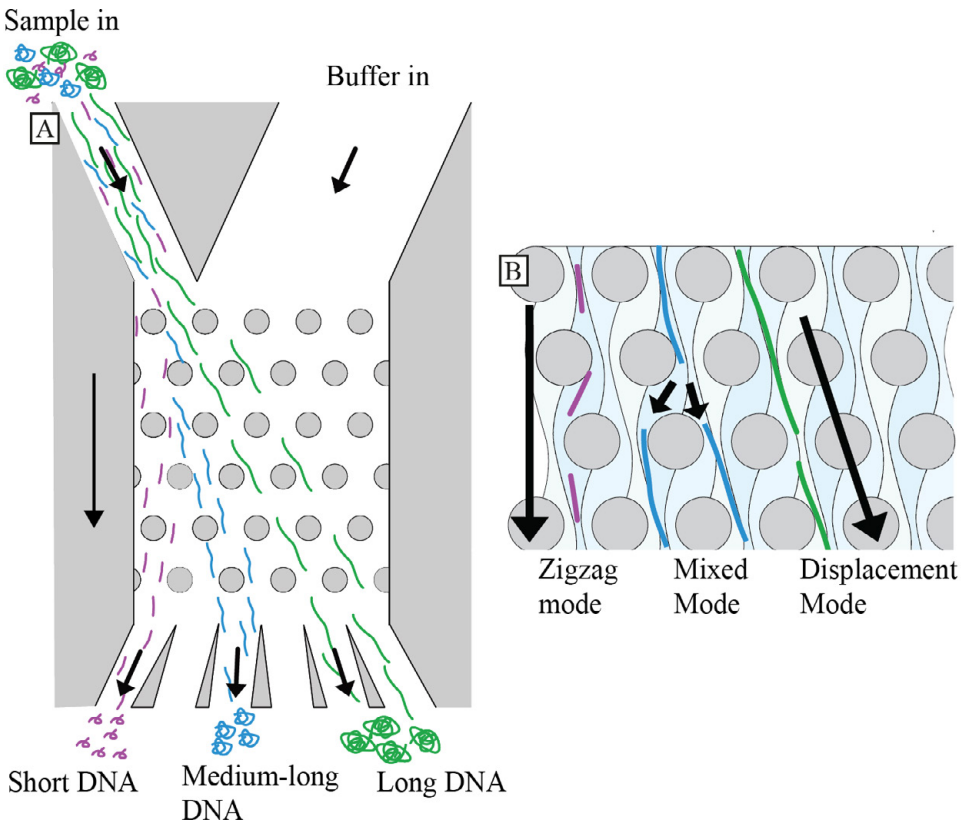

Figure 5.1. Schematics of length-based sorting example of DNA molecules with DLD. (**A**) DNA strands of 3 sizes are sorted in a DLD device for a particular flow velocity. The long DNA fragments (green) are displaced laterally while the short DNA fragments (magenta) zigzag between the pillars in a trajectory in line with the flow direction. The medium-long strands (blue) show both zigzag and displacement behaviour, ending up between the short and long fragments. The trajectories can be altered by adjusting the flow velocity. (**B**) Zoomed-in schematic of the three modes: zigzag, displacement and a mix of the two.

The obstacle array in DLD consists of many rows of pillars. Each row is laterally shifted a distance $\Delta\lambda$ in relation to the previous row. This row shift causes a bifurcation in the flow, splitting it into multiple streams. The number of streams is equal to the periodicity, N, ($N = \lambda/\Delta\lambda$, where λ is the pillar center-center distance). Figure 5.2 both illustrates a DLD unit cell and the stream bifurcation with $N = 3$.

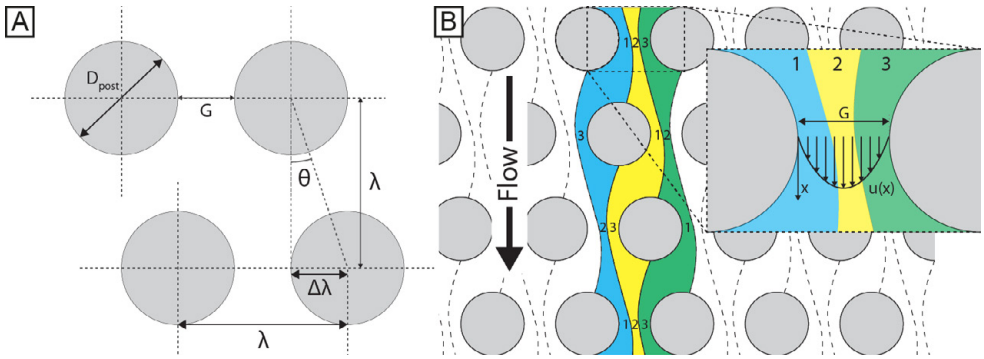

Figure 5.2. Geometry of an DLD array (A) and the flow through an example array with three stream lanes (B). The window in (B) illustrates the parabolic flow profile. Figure adapted from [18] with permission.

5.3 Critical Size

The salient feature of a simple DLD device is that it sends particles in two direction depending on their sizes in relation to the threshold size of the device. This threshold size is commonly referred to as the critical size.

Particles entering a DLD array will, in the simple case, either continue with a zigzag trajectory along a given flow stream or be displaced to a neighbouring stream at every *N*:th pillar. For the simplest of particles, a non-deformable or hard sphere, the outcome is determined by a cut-off or critical diameter, D_c. Inglis was the first to derive a formula for it [82]. Davis later improved on this formula empirically [83]:

$$D_c = 1.4 \cdot G \cdot \left(\frac{\Delta\lambda}{\lambda}\right)^{0.48} \tag{5.1}$$

where G is the gap between the pillars. This displacement using equation (5.1) is deterministic and will theoretically happen the same way every time for hard spheres. However, for more complex particles, the separation is not as simple. If the particles are asymmetric in shape or deformability, they could exhibit both

zigzag and displacement modes in the same device. This transport mode is referred to as “mixed” [84, 85]. Note that this mixed behavior has also been shown to occur for hard spheres both experimentally [16, 84, 86] and through simulations [84, 85, 87]. Kulrattanarak *et al.* proposed it happens due to asymmetric flow distributions leading to varying flow profiles across the length of the array.

5.4 Impact of Diffusion

The purity and recovery of separation in DLD worsens with particle diffusion. Similar to other microscopic objects, DNA molecules fluctuate randomly in a liquid as a result of other molecules hitting them from all directions. This is important to be aware of because it sets an upper time limit of the separation. Diffusion allows for the particles to move across stream lanes. This causes the number of possible trajectories to broaden for a given sample and leads to a greater lateral overlap between sample distributions at the end of the array. However, the impact of diffusion differs for zigzag and displacement modes [88]. The effect on particles migrating in a zigzag mode is a simple lateral broadening of the trajectories. For displacement, is it different. The particle position between the pillars resets at every row. The only way for diffusion to have an impact on the trajectory is if the displacing particle diffuses into the first lane (zigzag path) during migration between rows.

We can estimate the magnitude of Brownian motion of long DNA molecules with the Zimm model of polymer dynamics. In it, the segments interact with the solvent and with each other indirectly through the solvent interactions. The DNA size is approximated with $R \approx bN^{\nu}$ where b is the Kuhn length, N the number of Kuhn segments and ν the Flory exponent [35]. The Zimm friction coefficient for the polymer chain then becomes $\zeta_Z \approx \eta R \approx \eta b N^{\nu}$ where η is the viscosity of the medium. The prefactor is removed since it is different from case of a sphere. The Zimm diffusion coefficient becomes (Stokes-Einstein equation) [58]:

$$D_Z = \frac{k_B T}{\zeta_Z} \cong \frac{k_B T}{\eta R} \approx \frac{k_B T}{\eta b N^{\nu}} \tag{5.2}$$

where k_B is the Boltzmann constant, and T the temperature.

While the Zimm model gives a good estimate of the diffusion coefficient of long DNA, it can also be measured experimentally. Single molecule experiments have been conducted where trajectories of the Brownian motion of single DNA molecules are tracked [37, 89]. The mean squared displacement ensemble of these molecules’ displacement gives a diffusion coefficient using the Einstein relation. It

is important to be aware that the measured diffusion coefficients are larger than the ideal coefficients, predicted by the Zimm model in equation (5.2).

The impact of diffusion to DLD separation is especially relevant for small particles with large diffusion coefficients. It is not uncommon that the DNA samples reside 10 min in the devices used in this thesis. During this time, λ DNA (48.5 kbp) will diffuse about 24 µm in 1 dimension (using a diffusion coefficient, $D = 0.47\ \mu m^2/s$ [37]). Compare this to a YOYO-1 dye molecule ($D = 290\ \mu m^2\ s^{-1}$ [90]) and an *E. coli* genome using equation (5.2) with the pre-factor for good solvents from [40]). These will instead diffuse approximately 290 μm and 3.5 µm respectively. Based on these known diffusion distances, the devices have been designed and run accordingly.

5.5 Displacement of DNA

DNA separation was first demonstrated in DLD in the pioneering work by Huang *et al.*. In it, two bacterial artificial chromosomes (BAC, 61 kbp and 158 kbp) were isolated from each other using an electric field as a driving mode [16]. While the technique worked well to separate the two BAC, it did this at very low flow velocity (calculated approximately 20 µm/s). This prevented the technique from being practically useful for separating DNA as the throughput was too low to process enough sample needed for different kinds of genetic analyses following the separation. Eleven years later, in 2015, Chen *et al*. [91] demonstrated pressure-driven DNA DLD and doubled the working flow velocity where long DNA strands are displaced by adding polyethylene glycol (PEG) to the sample. PEG compacts DNA and reduces shear-induced extension. The extension of DNA was hypothesized to result in decreased displacement. While the work by Chen *et al.* increased the throughput, they did so very slightly (only up to a flow velocity of 40 µm/s). In addition, introducing a high concentration of PEG molecules to the sample is not optimal as it could be difficult to wash away if so required by post-separation analysis.

In 2019, Wunsch *et al*. presented hydrodynamic separation of DNA using nanoscale DLD arrays [13]. By reducing the dimensions from micrometers to hundreds of nanometers, they were able to separate DNA in the range of 100 bp–10 kbp with a resolution of 200 bp. They were able to achieve this separation with unprecedented flow velocities (up to approximately 1 mm/s, depending on the fragment size and the degree of overlap). The outlet position of a given DNA size was also showed to be tunable based on the flow velocity. However, the throughput was very low as the cross-sectional area of the channel is minimized by using nanoscale devices. They were able to circumvent this by massively parallelizing the DLD arrays. Parallelizing nanoscale devices requires advanced

cleanroom facilities which can be very expensive. Interestingly, while they were able to displace DNA as long as 48.5 kbp at high flow velocity (~1 mm/s) with gap sizes up to around half a micrometer, they reported that the displacement breaks down when using microscale gaps. In can be contrasted to the work presented in Paper I that is performed with micrometer-sized gaps. See Table 5.1 for a comparison of important parameters of pillar array-work for DNA separation.

Table 5.1. Comparison of key parameters and results for microfluidic pillar-based long-DNA displacement or separation. To put the comparison to a wider context, the conventional gel-based technique pulsed-field gel electrophoresis (PFGE) is also included. The table only compares the values for a single array which could be increased by parallelization. When the DNA migration is driven with an electric field, an effective flow rate and throughput is calculated by multiplying the migration velocity with the cross-sectional area of the array (depth × pillar gap × number of gaps).

Ref.	Experiment and sample	Pillar gap size (μm)	Highest Flow velocity or migration velocity (μm/s)	Highest flow rate (sample inlet) (μL/h)	Highest sample throughput (ng/h)	Sample Conc. used for highest throughput (μg/mL)
Paper I	DLD (pressure-driven), 166 kbp & 48.5 kbp	2.9	34 000*	24	760	8+24 = 32
Huang *et al.[16]*	DLD (electrophoresis), 158 kbp & 61 kbp	3	20	~0.04‡	~0.12‡	3
Chen *et al.* [91]	DLD (pressure-driven), 166 kbp	1.7	40 (with PEG) ¶	~0.21§	~0.002§	0.01
Wunsch *et al.* [13] †	DLD (pressure-driven), 48.5 kbp	0.078–0.75	1500#	~0.03	~0.03 **	1–5
Huang *et al. [15]*	DNA prism (electrophoresis), 209 kbp & 61 kbp	2	~400 ‡‡	~1	~100	~10
Doggett *et al.* [92]	Pulsed-field gel electrophoresis (PFGE) ††	-	-	0.05–0.2	0.4–16	80

* Mean flow velocity between the pillars. ‡ Effective value based on an estimate assuming a 0.3 mm wide inlet channel and 5 μm deep device. §Value based on the peak flow velocity 40 μm/s and interpolation based on the corresponding reported flow rates. ¶ Calculated peak velocity between the pillars assuming a parabolic flow profile. The device also only worked with the addition of PEG as a condensation agent. # The reported velocity is based on particle tracking of the DNA molecules. † Wunsch *et al*. also connected 1024 of their arrays in parallel to achieve higher throughput. ** Value based on an estimate assuming a 0.5 μm deep device. ‡‡ Value based on assuming a migration distance of 6 mm. †† Assuming a gel plug of 800 μL (standard Bio-Rad volume), a highest concentration of 80 μg/mL (see [9]) and run times between 4h and a week. Table is reproduced from [93] (no permission required).

A simple model for DNA displacement in DLD is based on comparing the short axis diameter of the DNA "blob" to the critical size of the DLD array [91]. The model says that if in a DNA strand is in its coiled state and the small axis diameter is wider than the critical size, the DNA strand will displace. If on the other hand, the DNA strand is extended by shear forces to a degree where the diameter becomes smaller than the critical diameter, it will zigzag. While in our experiments, we do observe molecules that are more in the coiled conformation to displace more, we also observe stretched-out molecules to displace (at flow velocities up to 34 mm/s). This simple model can then be discarded in favor for a model that would also include other mechanisms.

There are many effects that could affect the behavior of DNA in DLD. One category of effects are derived from the type of flow inside the array. The flow across the pillar array is a hybrid between shear and extensional flow. Figure 5.3 illustrates the Newtonian flow profile in the DLD pillar array, where velocity gradients both along and perpendicular to the flow are visible. As described in subchapter 4.2, DNA molecules have been shown to periodically tumble and extend in a shear flow [21]. They have also been shown to extend in an extensional flow [54]. Other effects that could affect DNA trajectories in DLD include hydrodynamic and entropic wall migration which forces the strands away from solid walls. In addition, DNA strands are also known to interact with micro pillars sterically (*e.g.* through hooking events) or electrostatically (DNA is negatively charged).

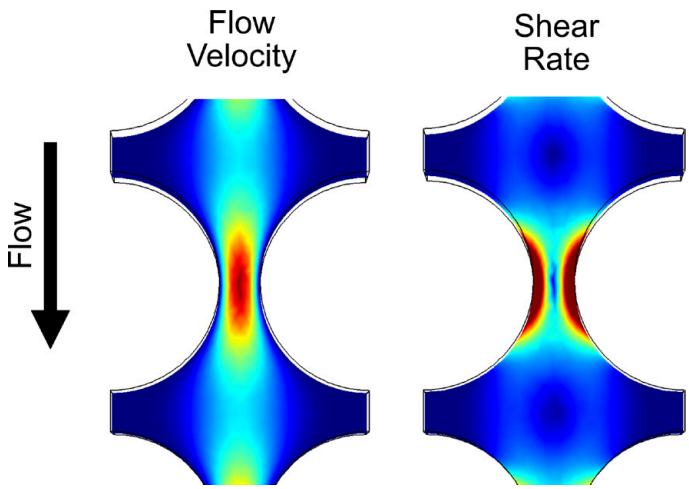

Figure 5.3. Finite Element Simulations of Newtonian fluid flow in a DLD unit cell. Left side shows the flow velocity profile whereas the right side shows the shear rate profile. Both a shear gradient and an extensional gradient is visible. Redder represents a higher value and bluer a lower value.

The conformational changes are predicted to be complex due to conformational hysteresis as the DNA strands flow between pillar gaps. Figure 5.4 illustrates two contrasting behavior and the conformational unpredictability for two DNA molecules from the same homogenous sample. One strand (Figure 5.4A) stays mostly in a blob conformation except at the higher flow speeds at the high flow velocity region, as depicted in Figure 5.3A, where the DNA is slightly extended. The other strand (Figure 5.4B), is more extended and exhibits a large rotation.

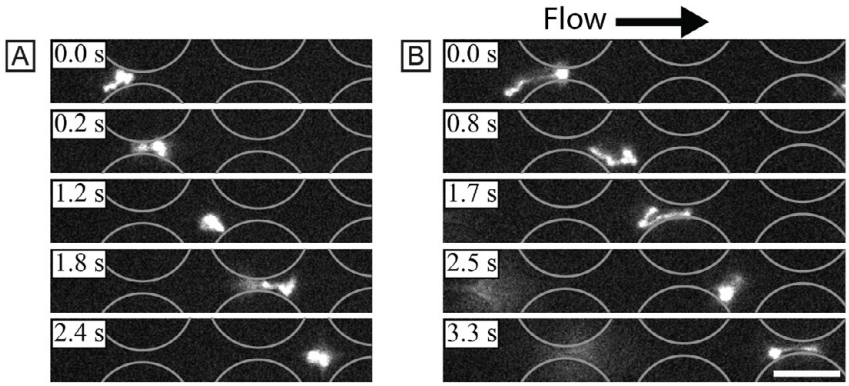

Figure 5.4. Fluorescent micrograph time series of long DNA flowing across DLD pillars. The molecule mostly stays in a coil configuration in (**A**) whereas in (**B**) a larger degree of extension and rotation can be visible.The DNA length is 166 kbp or 65 μm fully extended. The mean flow rate is approximately 21 μm/s. Scale bar is 10 μm.

Many of the above mentioned effects are likely to push DNA strands into a higher likelihood of displacement as the only condition for displacement is that the DNA strands migrate from the stream lane closest to the wall to one further away. The shear-induced periodic tumbling is very likely to increase displacement as rotation has been demonstrated to increase displacement for cell clusters [94]. Electrostatic repulsion has been shown to increase the likelihood of displacement in DLD for charged nanoparticles [95]. We have utilized lower ionic-strength buffers in Paper I to enhance to displacement.

Many effects are also enhanced with increased polymer length. Wall migration has been shown to be faster with longer DNA molecules [96]. Longer molecules have a longer relaxation time and are thus more sensitive to conformational hysteresis when the time for flowing between pillar gaps is much shorter than the relaxation time. Long molecules are also more likely to interact more with the pillars as they are larger.

The combination of all possible effects that could affect DNA in DLD makes it difficult to predict the trajectories across the array theoretically or numerically. In Paper I, we demonstrate that the Davis equation [equation (5.1)] is not an all-encompassing design parameter for predicting for long-DNA trajectories as it is for hard microspheres. Two devices with similar critical diameter exhibited very different result. A device with $N = 50$, $G = 2.8$ μm and $D_c = 0.60$ μm displayed displacement of 166 kbp long DNA at much higher flow velocities than a device with $N = 20$, $G = 2.2$ μm and $D_c = 0.74$ μm (4.1 mm/s compared to 40 μm/s), see Paper I.

5.6 Throughput

There are multiple ways to increase the throughput of DLD in order to collect large enough sample quantities for subsequent DNA analysis (see text box below). The two main alternatives are to either increase the volume that is being processed in a given duration or to increase the sample concentration. A third way to increase the throughput is to place arrays in parallel and thus increase the processed sample volume.

What is a large enough DNA sample throughput?

It depends on the scientific question in mind and on the analysis tool which to analyze the DNA with. For SYBR™-gold-based gel electrophoresis, as small as 20 pg of DNA is sufficient for detectable bands. For long-read nanopore sequencing (from Oxford Nanopore Technologies), an input DNA mass of 0.4 µg to 10 µg is commonly recommended, depending on the protocol.

Increasing the volumetric throughput can be achieved by increasing the cross-sectional area of the array or by increasing the flow velocity. In Paper I, we use arrays consisting of micrometer-sized gaps. This increases the throughput about 100 times compared to gaps 10 times smaller (*e.g.* used in nanoDLD [13]). We also explore the effect of high flow velocity in Paper I and show that we can displace long DNA up to approximately 34 mm/s that correspond to a throughput of 760 ng/h.

The second alternative of increasing the sample throughput is instead by increasing the sample concentration. It should however be done with caution as high concentration could worsen the separation in DLD due to the non-deterministic behavior caused by a high number of particle-particle interactions. For example, DLD separation of concentrated red blood cells has been predicted to break-down due to cell-cell collisions [97]. It is important to estimate this effect if one is to work at higher concentration. For example, Holm *et al*. showed that it is possible to still perform micro particle separation in a background of blood up to 45% hematocrit. However, they found that trajectories shifted and broadened for the particles close to the critical diameter [98]. It is also important to note that the viscosity increases when the particle-particle interactions become significant. While one should be wary of negative effects arising with high sample concentration, an experimental sweet spot can be found where throughput can be significantly increased with limited drawbacks.

It is previously not known how high concentration affects the behavior of DNA in microfluidic pillar array separation techniques. We have explored this in multiple articles. In Paper I, we vary the concentration of 48.5 kbp and show decreased separation from short DNA (0.25 kbp to 10 kbp). However, the displacement is

enhanced which we show for *e.g.* 166 kbp long DNA. In Papers III–IV we present viscoelastic behavior that arises from molecule-molecule interactions (see more details in next chapter).

5.7 Flow-induced DNA Fragmentation

The DNA separation in this work employs very high flow velocities. While it increases the throughput, the large hydrodynamic forces could also lead to breakage of the DNA molecules that are processed. While we have not observed significant fragmentation at even the highest applied pressures (3 bar, corresponding to flow velocities up to ~34 mm/s, see Paper I), it is possible that even longer DNA samples (*e.g.* mega base pair DNA) could be fragmented at these high flow velocities in our devices.

Long DNA molecules are known to fragment at high shear rates when pipetting [11]. In fact, this is a method commonly used to break up DNA before sequencing with methods that require short fragments. More recently, microfluidic techniques have been developed where long DNA molecules are deliberately fragmented by the passing through constricted pores [99, 100]. Note that we reduce the likelihood of fragmentation in our devices by employing large pillar diameters to minimize breakage due to rope-over-pulley snaring. We also use large microscale gaps (compared to *e.g.* nanoscale gaps) which reduces the shear rate. Lastly, short pore gaps [99] and rounded constrictions (resulting in a more gradual increase in the deformation rates) [100] such as used in our devices have also been showed to lead to a lower degree of long-DNA fragmentation.

In addition of fragmenting by the flow forces, the DNA molecules are subject to breaking by photodamage as we are using illuminating the sample to observe the DNA separation. This is however not a significant problem when the molecules are travelling at high flow velocities with minimal light exposure and anti-bleaching agents such as β-mercaptoethanol are used. When the separation parameters have been optimized, the separation will not need to be observed and photodamage will not be an issue.

6. Viscoelastic fluids in Pillar Arrays

"All models are wrong but some are useful"

— George Box

When polymers such as DNA are added to a solution, they can exhibit strong elastic behavior. Each DNA strand can be seen as a sequence of springs which can store energy when stretched by *e.g.* a flow. When a polymer solution is inserted into a microfluidic channel with complex geometry such as a pillar array, its elastic components affect the flow immensely. Large temporal and spatial flow instabilities can form. Such effects are important to be aware of when engineering devices for DNA separation or the manipulation of DNA in other ways. These effects can either be a disturbance to sorting as shown in Paper I or be exploited to study new flow phenomena as in Papers III–V. This chapter gives an overview of viscoelastic fluids and elastic turbulence around both individual micro pillars and through micro-pillar arrays.

6.1 Viscoelastic fluids

In a microfluidic channel, viscous fluids such as water will almost immediately cease to flow if the applied pressure driving the flow is stopped. Viscoelastic fluids such as high-concentration DNA solutions however, will not. The DNA strands can be seen as tiny springs which stretch more or less at sufficiently high flow rates. When the driving force of the flow is removed after running for a while, the DNA strands take some time to return into their relaxed state. This elastic component gives rise to interesting mechanical properties both on an individual polymer level and for the entire polymer solution.

Viscoelastic fluids are said to have a memory with a characteristic timescale that corresponds to the longest relaxation time. The relaxation time can be very long, hours or even days, depending on the fluid. They display hysteresis, where the shear stress for a viscoelastic fluid depends on all the previous shear rates. This is unlike a Newtonian fluid like water or honey where the shear stress at a moment in time is only dependent on the shear rate at that particular instant.

Shear thinning and extension thickening

The shear stress of a viscoelastic fluid is not proportional to the shear rate such as it is for Newtonian fluids. Polymer solutions are known to exhibit a decrease in the hydraulic resistance when subject to shear flow (see *e.g.* data for λ DNA solutions [101-103]). This is known as "shear-thinning" of the viscosity. The shear-thinning can lead to a viscosity reduction of several orders of magnitude. Conversely, when polymer solutions are subject to regions of strong extensional flow, the viscosity can increase dramatically. This is known as "extension-thickening". This has been shown for *e.g.* polystyrene solutions. This occurred when the extensional rate exceeded the inverse Rouse relaxation time. [104].

To simplify the study of viscoelastic fluids, the behavior of the flow and fluid constituents (such as polymers) can be characterized by a set of dimensionless numbers, which indicate system-wide average flow behavior, see an overview in Table 6.1. The first one, the Reynolds number, was introduced in chapter 2.

The second dimensionless number of relevance is the Deborah number, *De*. It is the ratio of the relaxation time to the time of observation (or characteristic time for a transient deformation process). Deborah number owes it names from the prophetess Deborah who proclaimed in the Old Testament that "the mountains flowed before the Lord". Given long enough passing of time, in the time scale of a god rather than with mere humans, even the mountains will flow. Thus, the observation time is important to judge the rheological behavior of the object. If the relaxation time is long and the observation time short, the object can be regarded as a solid. Conversely, if the relaxation time is short and the observation time is long, it can be regarded as fluid. A good example is the silicone polymer Silly Putty which behaves like an elastic solid and bounces over a short time period and flows like a liquid over a long time period.

The observation time used for *De* highly depends on the type of flow. For a steady shear flow, the time of observation is infinite, and thus, *De* is zero. In an oscillatory flow (like the one that exists in the pillar arrays in Papers I–V) the period of oscillation is a meaningful choice of observation time (time for the fluid to travel between pillar gaps). On the other hand, if the flow is across a single pillar in a channel (as in Paper IV), the time for passing the pillar is a more relevant alternative.

The third dimensionless number in this thesis is the Weissenberg number, *Wi.* While this number is not actively used in any of the thesis papers, it is widely used in DNA flow dynamics literature and useful when comparing the different dimensionless numbers. *Wi* is a measure of the relative magnitudes of the elastic to the viscous forces in a viscoelastic fluid, *e.g.* a polymer solution such as a DNA solution. Polymers impart elastic properties to the fluid which can be quantified

with Wi. $Wi > 1$ is enough for shear flows to overcome the entropic elasticity and extend a polymer molecule [77].

Note that the usage of De and Wi varies in literature and can be defined differently. The definition of De here is sometimes the same as the definition of Wi elsewhere. The reviews by Poole [105] and Dealy [106] are insightful to understand the historical and widespread differences in definition and usage of the two numbers.

The ratio of the Deborah number (and sometimes *Wi)* to the Reynolds number is called the Elasticity or elastic number, El. This is the fourth relevant dimensionless number. It describes the relative magnitudes of the elastic to the inertial forces. At large El, the system is dominated by elastic effects such as elastic turbulence (see next subchapter). El is independent of the flow velocity and is heavily affected by the characteristic length scale of the system ($El \propto l_0^{-2}$). We can thus expect huge El in our small microfluidic channels. El is also determined by the polymer relaxation time and the fluid viscosity, both rapidly increased with increased polymer concentration.

Table 6.1. Dimensionless numbers relevant to this thesis

Here ρ is the density of the fluid, η is the viscosity of the fluid, l_0 is the characteristic length scale (often the hydraulic diameter of the channel), u_0 is the characteristic velocity (often the average flow velocity), $\dot{\gamma}$ is the shear rate and τ_{relax} is the relaxation time of a polymer.

Dimensionless number	Interpretation	Equation	Significance	Eq. No.
Reynolds number	$\frac{\text{inertial forces}}{\text{viscous forces}}$	$Re = \frac{\rho l_0 u_0}{\eta}$	≪1 laminar flow >2000 inertia dominates	(6.1)
Deborah number	$\frac{\text{polymer relaxation time}}{\text{characteristic deformation time}}$	$De = \frac{\tau_{relax}}{\tau_{flow}} = \frac{\tau_{relax}}{l_0} u_0$		(6.2)
Weissenberg number	$\frac{\text{elastic forces}}{\text{viscous forces}}$	$Wi = \tau_{relax} \cdot \dot{\gamma}$	>1 coil-stretch transition can occur	(6.3)
Elasticity number	$\frac{\text{elastic forces}}{\text{inertial forces}}$	$\frac{De}{Re} = \frac{\tau_{relax}\eta}{\rho l_0^2}$	≫1 elastic turbulence	(6.4)

In Papers III to V, the elastic effects from the DNA solution give rise to high local variation in the local DNA concentration, viscosity and flow velocity. These variations occur both spatially across the array and through time for a fixed

location. The dimensionless numbers that have been used are based on system-wide averages and do not give an accurate representation of the flow at a local scale. While being interpreted as such, their numerical values are still useful as a guiding principle when designing experiments and microfluidic tools and comparing the flow to the works of others.

6.2 Introduction to Elastic Turbulence

Irregular flow patterns have for a long time been observed at small Re ($Re \ll 1$) for polymer solutions. Generally, when Re is small, inertia can be disregarded and the flow becomes laminar (see chapter 2). However, adding a tiny fraction of polymers is all that is needed for the flow pattern to become turbulent at sufficiently high flow velocity (but still too low for the inertia to play a significant role). When discovered, this inertia-free turbulence was dubbed "elastic turbulence" [107]. Since the discovery, it has been demonstrated in a large number of various flows and geometries (see the reviews: [108, 109]).

A general trend for the magnitude of flow instabilities of systems with elastic turbulence is that the instabilities increase in magnitude with a higher mean flow velocity (often reported as Wi or De). One such instability is an elastic flow vortex. Similarly to flow velocity fluctuations, vortices have been reported to emerge, grow and become unsteady with increasing Wi in a number of different microfluidic geometries. These include micro-contractions [110-117], confined single micro-pillars [118-122], confined pairs of micro-pillars [123, 124] and micro-pillar arrays [125].

Elastic turbulence differs significantly from inertial turbulence in the way the energy is dissipated. Inertial turbulence starts off with larger vortices or eddies. These eddies generate smaller eddies which in turn drive even smaller eddies to form. Eventually, the energy is dissipated as heat (see Kolmogorov Theory [126]). Elastic turbulence works in the opposite direction. It begins with flow disruption at the smallest length scale (single polymer level). This disruption can then drive the formation of larger instabilities such as eddies and large-scale flow disturbances. This energy length scale hierarchy is very visible in Papers III–V with a sequential emergence (with increasing flow velocity) of smaller flow disturbances, vortices and finally large-scale waves.

Pure elastic instabilities have mainly been reported with curved streamlines of the flow. When polymers are stretched out along curved streamlines, the normal forces that act against the extension are directed radially inwards (called "hoop" stresses). The polymers are then forced to move towards the center of the curvature which causes disturbances in the flow. Note that elastic instabilities have

also been shown to occur in a straight channel without curved streamlines provided that the flow has been perturbed upstream in the channel [127, 128].

The onset and magnitude of the elastic instabilities (usually reported with the variance of temporal and spatial flow velocities) have been related to the characteristic curvature flow length scale, where smaller curvatures result in larger fluctuations [129, 130] [compare to equation (6.4)]. Microfluidic pillar arrays with very small gaps (approximately 2–3 μm) as used in the papers presented here are then likely to generate large flow fluctuations.

6.3 Elastic Turbulence around Single Pillars

While the work in this thesis has mainly been focused on flow across pillar arrays, understanding the simpler geometry of a single pillar might give insight into the more complex one. The flow around a single pillar in a straight microfluidic channel is a benchmark that has been extensively investigated with both Newtonian and elastic fluids.

The flow pattern of a viscoelastic fluid around a single pillar changes considerably with increasing flow velocity. The following scenario has been reported by multiple authors [118, 119, 121]: At very low flow velocity, the flow around pillars for a viscoelastic fluid is laminar without a trace of turbulence. At a critical flow velocity (usually referred to with a Wi value), a downstream flow instability emerges. This is typically a long and unstable wake. At an even higher flow velocity, an upstream flow instability appears. This instability usually manifests as a single vortex or a set of two vortices. The vortices have been reported to grow in size and instability with increased flow velocity. They have also been observed to exhibit a periodic cycle of growth and shedding when the flow velocity exceeded a critical threshold [118, 125]. This progression of behavior has been reported to occur both upstream of single pillars (pillar radius of 32.5 μm and pillar gap 17.5 μm with polyethylene oxide in glycerol solution [118]) and in the gaps of pillar arrays (pillar radius of 131 μm and gaps 108.5 μm or 217 μm with a hydrolysed polyacrylamide solution [125]). In Papers I, III, IV and V, we observed the same progression for long-DNA solutions in both sparsely and densely distributed pillar arrays.

Significant flow asymmetry have also been observed at high Wi in the flow around single [122, 131] and pairs of micro pillars [132]. Such flow asymmetry is very likely occurring in the DNA waves which are demonstrated in the pillar arrays of Papers III–V. Shen and co-workers put forth a mechanism that can explain the emergence of an asymmetric flow state [133]. It is illustrated in Figure 6.1 with the following progression:

1. At a critical Wi, there is a large build-up of tensile stress at the downstream side of a pillar.
2. This stress causes a disturbance to either side that moves the downstream wake to one side.
3. At the side with the wake, the flow resistance is increased due to the extensional thickening occurring in the wake.
4. As a result, the flow resistance on the side without the wake is reduced with an increase in the shear rate. This leads to shear-thinning which further reduces the flow resistance and results in a feed-back effect that amplifies the flow asymmetry.

Note that the authors of the proposed mechanism above reports that the fluid has to be shear thinning at the side of the pillar and extensional thickening in the wake of the pillar for the flow asymmetry to arise. This means it would not work with a fluid without significant shear thinning (called Boger fluid, see subchapter 6.4) such as the one used in Paper III. However, in the work with the Boger fluid of Paper III, asymmetric flow is still observed in the experiment. This indicates that there might also be other factors involved in generating the asymmetry. A more detailed investigation is needed to determine all the contributing factors.

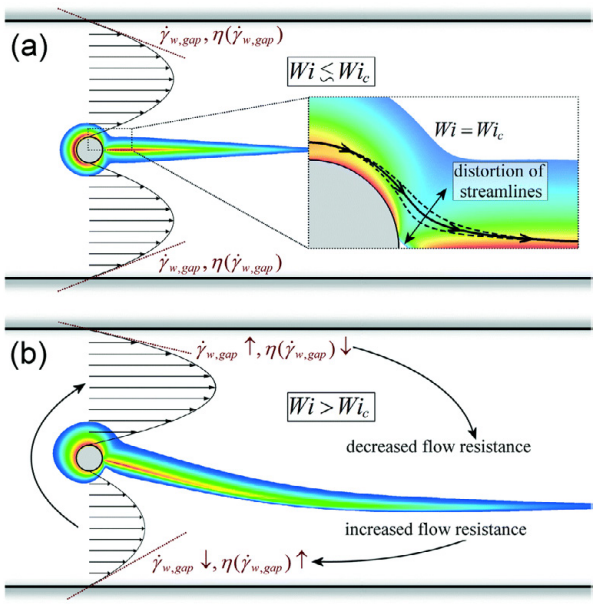

Figure 6.1. Schematic illustration of an asymmetric flow instability for a viscoelastic fluid around a pillar in a microchannel. The coloring represents elastic stresses where bluer is of lower magnitude and redder is of higher. Panel A shows a symmetric flow where Wi is below a critical Wi_c. The inset displays a disruption of the symmetric flow when $Wi = Wi_c$. Panel B shows an asymmetric flow where $Wi > Wi_c$. A feedback loop occurs that amplifies the asymmetry. Figure is reproduced from Ref. [133] with permission from the Royal Society of Chemistry.

6.4 Elastic Turbulence in Pillar Arrays

Unlike the flow around single pillars, pillar arrays constitute a large network of flow constrictions and expansions. The elastic properties of the flow may amplify the interaction between the local flows around neighbouring pillars. Local increases in polymer concentration, viscosity or flow velocity can affect the values of the same parameters of neighbouring areas. The change in flow in one area can change the flow in another, even far downstream and upstream in the array. Multiple flow asymmetries as presented in the previous subchapter can emerge and amplify each other. We believe this occurs in Papers III–V as a large-scale flow asymmetry in the form of oblique waves of higher concentration and aligned orientation of extended DNA strands are formed.

In Papers III–V, device-scale uniform elastic waves are presented. While no such waves have previously been observed, similar phenomena have been reported. One is the propagation of waves of regions of low flow velocity in hyaluronic acid solutions in a pillar array channel with slender pillars. The pillars in the device do not connect with the channel roof and similarly to Monami waves of inertial turbulence that propagate above canopies of vegetation, these waves propagate above the pillars [134]. Another phenomena is the propagation of flow velocity waves between two sides of a flow that has been split by a micro-pillar pair [124]. A third phenomena is the propagation of coherent flow structures composed of similar flow velocity surrounded by areas of lower flow velocity that arise downstream of 1D [135] and 2D pillar arrays [136]. The underlying mechanisms that give rise to those phenomena might be related to those presented in this work.

Polymer flow in porous media

The pillar arrays in our work constitute 2D models of porous media (a solid material containing a network of interconnecting pores). For over a century, people have been puzzled over why the flow resistance across porous media is increased when adding polymers to the solution. While the puzzle has not yet been completely solved, recent results provide clear evidence that elastic turbulence contributes to the increased flow resistance [137].

The following sections describe the effects of some of the most important parameters on elastic turbulence and on the flow dynamics that we observe in our devices

Effect of Sample Composition

Most work on elastic turbulence for both single pillars and pillar arrays has been based on fluids other than DNA solutions. These fluids include solutions of

aqueous wormlike micelles (WLM) [120, 122, 132, 133, 138, 139], high-weight polyacrylamide (pAAm) [112, 123], polyacrylamide in glycerol [121, 140], hydrolyzed polyacrylamide (HPAM) [125, 141], hyaluronic acid [134] and polyethylene oxide (PEO) in water [110, 111, 116] or in glycerol [118, 119, 142]. The wide variety of fluids used in the reported works makes the research findings difficult to compare as the number of relevant parameters that vary between the different fluids is vast. Some important examples of relevant parameters include polymer persistence length, mean polymer (or WLM structure) length, concentration, polydispersity, degree of segment interaction and buffer composition. While the formation of upstream vortices has been demonstrated for high-concentration DNA samples through flows across single constrictions [113-115] and micro bends [143], very little is known about flow of high-concentration DNA solutions in more complex geometries such as pillar arrays.

A few relevant DNA sample parameters that can affect the elastic flow include sample concentration, polymer length, ionic strength of the buffer and sample viscosity. By increasing the concentration or the polymer length and lowering the ionic strength, the concentration to overlap concentration ratio, C/C^* is higher, see subchapter 3.3 and Paper III where these two parameters were varied. A higher C/C^* leads to stronger molecule-molecule interactions which results in longer relaxation time, higher fluid viscosity and entanglement effects.

The solvent viscosity of the sample can also significantly alter the flow. By using a viscous solvent such as an aqueous glycerol or sucrose solution (as performed in Paper III), the shear thinning of a viscoelastic fluid can be disregarded and the fluid can be considered to have a viscosity independent of shear rate. This type of fluid is known as a "Boger fluid". By increasing the viscosity of the sample, the elasticity number, El, is raised both directly with the viscosity and indirectly with an increased polymer relaxation time. The increased viscosity thereby increases the relative impact to the elastic forces in two ways. As a consequence, elastic effects can be expected to be stronger and appear at lower flow velocity.

Note that if the DNA molecules are fluorescently labelled, as they are in this work, the staining ratio could also affect the flow as the molecules are extended by the addition of dye molecules (see subchapter 3.2).

Effect of Array Geometry

The geometry of a pillar array can be altered in a number of ways. Geometry parameters that could affect the flow include pillar radius, pillar shape, pillar gap (both parallel to and perpendicular to the flow), porosity (volume ratio of the open space or pores to the entire volume of the channel including the pillars), array width, array length, channel depth and the spatial distribution of the pillars. It is unclear how all of these parameters affect the flow and how changing one

parameter affects the impact of another. Figure 6.2 illustrates the different array geometries used in this thesis. In the following paragraphs, the effect of some of the most important geometry parameters are discussed.

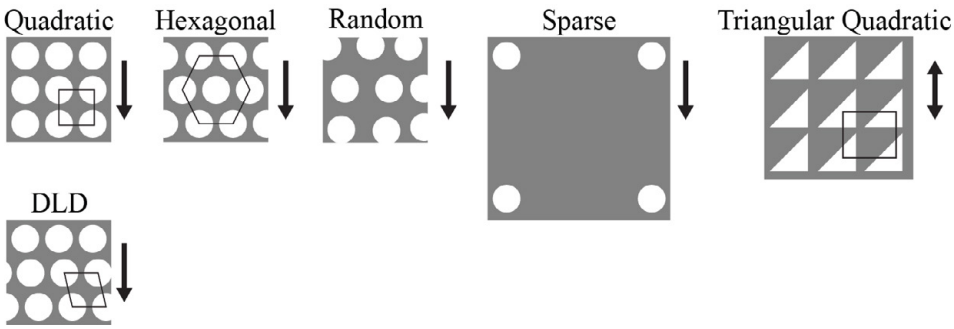

Figure 6.2. Schematics of the array geometries used in this work. The quadratic array is used in Papers III and IV, whereas the hexagonal random and sparse quadratic are used in Paper IV. The triangular quadratic array is used in Paper V and the DLD array is used in papers I and II. Note that the relative dimensions are not to scale. The arrows depict the average flow directions in each geometry.

The length scale of the array geometry can affect the elastic flow immensely as discussed earlier in the chapter. With the advent of microfabrication, pillar arrays have been able to shrink from the length scale of centimeters and meters (see *e.g.* work by Vossoughi in 1974 [144]) to micrometers. The smallness of the array dimensions and the curved flow lines can result in strong elastic effects. Note that most work on microfluidic pillar arrays has been conducted in arrays with relatively large dimensions (gaps approximately 20 μm to several hundred micrometers). This can be compared to our work with gaps of just a few micrometers.

The number of ways to spatially distribute pillars in a 2D pillar array is vast. Quadratic and hexagonal lattices are the simplest and most commonly investigated. The main difference between the two is that in hexagonal arrays, the pillar gaps have a 45° angle to the general pressure drop direction whereas in quadratic arrays the gaps are perpendicular and parallel to this direction. The result of this is that the stagnant zones of quadratic arrays are larger than those of hexagonal ones at the same porosity. The stagnant zone size difference could be a factor in creating the contrasting flow behavior for the two geometries as seen in Paper IV.

Kawale *et al.* found differences in the flow of hydrolysed polyacrylamide (HPAM) across both quadratic and hexagonal micropillar arrays, see Figure 6.3 [125]. In both array patterns, cycles of vortex growth and shedding were observed. These vortices originated upstream of the pillars, similar to those reported for single pillars. The stagnant zones where the vortices form were smaller and prism-shaped

in hexagonal arrays whereas in quadratic arrays, they were larger and conformed to the space in between the pillar in the flow direction. Their findings can be contrasted to the results in Paper IV where vortex formation was clearly visible for the quadratic array but not observed with the hexagonal array. The different behavior could be due to their array dimensions being an order of magnitude larger or that the sample composition is different.

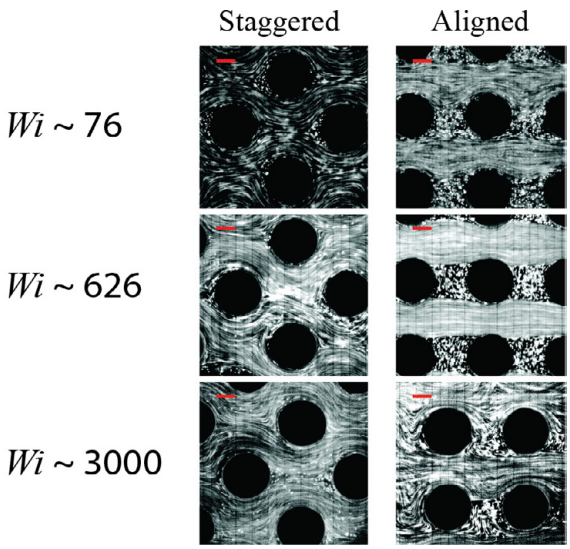

Figure 6.3. Viscoelastic flows of hydrolyzed polyacrylamide with different degrees of flow instabilities depending on Wi and the pillar array pattern. Staggered correspond the hexagonal and aligned to quadratic with the terminology used in this thesis. The flow direction is left to right. Scale bars are 100 μm. Reproduced from ref. [125] with permission from the Royal Society of Chemistry.

To better mimic common porous materials, disordered arrays may be preferred. There is an abundance of ways to create a disordered or randomized pillar array distribution. Note that each particular randomization may have a unique impact on the flow which could make the flows across different disordered arrays difficult to compare. The disordered array in Paper IV is based on a random shift in unit cell rows together with a slight shift in the position of each pillar in each unit cell. This design generates an array with local subarrays that are more or less similar of quadratic or hexagonal patterns. Other disordered pillar arrays that have been used to study elastic flows have relied on alternative randomization schemes. Interestingly, increased levels of pillar distribution disorder in these arrays have both been reported to delay [140] and advance [138] the onset of elastic turbulence with increasing Wi.

Effect of Pillar and Pore Shape

With the small dimensions of pillars and the gaps in between the pillars in the work of this thesis, the pillar shape could have a profound effect on the flow. In DLD studies, different pillar designs have shown to have a significant effect on the fluid dynamics around the pillars as well as resulting in a different critical diameter than their conventional cylindrical counterpart. These include triangular [145] air-foil [146] and I-shaped pillars [95].

When the flow geometry is symmetrical in both flow directions of the microchannel, such as the case for an array of symmetrical pores or a pillar array of circular cross-section, viscoelastic fluids exhibit identical flow patterns. However, when there is an asymmetry in the geometry, the flow can be significantly different for the two directions. The size of elastic vortices in stagnant zones have been shown to differ considerably at similar pressure drops across the channel. In addition, the resulting flow resistance have been shown to vary significantly depending on the flow direction for both triangular pore arrays [147-149] and triangular pillar arrays [150]. In Paper V, we show how both the microscopic and macroscopic flow patterns differ significantly in opposite flow directions through a pillar array with pillars of triangular cross-section.

7. Device Fabrication and Experimental Details

"Keep it simple"

The experimental motto I strive to follow but tend to forget

The experiments have been conducted in microfluidic devices which are designed and fabricated by us. To observe the positions and motion of DNA molecules inside these devices, an epifluorescence microscope has been utilized. The DNA samples have been stained with fluorescent labels and been flowed across the device channels using overpressure. This chapter describes these experimental procedures.

7.1 Device Fabrication

The devices used in this thesis were made in polydimethylsiloxane (PDMS) and glass. The PDMS devices have been fabricated using replica molding [151]. It is a powerful fabrication method that allows for rapid prototyping of devices (on the order of hours). PDMS, a commonly used material in microfluidics come also with a number of advantages. It is cheap (approximately $0.3 per device), biocompatible [152], optically transparent in the relevant wavelengths (240–1100 nm) and its surfaces are easy to chemically modify.

The molds have been made in two separate ways. In Papers I–IV, the molds have been made using UV lithography. It requires the purchasing of a mask which is both expensive and time consuming. As we recently had a maskless aligner (MLA150 maskless lithography system, Heidelberg Instruments GmbH, Heidelberg, Germany) installed in our cleanroom facility, the time from design to ready device has been reduced, from days, to hours. We utilized this new tool in Paper V.

This subchapter describes the fabrication steps for making the devices, from design to having a microfluidic device ready for use.

Device Design

When the purpose of a device has been decided, the first step in actually making it is to draw the design. We did this using a CAD-software, L-edit v.16.3 (Tanner Research, Monrovia, CA, USA). Some design rules were applied: sharp corners in channel connections were avoided to minimize flow disturbances. The width to height aspect ratio of channel designs was kept below 10:1. With larger aspect ratios than 10:1, there is a risk of PDMS channel roofs collapsing [153]. In order to achieve wide channels with large aspect ratios, we added supporting walls or pillars. The pillars must also not be of a height to width aspect ratio higher than 10:1, to reduce the risk of pillars breaking or sagging. A micro pillar array filter was also always added in the channel inlet and outlet regions to minimize dust particles in the system. Such particles can lead to clogging or a contamination of the channels.

Mold Fabrication – UV lithography

We fabricated the molds in two different ways. The first way is using UV lithography with a mask aligner. With this method, the design first had to be transferred onto a chromium photomask using a laser writer. The mask writing was outsourced to Delta Mask B.V. (Enschede, Netherlands). We made these molds in the negative photoresist SU-8. It is a chemically and physically robust material that can be used to produce high-aspect-ratio structures. We first fabricated the molds by spin-coating a thin layer of the material on silicon wafers. Then, we exposed the resist to UV-light using the pre-made photomask. The exposed areas of the resist was cross-linked by the light. The non-exposed parts could then be readily dissolved and washed away with a developer. Lastly, the manufactured molds were treated with an anti-sticking coating to make it possible to remove PDMS from the mold, to minimize fouling and make the mold last longer. See the full UV lithography protocol in Appendix 1.1. The generic steps to make a device this way can be seen in steps 1–6 in Figure 7.1.

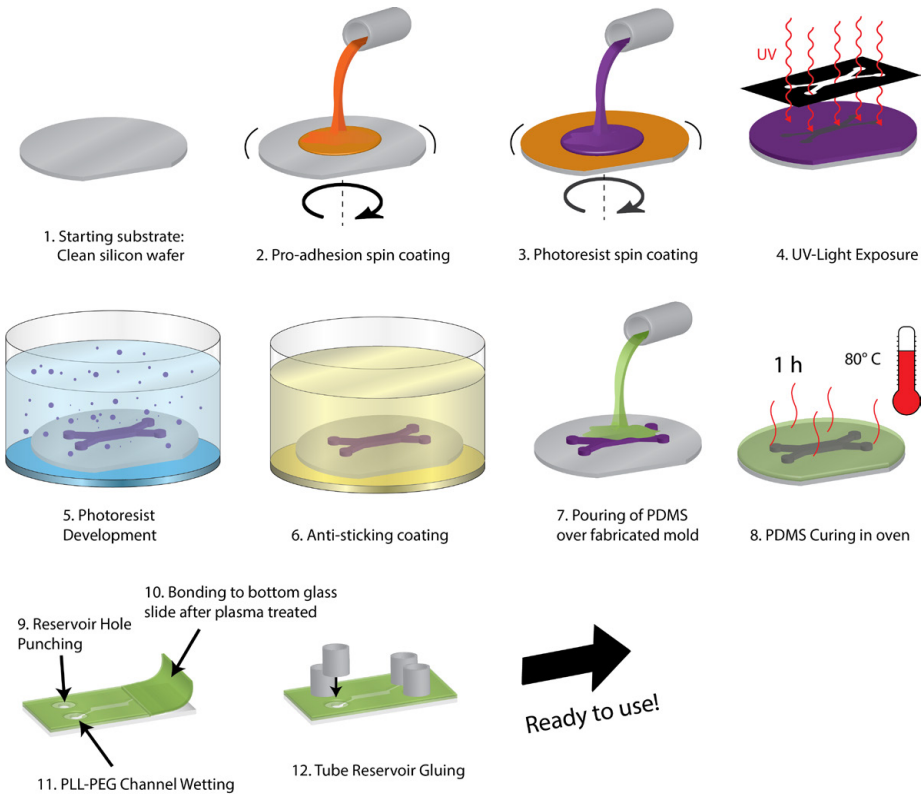

Figure 7.1. Generic steps for fabricating a microfluidic device with replica molding and UV lithography. Note that steps 2, 11 and 12 are optional. Figure reproduced from [18] with permission.

Mold Fabrication – Maskless Photolithography

The second way we fabricated the molds was with a maskless aligner. It writes directly onto the photoresist (mrDWL40 resist, Micro Resist Technology GmbH, Berlin, Germany) which allows for a total fabrication time between tens of minutes to many hours depending on the size and complexity of the design. It has a higher writing resolution than the mask aligner used with minimal feature sizes down to 600 nm (compared to approximately 1.5 µm for the mask aligner). The mold fabrication steps are very similar to the steps with the mask-aligner. It starts with spin-coating the photoresist onto a silicon wafer. The device design is then written directly onto the photoresist with a laser. The exposed photoresist is then cross-linked and the parts that were not exposed are washed away in a development step. The anti-sticking layer was then applied using atomic layer deposition (ALD). ALD allows for a fast and highly controlled deposition. See the detailed fabrication protocol in Appendix 1.2.

Replica Molding

Replica molding works by creating a rubber replica from a mold [153]. Liquid PDMS is first poured onto the mold and then becomes cured by thermal baking. Access holes are then punched and the PDMS channels are sealed to a glass substrate using plasma-bonding. In some devices, silicone reservoirs were glued onto the access holes to be used as connectors for the tubes containing nitrogen gas. Other devices instead lacked any extra reservoir to minimize the strong auto-fluorescence coming from the silicone tubing and the glue used to attach the tubing. These devices were made thicker and connecting tubes were directly inserted into the access holes. Note however, that the devices with glued tubes with them still work well with limited fluorescence contamination if the tubes are placed far away from the region of interest in the device design. See steps 7–12 in Figure 7.1 for an illustration of the process and a detailed replica molding protocol in Appendix 1.4.

Surface Modifications

The use of native hydrophobic PDMS surfaces in microfluidics leads to biofouling of proteins and dye molecules. The high hydrophobicity of PDMS surfaces leads to a high level of hydrophobic interaction between them and the biomolecules. In order to minimize the surface fouling, a multitude of surface passivation schemes have been developed and applied for PDMS, see [154, 155]. A commonly used molecule for surface passivation is the triblock polymer, poly(ethylene oxide)–poly(propylene oxide)–poly(ethylene oxide) (PEO–PPO–PEO, trademark Pluronic®). Its hydrophobic PPO-group spontaneously adsorbs to a hydrophobic surface. The PEO [also known as poly(ethylene glycol) or PEG if short] groups are in contact with the aqueous fluid in the channel and prevent other molecules from sticking to the channel walls. When many of these molecules adsorb next to each other, they form an anti-biofouling carpet or polymer brush. Several studies have shown substantial (95% [156] and 85% [157]) decrease in protein adsorption using the PEO-PPO-PEO coating compared to untreated control surfaces.

The PEO–PPO–PEO surface passivation scheme has been used in Papers I and III. In Paper II, the scheme was not used as it interfered with another surface treatment (see below). It was not used in Papers IV and V due to an effort to simplify the experiments by minimizing the number of substances in the sample.

When fabricating the devices, the plasma-oxidation step, used for sealing the PDMS channels to glass, renders the surfaces hydrophilic. It takes at a minimum one day for the PDMS to fully re-gain its hydrophobicity [158], but in our experience, usually longer. To speed up the hydrophobic recovery and make the surface conditions more reproducible, we thermally aged the plasma-treated PDMS for a day at 120 °C as described by Hung and Lee [159].

It is possible that the addition of PEO–PPO–PEO affects the flow dynamics of the DNA solutions. However, the molecular weight is much smaller (0.012 MDa for Pluronic® F-127, approximately 2500 × less than for λ DNA) and the concentration (~10 µg/mL) is much lower than for the high-concentration DNA solutions so we expect minimal effects on the flow dynamics or DNA behavior.

A surface coating protocol for DNA hydrophobic surface stretching or molecular combing have also been developed (see appendix 1.3). In contrast with the other coating, this coating is designed to make DNA stick to the surface. The choice of substrate used for DNA surface stretching has major importance. The cyclic olefin polymer ZEONEX® has proven to be superior to other substrates [74]. It is chemically stable, optically transparent and with minimum auto-fluorescence (see the datasheet of the manufacturer). It has been shown to yield a reproducible and high DNA deposition efficiency and exceptionally long-DNA extension (170%, the same relative extension as for S-DNA, see subchapter 4.4) [74]. In order to only coat the area of interest, the stretching channel, we performed selective plasma etching. For this, a PDMS slab was used as a negative plasma-mask. This selective plasma etching technique was developed by Jason P. Beech at Lund University.

7.2 DNA Samples

We have worked almost exclusively with purified DNA samples. They include a DNA ladder (0.25–10 kbp, GeneRuler 1 kb DNA Ladder, Thermo Fisher Scientific), 1 kbp, 5 kbp, 10 kbp and 20 kbp (NoLimits, 500 µg/mL, Thermo Fischer Scientific, Waltham, MA, USA), bacteriophage lambda DNA (λ DNA, 48.5 kbp, New England Bio-labs, Ipswich, MA, USA) and bacteriophage T4 (T4GT7, 165.6 kbp, Nippon Gene, Tokyo, Japan). In order to minimize photobleaching and photodamage, 3% (v/v) β-mercaptoethanol was added to the DNA sample except for where the photobleaching was expected to be minimal due to high flow rates. As BME increases the ionic strength, it was also excluded when the salt concentration was kept low.

Bare DNA molecules cannot be seen directly with optical microscopy using visible light. To overcome this obstacle, different fluorescent dyes have been developed in order to indirectly visualize single DNA molecules. The samples in this thesis have been labelled with fluorescent cyanine dyes (mainly YOYO-1, 491ex./509em. and YOYO-3, 612ex./631em., Life Technologies, Carlsbad, CA, USA). For detailed instructions on proper storage, handling and staining with these dyes, see the manufacturer's datasheet [160] and the work by Rye *et al.* [161]. An important note is that the staining will be more homogenous if taken place at high ionic strength [29, 161]. The staining in this work was therefore conducted at

5 × Tris EDTA (TE) for most measurements and at 1 × TE for the low-ionic strength measurements.

The basis of the dye visibility is fluorescence. The fluorescence works by these dye molecules first absorbing light of a certain wavelength. The absorbed photon excites one of the electrons of the molecule into an excited energy state. Soon thereafter, the excited electron first relaxes vibrationally and then emits light when relaxed back to the ground state. Figure 7.2B displays the absorption and emission spectra of YOYO-1. The energetic shift between the emission and the excitation is called Stokes shift. We can exploit this energy shift and only image the emitted light by adding appropriate filters.

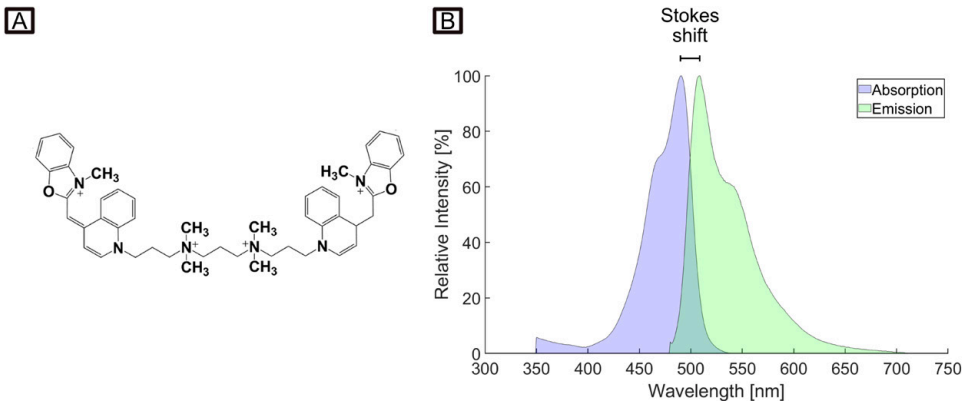

Figure 7.2. Overview of cyanine DNA dyes. Panel A shows the chemical structure of YOYO-1. Panel B shows the absorption (blue) and emission (green) spectra for YOYO-1. The plot was generated with data available by ThermoFisher Scientific [162].

The cyanine dye molecules are positively charged and easily bind to the negatively charged DNA. They intercalate to the DNA with one or two ends. Figure 7.2A shows the chemical structure of YOYO-1 which has two positively charged ends. These dyes are virtually invisible when freely dissolved in the solution due to losing their absorbed energy non-radiatively via rotation. However, upon binding to DNA, they exhibit a large enhancement of the fluorescence intensity. YOYO-1 is especially extraordinary. Rye *et al.* measured a 3200 times increase in fluorescence intensity upon binding to DNA compared to free YOYO-1 in the same buffer at peak emission wavelength [161]. In addition, YOYO-1 has a high quantum yield (0.52 [160]) and is chemically stable when bound to DNA. When two DNA samples had to be visualized independently, a dual-color scheme was used with one sample stained with YOYO-1 and the other with YOYO-3. Note however that the quantum yield of YOYO-3 is only 0.15, compared to 0.52 for YOYO-1. It is therefore more difficult to use YOYO-3 for single molecule

fluorescence microscopy as the signal is much weaker. See the generic staining protocol in appendix 1.6.

7.3 Running the Experiments

Microfluidic Devices

The first step in running a device is wetting the channels. For hydrophilic channels, the liquid enters easily. However, with the hydrophobic channels in this work, a high pressure (1 bar) had to be applied for several minutes to ensure that the micrometer-sized gaps were wetted to allow the sample to flow smoothly across the device with the lack of flow-disrupting air bubbles. During the wetting, a buffer containing the triblock copolymer Pluronic® F-127 (Sigma-Aldrich) is injected. The triblock polymer coats the channels to prevent bio-fouling as described in subchapter 7.1. Note that for Papers IV and V, the samples were directly injected into the channels without the wetting step or anti-fouling agents. These steps were excluded to simplify the experimental process. As only one outlet existed, wetting directly with the sample would not contaminate other outlets used for *e.g.* long-DNA collection. While clogging was not observed without the anti-fouling agents in this case, it is difficult to draw conclusions on the surface-effects of DNA solutions for with and without anti-fouling agents.

All chemicals that are injected into the device have been filtered with a 200 nm filter to minimize the contamination of particles that might otherwise block or interrupt the flow.

The flow was generated using a pressure difference across the channels. Nitrogen gas overpressure was applied to the inlets while keeping the outlets at ambient pressure. The pressure was controlled using a MFCS-4C pressure controller (Fluigent, Paris, France) or with a custom-built setup with the pressure measured using a manometer (model 840081, Sper Scientific, Scottsdale, AZ, USA). For Paper II, flow was also generated with negative pressure through a vacuum pump (mini diaphragm vacuum pump, VP 86, VWR), see Appendix 4. The flow rate was measured using a flow sensor (Flow rate platform (FRP) with flow unit S, Fluigent, Paris, France). The flow sensor was connected to the outlet of the devices with tubing filled with ultra-purified water. Note that the tubing length was long enough to ensure that the sample never reached the sensor as the sensor was only calibrated to work with pure water.

The pressure levels were controlled by the software OxyGEN (v. 1.1.0.0, 2021, Fluigent, Paris, France) or a custom-built LabVIEW VI (v. 2018, 32-bit, National

Instruments, Austin, TX, USA) for Papers I and II. The front panel of the LabVIEW VI is shown in Figure 7.3.

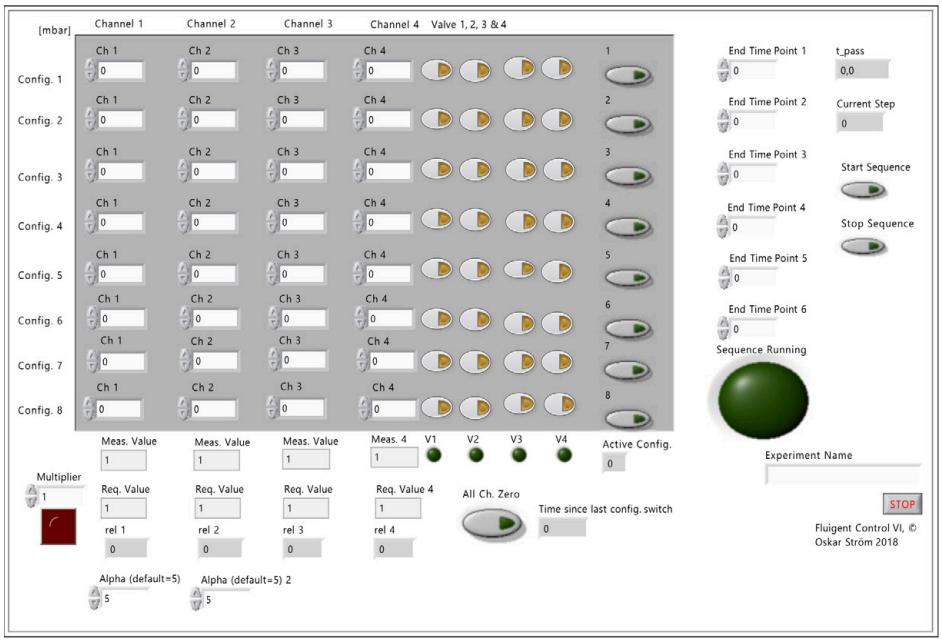

Figure 7.3. Front Panel of the LabVIEW VI for controlling the pressure applied to the microfluidic system. The left panel shows 8 pressure configurations for four pressure channels and four solenoid valves. Any pressure value can be inserted into the pressure channel control whereas the valves can only be turned on or off. Just below, the measured and requested values for the four channels are visible. Below the valves are light indicators of the valve on/off status. The configurations can be run in a sequence. The durations at each step is controlled by the input boxes at the right side. The passed time and the current step are displayed while running the sequence.

Single Molecule Epifluorescence Microscopy

To image the sample flowing in the device, an epifluorescence microscope was used. It works by exciting the sample with filtered light from a light source (Lumencor SOLA 6-LCR-SB light engineTM, Lumencor Inc, Beaverton, OR, USA or Solis-470C High-Power LED, Thorlabs, Newton, NJ, USA). The subsequent light, emitted by the fluorescent molecules, is also filtered, and ultimately detected by a camera sensor. In order to detect single DNA molecules, we utilized an ultra-sensitive electron multiplying charged coupled device (EMCCD) camera (Andor Ixon 897-DU, Andor Technology, Belfast, Northern Ireland). By multiplying the signal 300 times (EM gain), an EMCCD camera overcomes the otherwise commonly high readout noise in normal CCD cameras. It makes it possible to record ultra-low fluorescence signals at high framerate. For high-concentration samples, we used a scientific CMOS camera (ORCA-Flash4.0

V3, Hamamatsu, Hamamatsu, Japan) which has a much larger field of view than the EMCDD camera. A generic experimental setup is visible in Figure 7.4.

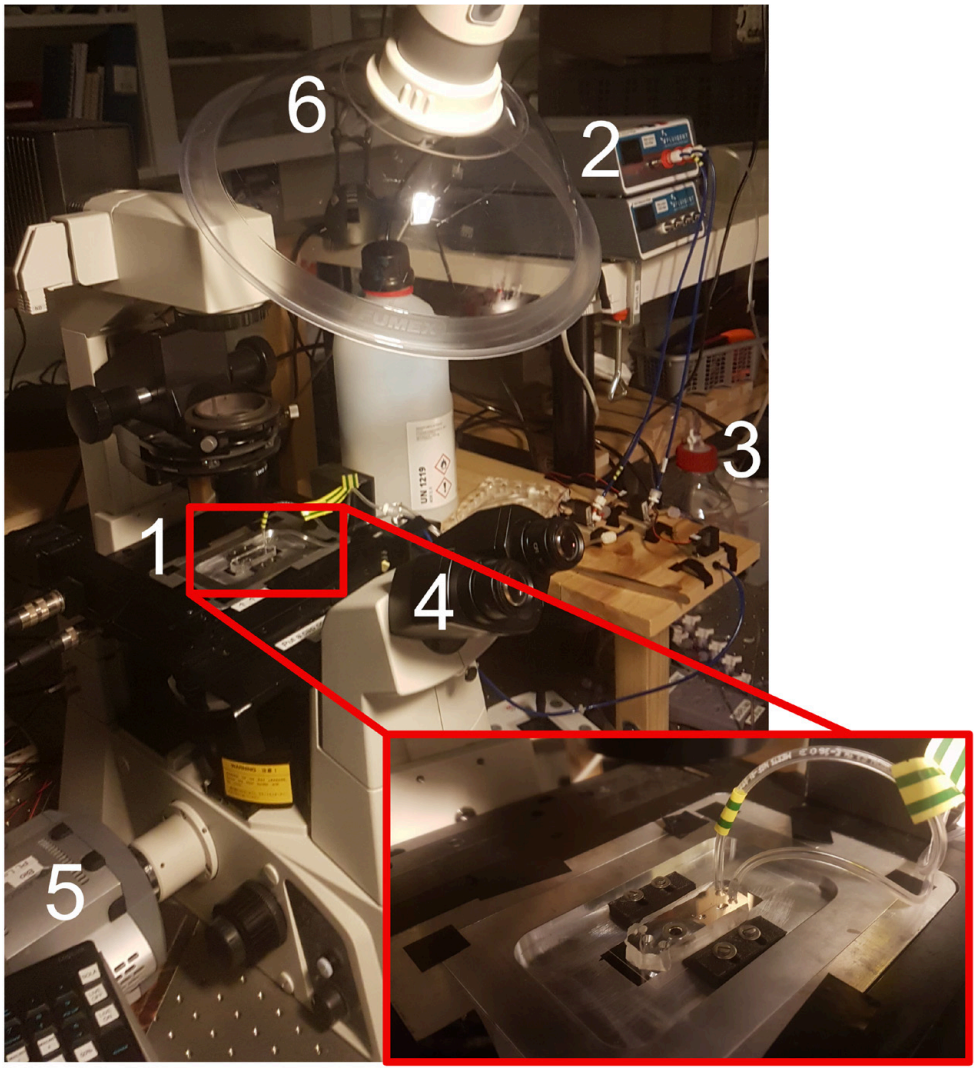

Figure 7.4. Generic experimental setup. (1) A device is mounted on a custom-made aluminum holder with 3D-printed clamps in acrylonitrile butadiene styrene (ABS) plastic. Pressurized nitrogen gas is connected to the (2) pressure controller (MFCS-4C, Fluigent, Paris, France) which generates the flow in the device. (4) An epifluorescence microscope (Nikon Eclipse-TI model TI-DH, Nikon Corporation, Tokyo, Japan) is used together with (5) an EMCCD camera (Andor Ixon 897-DU, Andor Technology, Belfast, Northern Ireland). (6) The extraction hood is used to prevent exposure to hazardous β-mercaptoethanol fumes. Out of image is the light source (Lumencor SOLA 6-LCR-SB light engineTM, Lumencor Inc, Beaverton, OR, USA).

Dual-channel Color/Polarization setup

For Papers I, III and IV, a dual-polarization setup was utilized. A beam splitter (OptoSplit II, Cairn Research Ltd., Faversham, UK) was installed after the emission filter and before the camera. Two modes were used, dual-polarization and dual color. For the polarization mode, two perpendicular polarization channels were set-up so that they were at a 45° to the long axis of the microchannels. Note that a smaller camera sensor pixel size is preferred with the dual polarization mode. A larger pixel size makes it harder to align the two channels. See Figure 7.5 for a photograph and a schematics of the beam splitter.

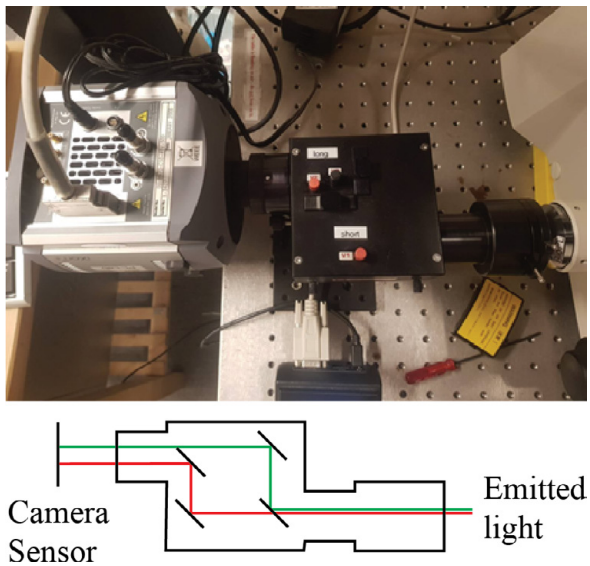

Figure 7.5. Photo (top) and schematics (bottom) of the beam splitter. The emitted light is split into two colors or two polarizations depending on the filters used.

8. Conclusions

This work has presented a series of microfluidic devices and experimental results for long-DNA preparation and transport.

While sequencing has revolutionized access to genomic data, sample preparation for sequencing has lagged behind. It is generally slow, laborious, requires expensive instruments and comes with great sample losses. While microfluidic techniques have shown great promises to improve sample preparation, they usually fall short on throughput.

Papers I and II have been focused on the development of sample preparation devices. Paper I has shown a large improvement in the throughput of long-DNA separation while Paper II presents device integration of long-DNA separation with an on-chip analysis technique. The developed devices are simple to fabricate and easy to run. The material choice makes the devices very cheap (approximately $0.3 per device). The device smallness makes them both portable and functional with miniscule sample volumes. DNA samples are commonly small and often require amplification, a process step that can be avoided with our devices.

Papers I, III–V concern the transport of high-concentration, long-DNA samples across micropillar arrays. While low-concentration transport of long DNA in microfluidics is a widely studied area, there is very little work regarding high-concentration DNA flow dynamics. Working at high concentrations can not only enable processing at higher throughput but also involves interesting and complex elastic effects. Studying and understanding the effects might lead to unforeseen and potentially impactful new applications.

We have shown that concentration effects can lead to both improved and worsened DNA separation. Papers III–V describe novel elastic flow phenomena, short and long-range cyclic patterns, and in particular, waves. The emergence and behavior of these waves have been characterized with different sample parameters and in different pillar array geometries. It is possible that these phenomena could be useful for microfluidic sample mixing or in fluidic diodes.

In the following subchapters, conclusions based on each paper are presented.

8.1 Paper I: High-throughput Separation of Long DNA in Deterministic Lateral Displacement Arrays

This paper focuses solely on the bottleneck of long-DNA sample preparation which is slow and laborious. There have been a number of micropillar-based microfluidic techniques that show great promises of long-DNA separation and isolation. However, they all suffer from low throughput.

In this paper, we demonstrate displacement and separation of several long-DNA samples using a microscale deterministic lateral displacement (DLD) array at high flow velocity. We show that we can separate 166 kbp long DNA from 48.5 kbp long DNA at an unprecedented flow velocity of approximately 34 mm/s, see Figure 8.1. The volumetric and mass throughput is increased approximately four orders of magnitude compared to previous long-DNA separation in DLD and one order of magnitude higher than the highest reported numbers for long-DNA separation in microfluidics. The presented throughput is high enough to produce sufficient sample quantities for standard analysis techniques in a short amount of time.

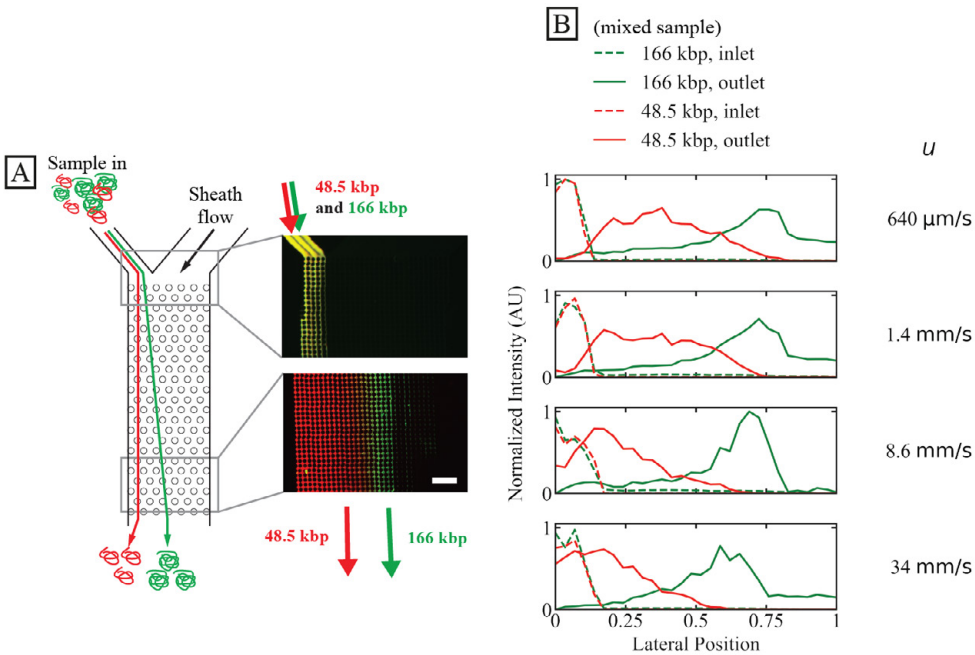

Figure 8.1. High-throughput separation of 166 kbp and 48.5 kbp DNA samples. (**A**) Schematic of the separation with fluorescent images of the array inlet and outlet. Dual staining have been used where 48.5 kbp is stained with YOYO-1 (red) and 166 kbp is stained with YOYO-3 (green). (**B**) Lateral distributions of the array inlet and outlet for different flow velocities. The scale bar is 100 µm. At a flow velocity of 34 mm/s, the sample inlet flow rate was 24 µL/h and the DNA mass throughput was 760 ng/h. Figure is reproduced from [93] (no permission required).

The separation is performed in standard soft lithography fabricated, micrometer-sized devices, without the need for complicated nanofabrication or parallelization. It makes the technique simple and comparatively cheap.

We demonstrate that higher DNA concentrations can both enhance and worsen the separation. Elastic effects arise that seem to enhance the displacement at high flow velocity for certain DNA concentrations. However, high DNA concentration is also shown to be deleterious to the separation and lead to DNA stream instabilities.

We believe that high flow velocity DNA displacement is possible due to the optimization of various device and sample parameters compared to previous work with DNA separation in microscale DLD devices. We show that we can displace long DNA at high flow velocity with a device with periodicity, N of 50 while not with a device with N of 20. This difference could increase the effect of a number of possible mechanisms that enhance displacement, including conformational changes, rotation and lift forces.

We show that DNA separation is possible, even when the molecules are extended, as shown in examples of DNA strands at different flow velocities in Figure 8.2. Displacing long DNA in microscale devices have previously been shown only to be possible when the flow velocity was low enough to keep the molecules in a coiled conformation so that their short axis were larger than the critical size of the array. In fact, all results have a Deborah number higher than unity which implies that molecules are at least extended some of the time in the device.

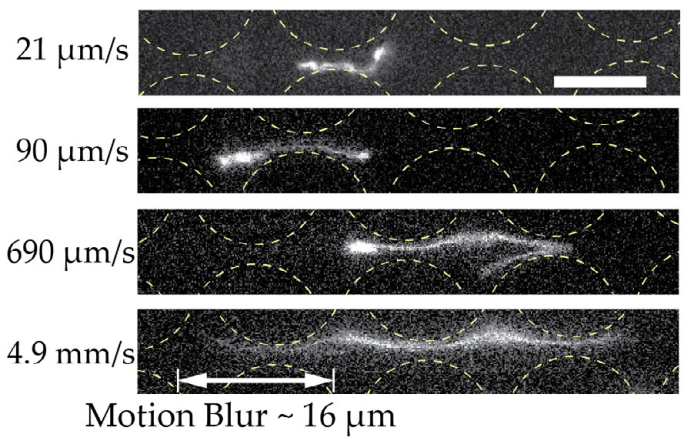

Figure 8.2. DNA strand extension as a function of flow rate. Typical examples of 166 kbp DNA for each flow velocity. Scale bar is 10 μm. Figure is reproduced from [93] (no permission required).

8.2 Paper II: Long DNA Isolation and Imaging using Lateral Displacement Arrays Integrated with DNA combing

While it is possible to use deterministic lateral displacement (DLD) on its own and analyse the separated species off-chip, the transfer step may result in sample losses, and sample damages. It is possible that the high shear rates used in paper I would fragment megabase pair-long DNA.

In this paper, we demonstrate integration of long-DNA isolation using DLD with a DNA analysis technique, on-chip molecular combing, see Figure 8.3. We perform the sorting and combing of long DNA from a background of shorter DNA in less than 10 minutes, much faster than conventional gel-based techniques of long-DNA isolation and analysis. By integrating the analysis on-chip directly after the isolation, very low flow velocity is needed which could make it possible to work with DNA samples that are more sensitive to shear forces. The sample losses are also minimal which makes it possible to work with samples that are of very small volumes or consist of an ultra-low DNA concentration. A few hundred sorted and stretched molecules are enough for the optical mapping analysis on the combed DNA. It eliminates the need for increasing the amount of sample by cell culturing or DNA amplification steps which is usually needed for manipulation and analysis of DNA samples.

The current device design is a proof-of-principle with DNA of 166 kbp long strands. While the separation step worked well, the subsequent stretching step was suboptimal. The surface roughness of the stretching channel was too high, leading to irregular meniscus migration. In addition, the channel was too deep to capture a large fraction of the molecules. This resulted in only a sub-fraction of the molecules binding to the surface. An updated design would therefore include a stretching channel that has smoother surface walls and a channel depth that is reduced an order of magnitude.

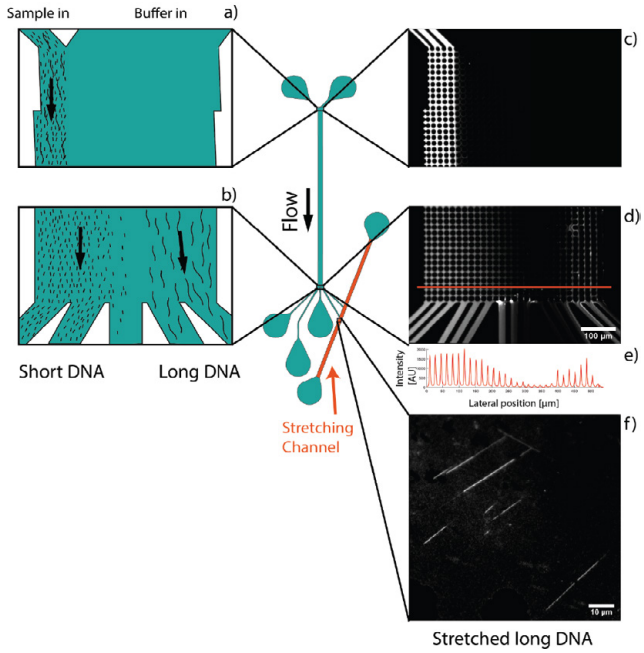

Figure 8.3. Integration of DNA separation with Deterministic Lateral Displacement (DLD) and surface stretching with molecular combing. Long DNA (166 kbp) is displaced laterally and isolated from short DNA (0.25 kbp to 10 kbp). (a) and (b) are schematic whereas (c) and (d) are fluorescent micrographs averaged over a duration of 1 min. (e) Fluorescent intensity across red line in (d). After isolation, the long DNA molecules are stretched out on the surface as shown with a fluorescent micrograph in (f). Figure is reproduced from [163] with permission from the authors.

8.3 Paper III: Short and Long-range Cyclic Patterns in Flows of DNA Solutions in Microfluidic Obstacle Arrays

The third paper builds on the high-concentration experiments of paper I. When injecting high-concentration, long-DNA samples into a micropillar array of a quadratic lattice at high flow velocity, we discovered the emergence of ordered and regular waves at the device-scale. The peaks of these waves consist of local regions of higher concentration and higher degrees of extension together with specific orientations of the extended molecules. See Figure 8.4(b) for a low magnification fluorescent micrograph of the waves.

When we change the geometry of the micropillar array from quadratic to disordered, we eliminate the long-range flow patterns, see Figure 8.4(c). Eliminating the waves could be useful if they prove detrimental to any application. It is possible that a slight randomization could keep the function of the application at hand, *e.g.* DNA separation, while being able to avoid detrimental waves.

We have identified vortex pairs forming between the pillars in the flow direction. These vortices periodically collect DNA and grow in intensity and apparent size until they shed a blob of DNA. We believe that the instability and shedding of these vortices are closely related to the emergence of the waves. See Figure 8.5 for a time series and kymograph of a vortex growth and shedding cycle.

We studied the wave dynamics as a function of flow rate, buffer composition (ionic strength and solvent viscosity), concentration and molecular length. We find that the waves only occur at high concentration to overlap concentration ratios, *C/C**, or at higher solvent viscosity.

By using a micropillar array with very small spatial dimensions (a few micrometers) and very small radii of the resulting curved streamlines, the elastic forces in the device are enormous ($El \propto l_0^{-2}$, see chapter 6). Previous works have generally been concerned with pillar arrays of larger dimensions and with samples other than DNA solutions. Our small sized-pillars together with using DNA as a sample could be major reasons why these waves arise in our system.

The waves presented in this paper can be useful for *e.g.* enhanced mixing or be destructive for sorting schemes like DLD that rely on laminar flow. Our characterization of elastic phenomena in microarrays advances the development of high-throughput handling of complex fluids, something that has long been seen as a severe limitation in microfluidics.

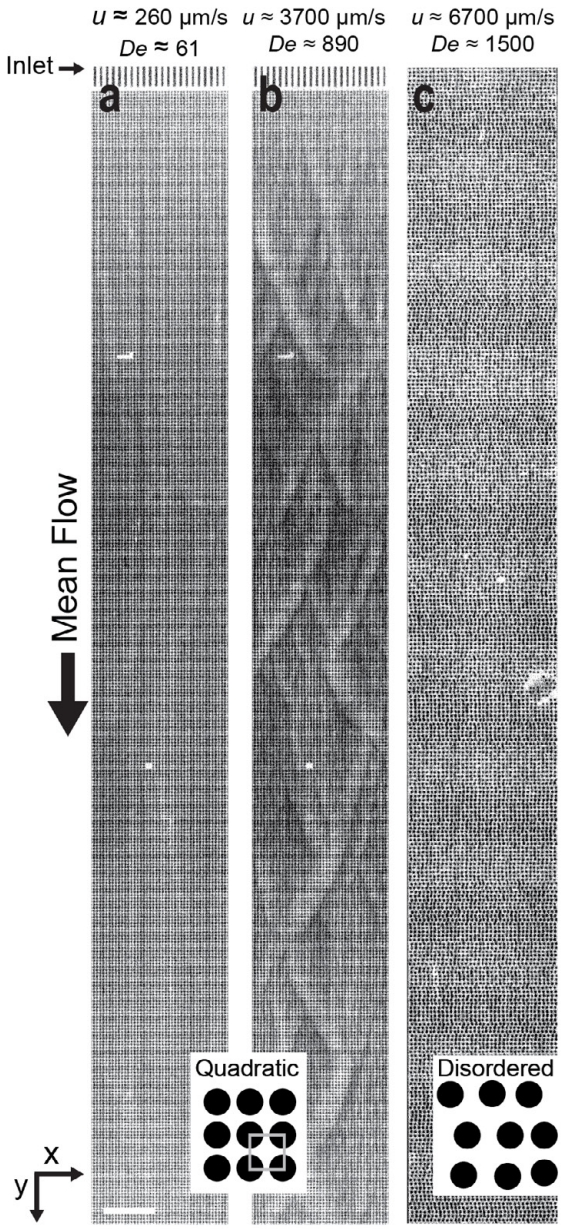

Figure 8.4. Macro-scale flow dynamics comparing the fluorescent micrographs of the flow of a 400 μg/mL λ DNA solution across a quadratic array at low and high flow velocity, (a) and (b), respectively, with that of a disordered array (c). The scale bar is 300 μm. Reproduced from [164] with permission from the authors.

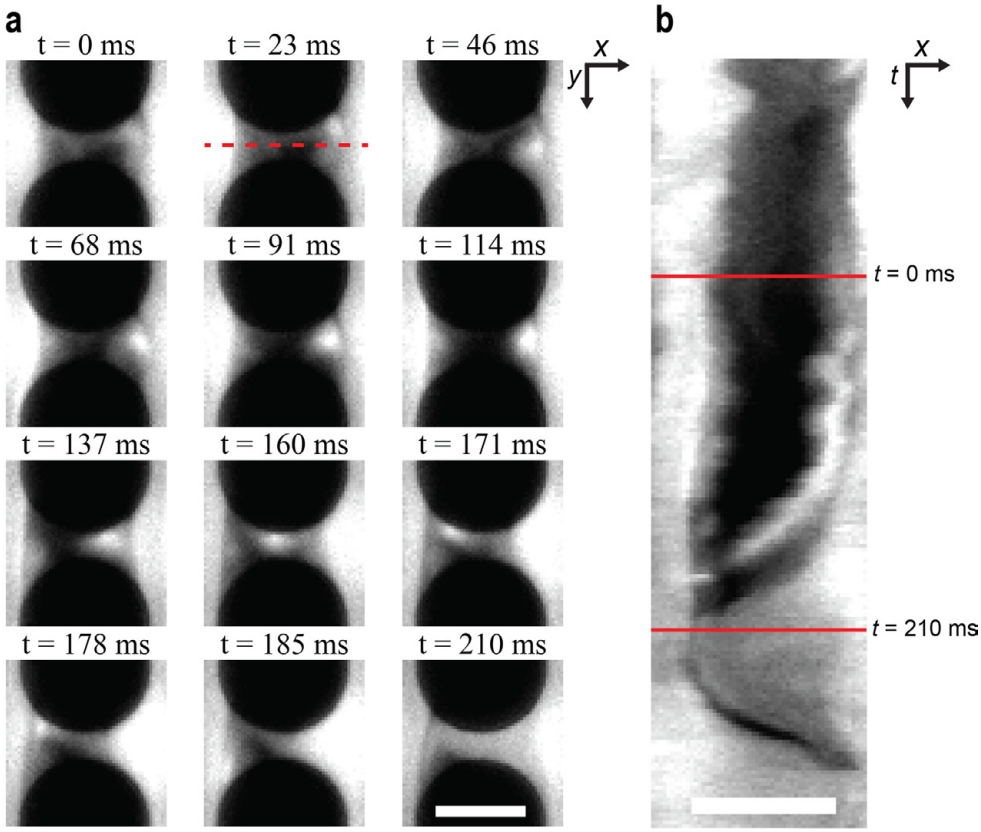

Figure 8.5. Vortex grown and shedding of a DNA blob inside the micropillar array. (a) shows a time series of the event while (b) shows a kymograph of it. Scale bars are 10 μm. Reproduced from [164] with permission from the authors.

8.4 Paper IV: Geometry-dependent Elastic Flow Dynamics

The fourth paper builds on Paper III. It concentrates on the effect of pillar array distribution on the flow dynamics of high-concentration λ DNA solutions. It compares the flow of the previously presented quadratic and disordered arrays with hexagonal and sparse pillar-array distributions.

In the hexagonal array, large chaotic zig-zag flow patterns emerge at similar flow velocity as when waves appear in the quadratic array. At a microscopic scale, the flows, observed using polarization microscopy, look remarkably similar for the quadratic and hexagonal arrays, where the direction of the flow is continuously

switching such that it is angled either to the left or the right, see Figure 8.6. In both cases, the DNA strands bundle up as diagonal streaks.

As shown in Paper III, the disordered array exhibits no large-scale flow patterns like those of the quadratic and hexagonal array. However, in this paper we show that the local flow patterns are very interesting with high variation in the flow stability. The flow in some of the gaps between the pillars in the flow direction is stable and show very little variance in the DNA concentration while others are unstable with a great degree of switching in the flow direction.

Fourier analysis and analysis of the fluctuations reveal large differences between the dense array geometries.

The array of sparsely distributed pillars exhibit no waves or coupling between flow instabilities around the pillars laterally. However, periodic cycles of vortex growth and shedding are still observable as can be seen in Figure 8.6(B–D). The shedding events affect downstream flow instabilities and causes a cascade of shedding.

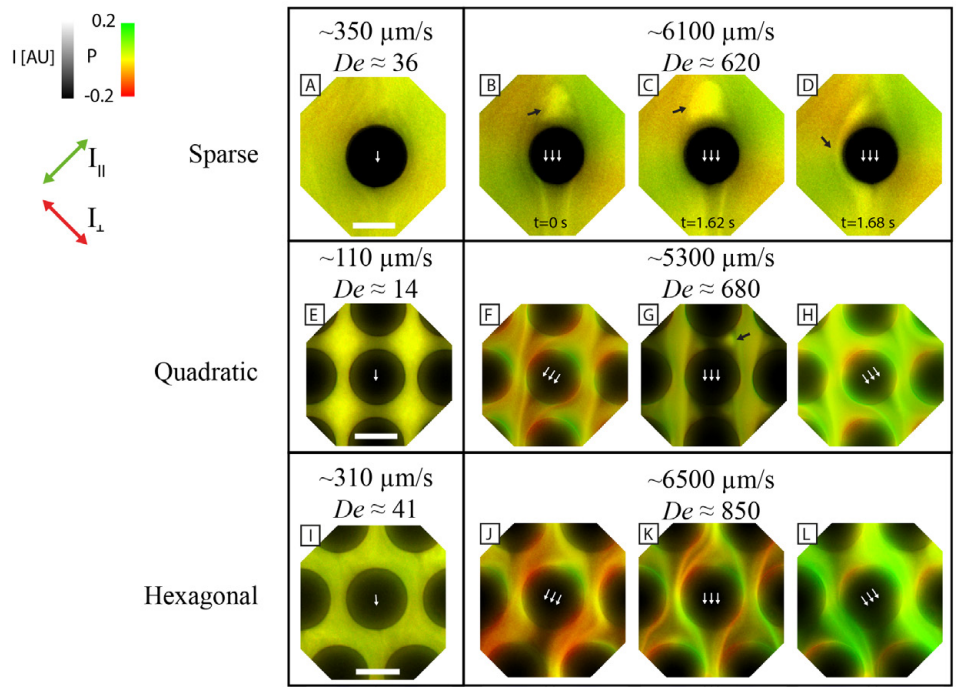

Figure 8.6. Micro-scale high-concentration DNA flow dynamics as a function of pillar-array geometry. The images are colored using the Hue-Value and Saturation (HSV) model. The pixel value of the images corresponds to the fluorescence intensity of the micrographs whereas the hue corresponds to the polarization emission ratio. At low flow velocity (**A**), (**E**) and (**I**), the flow is relatively stable and homogenous with minimal polarization differences across the image. In a sparse array at high flow velocity (**B**)–(**D**) Vortex growth and shedding in the sparse array. (**F**) and (**H**), switching of the flow between right and left in the quadratic array, corresponding to waves. (**G**) DNA blob visible in a vortex between waves. (**J**)–(**L**) Similar switching of the flow in the hexagonal. Note the difference between the waves (**K**). Scale bars are 10 µm.

As found with the quadratic array in Paper III, periodic cycles of growth and shedding are visible in some of the pillar gaps in the disordered array as well as upstream of the pillars in the sparsely distributed array. Interestingly, others have observed similar cycles with other viscoelastic fluids [118, 125]. This means that potentially waves of other materials could be generated as well.

By altering the pillar array geometry, we can induce or avoid large-scale flow patterns such as ordered waves or chaotic zig-zag patterns. This finding can help in understanding the underlying flow mechanisms that lead to waves. It can also aid in improving the design of microfluidic tools that either have their functionality enhanced or worsened by the elastic phenomena.

8.5 Paper V: Broken Symmetries in Microfluidic Pillar Arrays are Reflected in a Flowing DNA Solution across Multiple Length Scales

By changing the lateral symmetry of the circular pillars by exchanging them by triangular pillars, the symmetry of the large-scale wave pattern is broken. Instead of observing device-scale waves migrating with two separate orientations, the large waves only appear in one orientation, see Figure 8.7. Changing the direction of the flow by applying pressure on the other end of the array results in waves of another orientation.

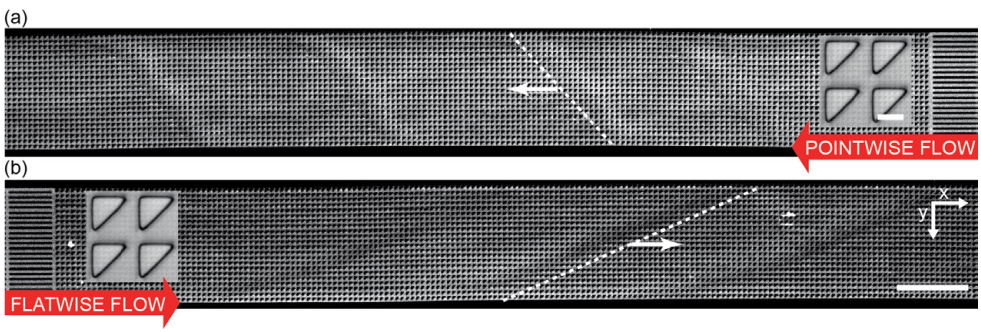

Figure 8.7. Wave orientation differs with flow direction. When the flow is changed from pointwise to flatwise, the wave angle changes. Scale bars are 10 µm (inset) and 500 µm (large micrograph).

The microscopic flow dynamics is also different for the two flow directions, see Figure 8.8. At very low flow velocity, the DNA concentration is spatially homogenous across the array, similar to how Newtonian fluids would appear. At slightly higher flow velocity, DNA depletion in the gaps in the flow direction

takes form. This is similar for both flow directions. At even higher flow velocity, asymmetric vortex pairs are visible. The vortices that form in the flatwise flow are much more stable and pronounced that those that form in the pointwise flow.

The waves appear earlier for the pointwise flow than for flatwise. We also see a difference in the flow rate for a given applied pressure difference when the waves appear. This implies that the system is a fluidic diode at certain flow velocities. However, more systematic and careful measurements of a potential diodicity are needed to ensure that the difference in flow rate is not due to artifacts of the system.

The altered wave phenomena in triangular arrays could aid in understanding the emergence of the waves. Long-range waves of two orientations are hindered. Controlling the direction of the waves might make them less destructive for separations, compared to waves that are move in two directions. Further experimental and numerical studies are needed to fully understand the underlying mechanisms.

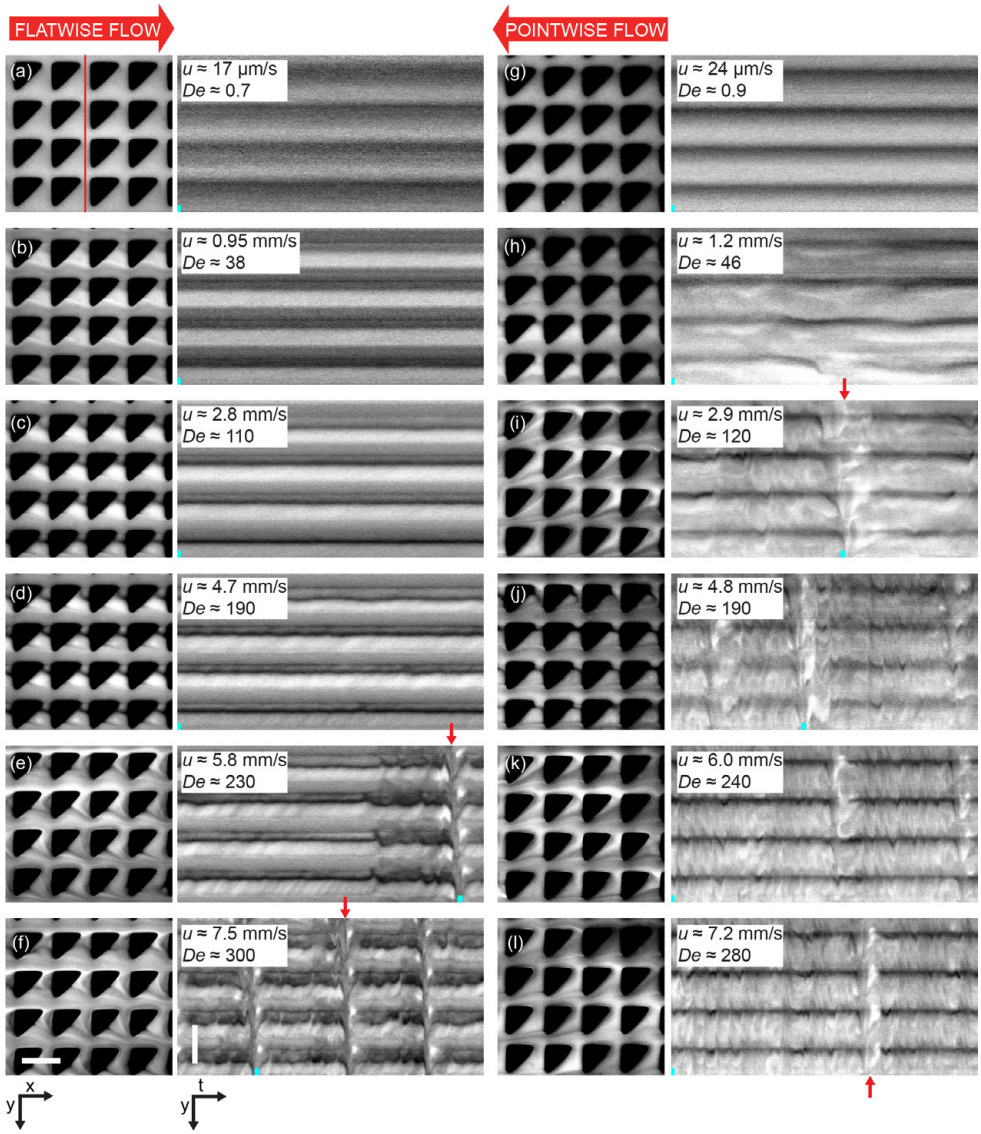

Figure 8.8. Microscopic flow dynamics as a function of flow velocity for the two flow directions. The left-hand side show fluorescent micrographs whereas the right-hand side show the corresponding kymograph. The red arrows point at wave occurrences. The teal bar indicates where in the kymograph the micrograph has been taken. Scale bars are 20 µm. Each kymograph span a total of 15 s.

9. Outlook

9.1 Device Integration

A future goal is a stand-alone, fully-integrated device that can perform all preparation and analysis steps for multiple sample types. In Paper II, only two steps were combined, but with more development, also the sample clean-up, cell isolation, DNA extraction and other genetic analysis techniques such as next-generation sequencing could be integrated. The end goal would be a sample-in, answer-out type of system that would work at the point of care. No pre-processing would be needed that many of the state-of-the-art systems now require. The device would need minimal or no training to use and the results would be easy to interpret. Large, bulky and expensive external equipment would be discarded for small, portable and cheaper alternatives. Flow pumps can be built-in and their handling automated. Due to the small dimensions of microfluidics components, many devices can fit together on a single chip. Multiple samples can therefore be processed in parallel within the same chip. While integration comes with many advantages, it is essential that the integrated device is not made overly complex as can easily happen when many otherwise separate processes are combined.

9.2 Separation Throughput

While we have accomplished a great improvement in the throughput of long-DNA separation in DLD (up to 24 µL/h or 760 ng/h for 166 kbp from 48.5 kbp), it can still take hours to obtain enough sample for some genetic analyses such as nanopore sequencing. The process could be further improved upon to make the process even faster and able to handle larger sample volumes (several milliliters) and sample mass (tens of micrograms) in a shorter amount of time (tens of minutes). A higher throughput would make it possible to perform analyses that require larger initial sample quantities.

To increase the throughput further, the conventional ways of increasing the throughput could be exploited to their limits. These include optimizing channel geometry (deeper and wider devices), optimizing the inlet and outlet regions and potentially parallelising the array. The effect of DLD parameters such as gap size,

periodicity and pillar diameter could be investigated. In addition to finding ways to further increase the throughput, the negative effects that normally accompany high throughput have to be considered. High shear and extensional rates could break and fragment DNA strands longer than those utilized in this work. To minimize such fragmentation, variations of channel and obstacle design could be explored.

9.3 Separation of Clinical Samples

The work performed in this thesis mostly relied on purified monodisperse DNA samples. While the aim was to present a proof-of-principle device, handling clinical samples could demonstrate the full potential of the technology. Clinical samples may typically be contaminated with cell debris or other material that might clog the channels or lead to extensive bio-fouling, worsening the separation quality. To minimize any such problems, a pre-separation washing step would be advisable.

The practical demands for long-DNA sample preparation highly depends on the sample type and the goal of the preparation. If the sample concentration is too high, dilution might be necessary. Is the purpose to eliminate all short strands from the long ones or is only an enrichment of long DNA strands sufficient? It could be that the small strands are not an issue but instead other contaminants, *e.g.* reagents from previous processing steps. It could be that a buffer exchange of the long DNA is needed or that a high-resolution, long-DNA-strand separation is required. With a versatile separation method such as DLD, the device can be designed accordingly. In many cases, a custom-made device design is not required due to its high dynamic range and tunability.

9.4 Elastic Effects

The elastic phenomena presented in this work have just been discovered and great prospects in further investigations of the flow dynamics and exploration of related effects awaits the avid scientist. We call for curious theoreticians to help us understand the underlying mechanisms and ask for interested simulation experts to numerically simulate the emergence of the DNA waves.

The parameter space for studying elastic phenomena in micropillar arrays, that is presented in this work, is vast. Effects of pillar size, channel depth, array spacing, array width, and more alternative pillar distribution patterns and pillar shapes, are outside the scope of this thesis and for others to explore. It could be interesting to explore viscoelastic fluids such as aqueous wormlike micellar solutions or

polymers other than DNA (*i.e.* polyacrylamide or polyethylene oxide). The flow dynamics might be entirely different if *e.g.* the persistence length of the polymers is dramatically shorter.

Elastic effects that lead to flow instabilities have proven to be detrimental to the sorting that crucially relies on stable flow streams (see Paper I). By further understanding what conditions give rise so such effects, effort can be made to avoid them (*e.g.* through alternative pillar shapes or changing the spacing).

Elastic flow in microfluidic devices have been shown to enhance mixing [17] as well as being the cause for a fluidic diodicity [147]. It is possible that the waves presented here could give rise to similar outcomes.

The flow of DNA solutions in the 2D micropillar array is an example of flow of a viscoelastic fluid across porous media. The elastic phenomena found in this work could have impact into various applications that are based on such flow. These include pathogen clearing in the mucus in the lungs, industrial polymer processing, mixing for lab-on-a-chip systems, enhanced oil recovery and groundwater remediation.

9.5 From Lab to Patient

Surprisingly few microfluidic technologies have been commercialized [165, 166]. Many of the published methods stay in academia and are never fully utilized to the benefit of society. One of the reasons that has been identified is the lack of standardization of microfluidic devices. Protocols, equipment and material in the research environment differ from and are not compatible with those used in the private sector [165]. Thus, in order for the research to reach actual patients, this gap must be bridged in future device versions.

In our work, we have used PDMS as the main chip material. PDMS has been avoided in industry due to problems with up-scaling and manufacturability [165]. We have chosen this material due the superior speed with which device prototypes can be fabricated. However, it would not be difficult for us to change material when we have proven the principle of the technology as we are not dependent on any specific material property of PDMS.

This work is only on the level of proof-of-principle. In order for the technology to become wide-spread, it has to be further optimized in terms of device-device reproducibility. There can only be minimal variability in the analysis result among devices. The devices must be tested for real-life conditions. Variations in temperature, storage time, and timing of user actions can influence the results.

Implementing the result of our work in actual biomedical applications could reduce the time for diagnosing certain infectious and genetic diseases. Reducing the time for diagnosis is crucial. In general, the shorter time a disease has progressed, the easier it is to treat it, with less side-effects and requiring less resources.

For diagnostic tests of infectious diseases in resource-poor conditions, the **ASSURED** criteria from the World Health Organization should be followed. While such a test is outside the scope of the thesis, it is important to keep it in mind while developing components that could be useful for such purposes. ASSURED stands for **A**ffordable, **S**ensitive, **S**pecific, **U**ser-friendly (simple to perform in a few steps with minimal training), **R**apid and robust (results available in less than 30 min, long shelf time), **E**quipment-free and **D**eliverable to end-users (portable, hand-held) [167]. These categories must be included when planning for the next generation of the devices if the end goal of patient care is to be reached.

Appendix 1: Lab Protocols

While lab protocols can never fully replace in-house training, they are useful in order to replicate procedures for users with sufficient experience. Note that a risk assessment should always be carried out for handling chemicals to minimize personal exposure and harm. The following appendix contains a number of lab protocols used in the work.

1.1 UV Lithography Protocol

The following protocol applies to SU-8 2015 for 12 µm deep features. For features with an alternative depth, slightly different spin speeds are used. Please visit the fabrication protocols at Microchem (now Kayaku, https://kayakuam.com/products/su-8-2000/).

Equipment/Material

- Silicon Wafers, 3" (SIEGERT WAFER GmbH, Aachen, Germany)
- SU-8 2015 (Micro resist technology GmbH, Berlin, Germany)
- Spin coater
- Hotplates
- Mask aligner (Karl Süss MJB3 and MJB4, Münich Germany)
- Convection Oven
- Edge Bead Remover (Performus IV (EBR PG, microChem)
- SU-8 developer, mr-Dev 600 (Microresist Technology)
- Anti-sticking agent (1H,1H,2H,2H-perfluorooctyltrichlorosilane, PFOTS (ABCR GmbH & Co. KG, Karlsruhe, Germany))
- Glove box
- Nitrogen gun

#1 Substrate Pre-treatment

1. **Wash** the wafer with acetone, isopropanol and DI-water. Blow dry with Nitrogen gun.
2. **Bake** at 200 °C hotplate for 5 min to dehydrate the substrate and allow the substrate to cool to room temperature

#2 SU-8 Spin Coating

1. **Static Dispense** with approximately 1 ml of SU-8 per inch of wafer diameter.
2. **Spreading Spin** at 500 rpm for 5 s with acceleration of 100 rpm/s then a main spin at 4000 rpm for 60 s with acceleration of 300 rpm/s.

#3 Soft Baking

1. **Soft-bake** on hot-plate for 30 s at 65 °C
2. **Soft-bake** on hot-plate for 3 minutes at 95 °C
3. **Edge Bead Removal** if visible edge beads (Both normal & coffee ring effect-derived edge beads). For my devices, the edge bead remover was used according to the manufacturer's protocol. Removing the edge bead yields better resolution, esp. for thicker features.)

#4 UV Treatment & Development

1. **UV Exposure** (near UV (350–400nm)) - Total energy per surface area of 135 mJ/cm^2. Set wedge-edge correction (WEC) to 14–15 mPa. Use 6.8 s exposure dose with a constant intensity of 20mW/cm^2 using no-vacuum contact mode with a mask aligner.
2. **Post-Exposure Bake**
    a. Post-Exposure Bake for 4 min at 95 °C. Let cool down to room temperature for 4-5 min.
3. **Development** with the developer for 3 min.
4. **Rinsing** with the developer & Isoproponal for 10 s each and then **drying** with nitrogen gas.
5. **Hard Bake** for 2 h at 200 °C in a convection oven.

#5 Anti-Adhesion Treatment

1. Insert the wafer into a glove box containing a nitrogen atmosphere.
2. Place the wafers inside a glass dish, insert 80 µl (depending on the size of the dish) of the agent (1H,1H,2H,2H-perfluorooctyltrichlorosilane, PFOTS) and seal the hole in the lid with a glass slide.
3. Set the heating to about 180 °C (boiling temperature of PFOTS is 192 °C)
4. Let sit for minimum 4 h.

1.2 Maskless Photolithography Protocol

This protocol involves fabrication of microfluidic molds using a maskless aligner. It enables faster prototyping of microfluidic designs without the need of photomasks. The resulting feature thickness of this protocol is 11.5 µm.

Equipment/Material

- 4 inch silicon wafer
- Spin coater
- Convection oven
- mrDWL40 resist (Micro Resist Technology GmbH, Berlin, Germany)
- Maskless aligner (MLA150 maskless lithography system, Heidelberg Instruments GmbH, Heidelberg, Germany)
- Oxygen plasma system (Plasma Preen, NJ, USA)
- Atomic Layer Deposition (ALD) system (Fiji – Plasma Enhanced ALD, Veeco, NY, USA).

Process

1. Spin coating on 4 inch wafers. First treat the wafers with oxygen plasma for 60 s for enhanced adhesion of the resist. Then spin the resist at 5000 rpm for 60 s. The resulting thickness at this spin speed is 13.3 µm.
2. Expose the coated wafer at approx. 450 mJ/cm^2 with a 405 nm laser with the maskless aligner.
3. Hard bake the exposed wafer at 120 °C for 10 minutes. Note that the resist layer settled at 11.5 µm.
4. Anti-sticking treatment. Deposit a layer of aluminium oxide followed by a monolayer of Perfluordecyltriklorosilan (FDTS) using an ALD system.

1.3 Cyclo Olefin Polymer Glass Coating

The following protocol is used to spin a thin film of cyclo olefin polymer that is used for stretching of DNA on a hydrophobic surface.

Equipment/Material

- For dissolution:
    - ZEONEX crystals (Zeon Chemicals L.P., Louisville, USA)
    - sec-Butylbenzene (Sigma-Aldrich)
- For the Coating process:
    - Scale, hot plate, ultrasonicator and a spin-coater
    - Pasteur Pipettes (1 mL)
    - Glass coverslips (22 × 22 mm, Menzel-Gläser no. 1.5, Germany)

Dissolution

1. Dissolve a piece of ZEONEX in sec-Butylbenzene to obtain 0.8% (w/v) ZEONEX solution. The dissolution takes around 3 h.

Coating Process

1. Wipe the coverslips with a cleanroom cloth dipped in IPA.
2. Wash the coverslips by ultrasonication (highest power) for 5 min in acetone, followed by 5 min in isopropanol and finally followed by 5 min in Milli-Q® water. Dry with nitrogen and put on the 140 °C hotplate for a couple of minutes to completely evaporate all water.
3. Insert it onto the spin-coater chuck and dispense 30–40 µL (~3 drops) of ZEONEX on top of a cover slip with a 1 mL plastic Pasteur pipette (Make sure to dispose the first 1–2 drops in the waste due to their high air bubble content. Make also sure there are no bubbles on the slide in the spin coater).
4. Spin coat. Ramp at 500 RPM for 2 s with an acceleration of 1200 RPM/s and then spin at 3000 RPM for 45 s.
5. Post-bake at 140 °C for 1 h immediately after coating to smoothen the surface.
6. Store at room temperature in a desiccator or a container sealed with parafilm

1.4 Replica Molding

The following protocol describes the standard procedure for replica molding that is used to make our microfluidic devices.

Equipment/Material

- Poly-Di-Methyl-Siloxane (PDMS), SYLGARD® 184 Silicone Elastomer Kit, Dow Corning)
- Scotch Tape (3M, Maplewood, MN, USA)
- (Optional) Reservoir glue, silicone adhesive A07 (Wacker Chemie AG, München, Germany)
- Plasma System, (Zepto, Diener electronic GmbH & Co. KG, Ebhausen, Germany)
- (Optional) Silicone tubes, 3 mm inner, 5 mm outer diameter
- Glass substrate: Microscope slides (76 × 26 mm, Menzel-Gläser) or Glass coverslips (22 × 22 mm, Menzel-Gläser no. 1.5, Germany) for imaging with high-magnification and low working distance oil-immersion objectives.
- Desiccator
- Hole Puncher (Syneo Trading GmbH, Munich, Germany). Make sure to sharpen before usage if found to be dull.
- Lab coat (to minimize fabric threads from clothes falling onto the devices.)

#1 PDMS Replica Fabrication

1. Thoroughly mix PDMS monomer and curing agent, ratio of 10:1.
2. Degas the PDMS mixture in a vacuum desiccator for 20–30 min to eliminate bubbles formed during mixing.
3. Pour the mixture onto the silicon wafer (verify that there are no bubbles on the master after pouring)
4. Bake in oven for 1 h at 80 °C. Make sure to keep the substrate level inside the oven to avoid an uneven PDMS layer.
5. Store on a clean plastic sheet until use.

#2 Punch reservoir holes with the hole-puncher

6. Punch holes from the channel feature side of the PDMS to make cleaner cuts. Verify that the punched holes are free from residue. See Table A1.1 for an overview of the punch sizes used for what tubing.

Table A1.1. What puncher size for what tubing size? For direct insertion into a thick PDMS slab instead of using external, glued-on silicone reservoirs.

Tubing material (used in this work)	Tubing outer diameter	Puncher cutting edge diameter
Tygon	1/8 inch or 3.2 mm	2.97 mm (Accu-punch, Syneo, West Palm Beach, Florida USA)
Ethylene tetrafluoroethylene (ETFE)	1/16 inch or 1.6 mm	2 mm (in-house design)

#3 PDMS Bonding

7. Pre-Plasma Cleaning. Apply scotch tape two times to the feature side of the PDMS slab and blow away any residual particles with a nitrogen gun. Clean the glass substrate by washing with IPA and then DI-water and then blow-drying with nitrogen gas.
8. Verify that there is no dust or other particles clogging the device.
9. Plasma Oxidation. Optimized times are 8 s for PDMS, 30s for glass and 3.5 min for Zeonex-coated glass at full power.
10. Bonding to substrate. Make sure that you start from one side and slowly attach the rest of the PDMS in a continuous manner.
11. Post-Plasma Baking at 80 °C for 2 min to enhance the bonding.

(Optional) Gluing of tube reservoirs

12. Glue the silicone tubes on top of the access holes of the PDMS slab. Verify that no glue has clogged the channel entrance and that there is no glue missing around the tube-PDMS interface. This is to prevent leakage when experimenting.
13. Wait 30 min to 1h for the glue to cure inside a box. Add water inside the box (but not onto the devices directly) to fasten the polymerization of the glue. When complete, open the box under a hood to minimize toluene exposure.
14. Gluing Verification step - verify that there is no leak from the gluing by visual inspection.

#4 Thermal aging baking for a hydrophobic channel surface

15. Put the device for 24 h in an oven at 120 °C.

(Optional) Mold replication

To minimize damage to the master mold and to speed-up the device fabrication, some of the molds were replicated using the protocol in [168]. To summarize, UV-curable adhesive glue (Norland optical adhesive 63, NOA63, Norland, US) was poured over the PDMS mold. The glue was sealed with a glass slide with metal clamps and exposed to UV light for approximately 40 min. To fully evaporate glue residue, the glue replica was baked overnight in the oven at 80 °C.

1.5 Troubleshooting: Fabrication and Experimentation

The three R:s of experimentation: "When you run into a seemingly unsolvable problem, complete the following set of tasks: ***relax****, take 10 deep breaths,* ***read*** *the literature, and then finally* ***repeat*** *the experiments with the new-found knowledge."*

Jonas O. Tegenfeldt

This section briefly describes commonly encountered problems and how to deal with them effectively. The hope is that it can be of use to future students and minimize frustration in the lab.

Difficulty in Wetting the Device

To make the wetting process easier, ethanol can be inserted as a first step before introducing aqueous solutions. Ethanol has a much lower surface tension and easily wets narrow hydrophobic channels.

Trapped Bubbles in Microchannels

Apply maximum pressure to all access holes (inlets and outlets) and wait 20 min. This will create a pressure gradient from the channel to the other side of the porous PDMS at ambient pressure. It will also increase the gas solubility in the liquid. Both of these effects will force the trapped air out of the microchannels.

Another way to minimize the presence of bubbles is to degas the buffer beforehand. This is performed most efficiently under the impact of an ultrasonicator under vacuum.

Plasma-bonding Failure

The failure of plasma-bonding between PDMS and glass can have multiple causes. If the chamber atmosphere is humid, it could ruin the process. Other possible causes are insufficient surface cleaning or contamination by *e.g.* fingerprints. Make sure to clean the plasma chamber with isopropanol regularly to prevent build-up of contaminants.

Device Breakage

The glass coverslip substrates used in this thesis makes the devices fragile and prone to breakage. To keep the devices intact, always transfer them using a robust holder. Never insert or dislodge fluidic connection to the chip while it is mounted on the microscope. Always do this step when the device is on-top of a flat and solid substrate.

Channel Leakage

To minimize leakage, always double-check the bonding steps. If you are using glue, exploit the difference in the refractive index of the glue to the glass by manually inspecting it with light to find out the glue has spread properly.

Channel Blockage

To minimize blocking and disturbances of the flow, always filter the liquids from particles. Wet the device from the outlet to minimize the collection of particles in the inlet of the device. When making devices, use a lab coat and make sure you do not shed particles from hair on your face or head. If the device was designed correctly, the dust particles will be trapped in the outlet filter.

Auto-fluorescence

Single molecule fluorescence images can be ruined if the device material is auto-fluorescent. Make sure that highly auto-fluorescent material such as silicone tubing is kept well away from the region of interests. Minimize background fluorescence by using surface passivation schemes and low dye concentrations.

1.6 DNA Staining

The following protocol is a standard protocol for staining double-stranded DNA with intercalating monomethine cyanine dyes (*e.g.* YOYO-1 Iodide [491ex/509em, Thermofisher, MA, United States]). The dye to base pair ratio used was 1:10 (Papers I and II), or 1:50 and 1:200 (Papers III–IV).

1. Aliquot the dye solution to prevent multiple thaw-freeze cycles. Do not store diluted aliquots as the dye molecules will deteriorate in aqueous environments.
2. Thaw the DNA sample and the dye solution aliquot. Mix the DNA solution by repeated turning upside-down and tapping the tube. Mix the dye solution by vortexing for 20 s.
3. Add TE-buffer (1 × TE equals 10 mM Tris-HCl and 1 mM EDTA) and the dye to the water, vortex, and then add the DNA sample last. Mix by flicking the tube approximately 20 times.
4. Heat for 2 h at 50 °C on a heat-block, and make sure to have the solution protected from light by placing aluminium foil on-top of the tube.
5. Store in the fridge at approximately 4 °C until use.

Appendix 2: Numerical Simulations

The hydrodynamic flow inside the microchannels used in this thesis is complex and its governing equations (see chapter 2) cannot be solved analytically. To predict the flow inside the devices in greater detail than can be drawn from a rough analysis using dimensionless numbers, the flow is simulated numerically using the finite element method (FEM). FEM solves the continuous flow equations at discrete elements in a pre-selected mesh. The simulation software used in this thesis is COMSOL Multiphysics 5.5 (COMSOL Inc. Stockholm, Sweden). In the simulations, creeping flow (low Re) was assumed together with a no-slip condition ($u = 0$) at the walls. The simulations were made in 3D. A periodic flow pattern was applied between the inlets and outlets. Note that simulations of non-Newtonian flows such as elastic turbulence is outside the scope of this work.

Appendix 3: Data Analysis

The acquired micrographs and fluorescent videographs were analysed using Python v. 3.8.3 and ImageJ v. 1.52i (Public Domain, developed at National Institutes of Health, Maryland, United States). The code associated with the thesis will be available at https://github.com/oskarestrom/phd.

3.1 Background Subtraction

For the quantitative fluorescence measurements in Papers III, IV and V, the heterogeneous background from the LED lamp with spatially uneven intensity was first subtracted. Thereafter, the non-channel background intensity was subtracted from the images. This intensity level was determined by averaging the signal in an area outside the channel.

3.2 Ionic Strength Calculation

The ionic strength, I, is calculated by summing the product of the concentration and squared charge of all ions in the solution:

$$I = \frac{1}{2}\sum_{i=0}^{n} z_i^2 c_i \quad (1)$$

where the one half is added to include both anions and cations and c_i is the concentration of an ionic species with the valence z_i.

The script calculates I based on the detailed description by Iarko *et al.* [169]. The script is written using the python library SymPy (v. 1.7.1). The first step is setting up the series of Henderson-Hasselbalch equations to be solved. With β-mercaptoethanol, the number of equations are 9 and without 7, see Table A3.1 below. The disassociation constants together with the total species concentrations are known but the concentrations of the ionic species are not.

Table A3.1. Series of Henderson-Hasselbalch equations required to solve the ionic strength of the solution. β stands for β-mercaptoethanol, T, for Tris, E for EDTA and γ_X for the activity coefficient of species x.

Formulae	Equation No.
$\frac{[TH^+]\gamma_{TH^+}[OH^-]\gamma_{OH^-}}{[T]\gamma_T} = 10^{-5.94}$	1
$\frac{[HE^{3-}]\gamma_{HE^{3-}}[H^+]\gamma_{H^+}}{[H_2E^{2-}]\gamma_{H_2E^{2-}}} = 10^{-6.16}$	2
$\frac{[E^{4-}]\gamma_{E^{4-}}[H^+]\gamma_{H^+}}{[HE^{3-}]\gamma_{HE^{3-}}} = 10^{-10.26}$	3
$\frac{[\beta^-]\gamma_{\beta^-}[H^+]\gamma_{H^+}}{[H\beta]\gamma_{H\beta}} = 10^{-9.6}$	4
$[H^+]\gamma_{H^+}[OH^-]\gamma_{OH^-} = 10^{-14}$	5
$[T] + [TH^+] = C[T]$	6
$[H_2E^{2-}] + [HE^{3-}] + [E^{4-}] = C[E]$	7
$[H\beta] + [\beta^-] = \beta[T]$	8
$[TH^+] + [H^+] = [OH^-] + 2[H_2E^{2-}] + 3[HE^{3-}] + 4[E^{4-}] + [\beta^-]$	9

The activity coefficients are calculated using the Davis equation:

$$\log_{10}\gamma_x = -0.51 z_x^2 \left(\sqrt{\frac{I}{1+\sqrt{I}}} - 0.3I \right) \quad (1)$$

where γ_x and z_x are the activity coefficient and valence of species x, respectively. Note because that the activity coefficients depend on the ionic strength which in turn depend on the activity coefficients, the system of equation is iterated until a converging solution is found. The initial value of the activity coefficients are set to 1. The percent error (100 × [calculated value – literature value] / literature value) is below 0.6% based on the values from [170].

3.3 Analysis of Polarization Images

The beam splitter divided the two polarization channels to either side of the camera sensor. The heterogeneous background from the uneven lamp intensity across the field of view was first subtracted. Then, the image was split into the two polarization images. These images were then aligned on-top of each other using an Enhanced Correlation Coefficient (ECC) image alignment algorithm from the OpenCV package in Python (v. 4.5.5.64). To be able to visualize both the total fluorescent intensity and the polarization signal in the same image, the hue, saturation and value (HSV) model was applied. The normalized intensity corresponded to the value and the polarization emission ratio, $P = (I_{\parallel} - I_{\perp})/(I_{\parallel} + I_{\perp})$, corresponded to the hue, where $I_{\parallel}$ and $I_{\perp}$ corresponds to the intensity of the parallel and the perpendicular polarization channels, respectively. It was generally set so that $P = 0.2$ corresponded to 0 (red) and $P = -0.2$ corresponded to 1/3 (green) in the hue of the HSV model. The saturation was set to 1 for all images, not containing any information.

Note that the alignment of the two-channels is improved if the physical pixel size of the camera is smaller. We noticed a great enhancement by changing from 16 µm in pixel width to 6.5 µm.

Appendix 4: Pressure Control System Schematics for Paper II

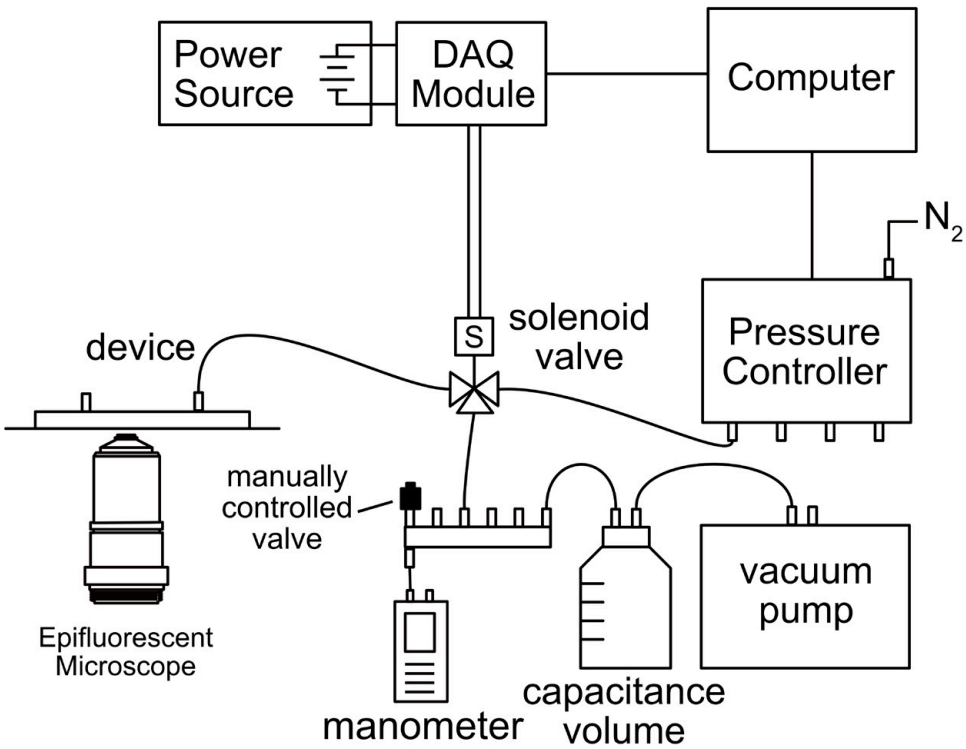

Figure A4.1. Pressure control scheme for the on-chip combing chip of Paper II. Only the pressure controller is used for the other experiments. This scheme is simplified as only one channel from the pressure controller is visible. Multiple pressure channels have been added during the experiments. Negative pressure is generated with the vacuum pump (mini diaphragm vacuum pump, VP 86, VWR). A glass bottle is added as a pressure capacitance. The pressure is regulated using a valve and measured with a manometer. Positive pressure is generated from an in-house nitrogen overpressure gas source. The pressure is controlled using a pressure controller (MFCS-4C pressure controller, Fluigent, Paris, France) connected to a computer. The switching between the positive and negative pressure systems are performed with a solenoid valve (SCS067A061, ASCO, Florham Park, NJ, USA). The solenoid valve is controlled by a DAQ-module (cDAQ-9174, National Instruments, Austin, TX, USA) which is connected to a computer. The DAQ-module is powered by a power source (24 V DC Power source, MI-40A, METRIC). The device is imaged using an epifluorescence microscope.

Appendix 5: 2D Fourier Analysis

In Papers IV and V, the algorithm Fast Fourier Transform (FFT) was applied to the fluorescent micrographs of the flow in two-dimensional (2D) pillar arrays. This appendix aims to give a brief overview how it works with some related examples.

FFT was first known to Carl Friedrich Gauss in 1805 but never published. In 1965 it was re-invented by James Cooley and John Turkey which popularized the algorithm [171]. Compared to other discrete Fourier Transform algorithm, FFT takes advantage of symmetries that leads to $O(N \log N)$ scaling instead of $O(N^2)$.

FFT is a discrete Fourier Transform, meaning that a signal (a sequence of N complex numbers x_0, x_1,…,x_{N-1}) in the time (or space) domain is converted to a limited sequence of complex numbers in the frequency domain (X_0, X_1,…,X_{N-1}):

$$X_k = \sum_{n=0}^{N-1} x_n \cdot e^{-\frac{i2\pi}{N}kn}, k = 0, \dots, N-1 \quad \text{(A5.1)}$$

The two-dimensional version of FFT works in the same way but for two dimensions. The resulting vector that one receives in Python when applying numpy.fft contains *N* terms with the first term containing the zero frequency (the sum of the signal). The second to *N*/2 terms contain the positive-frequency terms and *N*/2+1 to the *N* terms contain the negative frequency terms. After the transform has been shifted, the zero frequency term is placed in the middle of the array at (*N*+1)/2. The amplitude, frequency and phase can then be extracted from each frequency component.

The 2D FFT was calculated in Python, using the function fft.fft2 from the NumPy library. The transform was shifted with the function fft.fftshift so that the zero frequency component is centered in the transform. The function fft.ifft2 was used to compute the inverse Fourier transform

See examples of 2D Fourier filters and their corresponding inverse transforms of a DNA waves fluorescent micrograph in Figure A5.1. From it, it is clear that the waves are made of a number of spatial frequencies, although some frequency components have a larger share as seen in Figure A5.1(I and K).

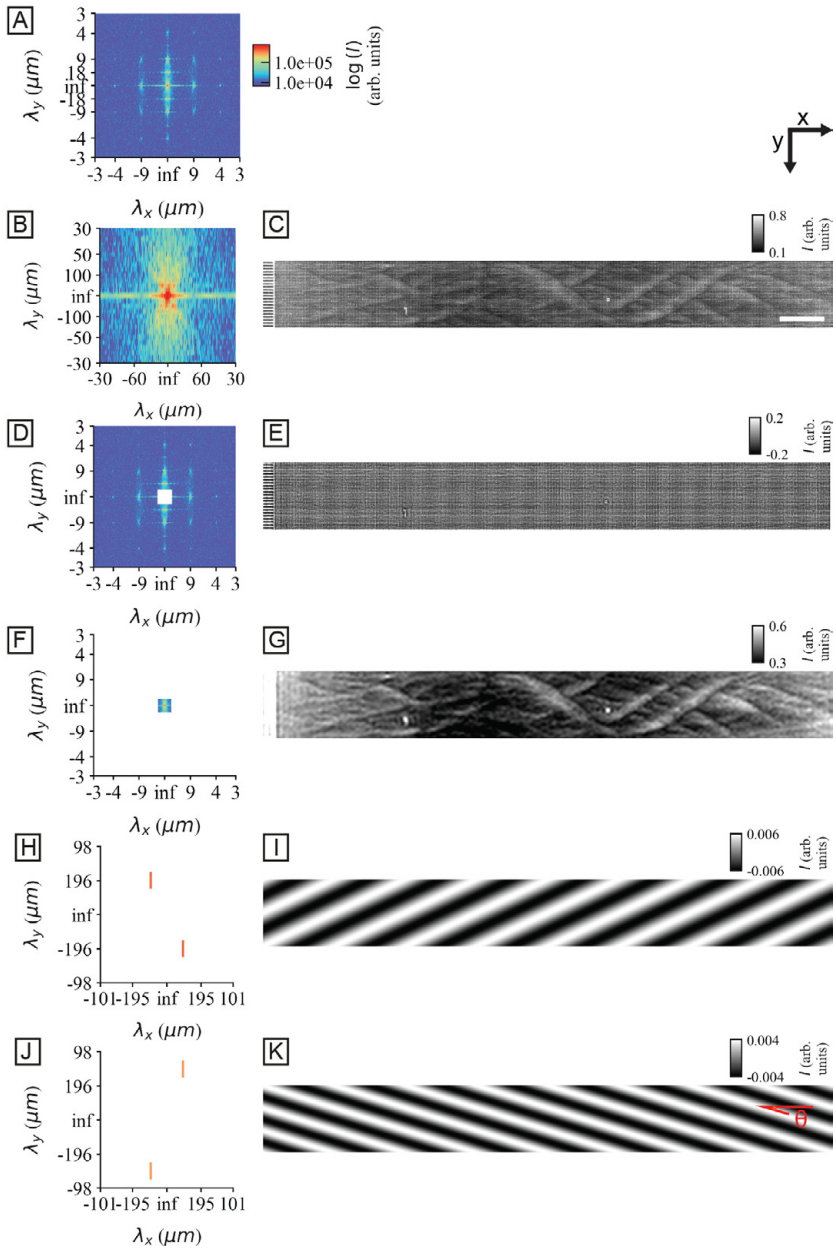

Figure A5.01. Example of Fourier amplitude spectra with corresponding inverse transforms of various filters. Note that the spectra are shifted with the zero amplitude frequencies in the center and spatial frequency is on the spectral axes instead of frequencies. The white areas in the filters are set to zero. (**C**) shows the raw fluorescent micrograph of DNA waves in a quadratic pillar array. (**A**) and (**B**) show the full and zoomed-in spectra corresponding to (C). (**D**) and (**F**) show a square high-pass and low-pass filters, with their corresponding inverse spectra (**G**) and (**I**), respectively. (**H**) and (**J**) show the peak wavelengths of either side of the spectrum with the corresponding single frequency inverse spectra in (**J**) and (**K**), respectively. The colorbar in (A) is valid for all spectra. The colorbars on the right-hand side of the image are set to highlight the features from the corresponding mask. The scale bar is 500 μm.

References

1. Watson, J.D. and F.H.C. Crick, *The structure of DNA*, in *Cold Spring Harbor symposia on quantitative biology*. 1953. p. 123-131.
2. Lander, E.S., et al., *Initial sequencing and analysis of the human genome.* 2001.
3. Chaisson, M.J., R.K. Wilson, and E.E. Eichler, *Genetic variation and the de novo assembly of human genomes.* Nature Reviews Genetics, 2015. **16**(11): p. 627-640.
4. Wijmenga, C., et al., *Chromosome 4q DNA rearrangements associated with facioscapulohumeral muscular dystrophy.* Nature genetics, 1992. **2**(1): p. 26-30.
5. Howorka, S., S. Cheley, and H. Bayley, *Sequence-specific detection of individual DNA strands using engineered nanopores.* Nature biotechnology, 2001. **19**(7): p. 636-639.
6. Eid, J., et al., *Real-time DNA sequencing from single polymerase molecules.* Science, 2009. **323**(5910): p. 133-138.
7. Müller, V. and F. Westerlund, *Optical DNA mapping in nanofluidic devices: principles and applications.* Lab Chip, 2017. **17**: p. 579-590.
8. Zheng, G.X., et al., *Haplotyping germline and cancer genomes with high-throughput linked-read sequencing.* Nature biotechnology, 2016. **34**(3): p. 303-311.
9. Dorfman, K.D., et al., *Beyond gel electrophoresis: Microfluidic separations, fluorescence burst analysis, and DNA stretching.* Chemical Reviews, 2013. **113**: p. 2584-2667.
10. Schwartz, D.C. and C.R. Cantor, *Separation of yeast chromosome-sized DNAs by pulsed field gradient gel electrophoresis.* cell, 1984. **37**: p. 67-75.
11. Kovacic, R.T., L. Comal, and A.J. Bendich, *Protection of megabase DNA from shearing.* Nucleic Acids Research, 1995. **23**: p. 3999-4000.
12. Schalamun, M., et al., *Harnessing the MinION: An example of how to establish long-read sequencing in a laboratory using challenging plant tissue from Eucalyptus pauciflora.* Molecular ecology resources, 2019. **19**(1): p. 77-89.
13. Wunsch, B.H., et al., *Gel-on-a-chip: continuous, velocity-dependent DNA separation using nanoscale lateral displacement.* Lab on a Chip, 2019. **19**(9): p. 1567-1578.
14. Ertaş, D., *Lateral separation of macromolecules and polyelectrolytes in microlithographic arrays.* Physical Review Letters, 1998. **80**(7): p. 1548.

15. Huang, L.R., et al., *A DNA prism for high-speed continuous fractionation of large DNA molecules.* Nature Biotechnology, 2002. **20**: p. 1048-1051.
16. Huang, L.R., et al., *Continuous Particle Separation Through Deterministic Lateral Displacement.* Science, 2004. **304**: p. 987-990.
17. Groisman, A. and V. Steinberg, *Efficient mixing at low Reynolds numbers using polymer additives.* Nature, 2001. **410**(6831): p. 905-908.
18. Ström, O., *RBC deformability fractionation and hydro- dynamic trapping for studying Plasmodium Falciparum infection*. 2017.
19. Folch, A., *Introduction to bioMEMS.* 2016.
20. Bruus, H., *Theoretical microfluidics*. Vol. 18. 2008: Oxford university press Oxford.
21. Smith, D.E., H.P. Babcock, and S. Chu, *Single-polymer dynamics in steady shear flow.* Science, 1999. **283**(5408): p. 1724-1727.
22. Di Carlo, D., *Inertial microfluidics.* Lab on a Chip, 2009. **9**(21): p. 3038-3046.
23. Squires, T.M. and S.R. Quake, *Microfluidics: Fluid physics at the nanoliter scale.* Reviews of Modern Physics, 2005. **77**: p. 977-1026.
24. Schroeder, C.M., *Single polymer dynamics for molecular rheology.* Journal of Rheology, 2018. **62**(1): p. 371-403.
25. Rivetti, C., C. Walker, and C. Bustamante, *Polymer chain statistics and conformational analysis of DNA molecules with bends or sections of different flexibility.* Journal of molecular biology, 1998. **280**(1): p. 41-59.
26. Pray, L., *Discovery of DNA structure and function: Watson and Crick.* Nature Education, 2008. **1**(1).
27. Bates, A.D., A. Maxwell, and others, *DNA topology.* 2005.
28. Kundukad, B., J. Yan, and P.S. Doyle, *Effect of YOYO-1 on the mechanical properties of DNA.* Soft matter, 2014. **10**: p. 9721-9728.
29. Nyberg, L., et al., *Heterogeneous staining: A tool for studies of how fluorescent dyes affect the physical properties of DNA.* Nucleic Acids Research, 2013. **41**.
30. Spielmann, H.P., D.E. Wemmer, and J.P. Jacobsen, *Solution structure of a DNA complex with the fluorescent bis-intercalator TOTO determined by NMR spectroscopy.* Biochemistry, 1995. **34**(27): p. 8542-8553.
31. Reisner, W., J.N. Pedersen, and R.H. Austin, *DNA confinement in nanochannels: Physics and biological applications.* Reports on Progress in Physics, 2012. **75**.
32. Odijk, T., *Polyelectrolytes near the rod limit.* Journal of Polymer Science: Polymer Physics Edition, 1977. **15**(3): p. 477-483.
33. Skolnick, J. and M. Fixman, *Electrostatic persistence length of a wormlike polyelectrolyte.* Macromolecules, 1977. **10**(5): p. 944-948.
34. Dobrynin, A.V., *Effect of counterion condensation on rigidity of semiflexible polyelectrolytes.* Macromolecules, 2006. **39**(26): p. 9519-9527.
35. Rubinstein, M. and R.H. Colby, *Polymer physics*. Vol. 23. 2003: Oxford university press New York.

36. Doi, M., *Introduction to polymer physics*. 1996: Oxford university press.
37. Smith, D.E., T.T. Perkins, and S. Chu, *Dynamical scaling of DNA diffusion coefficients.* Macromolecules, 1996. **29**(4): p. 1372-1373.
38. Li, B., N. Madras, and A.D. Sokal, *Critical exponents, hyperscaling, and universal amplitude ratios for two-and three-dimensional self-avoiding walks.* Journal of Statistical Physics, 1995. **80**(3-4): p. 661-754.
39. De Gennes, P.-G. and P.-G. Gennes, *Scaling concepts in polymer physics*. 1979: Cornell university press.
40. Doi, M. and S.F. Edwards, *The theory of polymer dynamics*. Vol. 73. 1988: oxford university press.
41. Graessley, W.W., *Polymer chain dimensions and the dependence of viscoelastic properties on concentration, molecular weight and solvent power.* Polymer, 1980. **21**(3): p. 258-262.
42. Pan, S., et al., *Universal solvent quality crossover of the zero shear rate viscosity of semidilute DNA solutions.* Journal of Rheology, 2014. **58**(2): p. 339-368.
43. Pan, S., et al., *Viscosity radius of polymers in dilute solutions: Universal behavior from DNA rheology and Brownian dynamics simulations.* Macromolecules, 2014. **47**(21): p. 7548-7560.
44. Banik, S., et al., *Monodisperse Lambda DNA as a Model to Conventional Polymers: A Concentration-Dependent Scaling of the Rheological Properties.* Macromolecules, 2021. **54**(18): p. 8632-8654.
45. Bustamante, C., et al., *Entropic Elasticity of $\lambda $-Phage DNA.* Proc. Nati. Acad. Sci USA, 1991. **88**: p. 10009.
46. Marko, J.F. and E.D. Siggia, *Stretching dna.* Macromolecules, 1995. **28**(26): p. 8759-8770.
47. Bustamante, C., et al., *Single-molecule studies of DNA mechanics.* Current opinion in structural biology, 2000. **10**: p. 279-285.
48. Bustamante, C., et al., *Entropic elasticity of λ-phage DNA.* Science, 1994. **265**(5178): p. 1599-1600.
49. Bao, G., *Mechanics of biomolecules.* Journal of the Mechanics and Physics of Solids, 2002. **50**(11): p. 2237-2274.
50. Smith, S.B., Y. Cui, and C. Bustamante, *Overstretching B-DNA: the elastic response of individual double-stranded and single-stranded DNA molecules.* Science, 1996. **271**(5250): p. 795-799.
51. Cluzel, P., et al., *DNA: an extensible molecule.* Science, 1996. **271**(5250): p. 792-794.
52. Lai, P.-Y. and Z. Zhou, *B-to S-form transition in double-stranded DNA with basepair interactions.* Physica A: Statistical Mechanics and its Applications, 2003. **321**(1-2): p. 170-180.
53. Schroeder, C.M., et al., *Characteristic periodic motion of polymers in shear flow.* Physical review letters, 2005. **95**(1): p. 018301.
54. Perkins, T.T., D.E. Smith, and S. Chu, *Single polymer dynamics in an elongational flow.* Science, 1997. **276**(5321): p. 2016-2021.

55. Smith, D.E. and S. Chu, *Response of flexible polymers to a sudden elongational flow.* Science, 1998. **281**(5381): p. 1335-1340.
56. De Gennes, P., *Molecular individualism.* Science, 1997. **276**(5321): p. 1999-2000.
57. Schroeder, C.M., et al., *Observation of polymer conformation hysteresis in extensional flow.* Science, 2003. **301**(5639): p. 1515-1519.
58. Zimm, B.H., *Dynamics of polymer molecules in dilute solution: viscoelasticity, flow birefringence and dielectric loss.* The journal of chemical physics, 1956. **24**(2): p. 269-278.
59. Shaqfeh, E.S., *The dynamics of single-molecule DNA in flow.* Journal of Non-Newtonian Fluid Mechanics, 2005. **130**(1): p. 1-28.
60. Perkins, T.T., D. Smith, and S. Chu, *Relaxation of a single DNA molecule observed by optical microscopy.* Science, 1994. **264**(5160): p. 822-826.
61. Schwartz, D.C., et al., *Ordered restriction maps of Saccharomyces cerevisiae chromosomes constructed by optical mapping.* Science, 1993. **262**: p. 110-114.
62. Tegenfeldt, J.O., et al., *The dynamics of genomic-length DNA molecules in 100-nm channels.* Proceedings of the National Academy of Sciences, 2004. **101**: p. 10979-10983.
63. Moffitt, J.R., et al., *Recent advances in optical tweezers.* Annual review of biochemistry, 2008. **77**.
64. Jing, J., et al., *Automated high resolution optical mapping using arrayed, fluid-fixed DNA molecules.* Proceedings of the National Academy of Sciences, 1998. **95**: p. 8046-8051.
65. Granéli, A., et al., *Organized arrays of individual DNA molecules tethered to supported lipid bilayers.* Langmuir, 2006. **22**(1): p. 292-299.
66. Granéli, A., et al., *Long-distance lateral diffusion of human Rad51 on double-stranded DNA.* Proceedings of the National Academy of Sciences, 2006. **103**(5): p. 1221-1226.
67. Bensimon, A., et al., *Alignment and sensitive detection of DNA by a moving interface.* Science, 1994. **265**: p. 2096-2098.
68. Bensimon, D., et al., *Stretching DNA with a receding meniscus: Experiments and models.* Physical Review Letters, 1995. **74**: p. 4754-4757.
69. Lam, E.T., et al., *Genome mapping on nanochannel arrays for structural variation analysis and sequence assembly.* Nature biotechnology, 2012. **30**(8): p. 771-776.
70. Kahl, V.F., et al., *Telomere Length Measurement by Molecular Combing.* Frontiers in cell and developmental biology, 2020. **8**: p. 493.
71. Reisner, W., et al., *Nanoconfinement-enhanced conformational response of single DNA molecules to changes in ionic environment.* Physical Review Letters, 2007. **99**: p. 3-6.
72. Dimalanta, E.T., et al., *A microfluidic system for large DNA molecule arrays.* Analytical Chemistry, 2004. **76**: p. 5293-5301.

73. Allemand, J.F., et al., *pH-dependent specific binding and combing of DNA.* Biophysical Journal, 1997. **73**: p. 2064-2070.
74. Deen, J., et al., *Combing of genomic DNA from droplets containing picograms of material.* ACS Nano, 2015. **9**: p. 809-816.
75. Reisner, W., et al., *Single-molecule denaturation mapping of DNA in nanofluidic channels.* Proceedings of the National Academy of Sciences, 2010. **107**: p. 13294-13299.
76. Dorfman, K.D., *DNA electrophoresis in microfabricated devices.* Reviews of Modern Physics, 2010. **82**: p. 2903-2947.
77. Rems, L., et al., *Flow of DNA in micro/nanofluidics: From fundamentals to applications.* Biomicrofluidics, 2016. **10**(4): p. 043403.
78. Mai, D.J., C. Brockman, and C.M. Schroeder, *Microfluidic systems for single DNA dynamics.* Soft matter, 2012. **8**(41): p. 10560-10572.
79. Tang, J., N. Du, and P.S. Doyle, *Compression and self-entanglement of single DNA molecules under uniform electric field.* Proceedings of the National Academy of Sciences, 2011. **108**(39): p. 16153-16158.
80. Hochstetter, A., et al., *Deterministic Lateral Displacement: Challenges and Perspectives.* ACS nano, 2020.
81. Salafi, T., Y. Zhang, and Y. Zhang, *A review on deterministic lateral displacement for particle separation and detection.* Nano-Micro Letters, 2019. **11**(1): p. 77.
82. Inglis, D.W., et al., *Critical particle size for fractionation by deterministic lateral displacement.* Lab on a Chip, 2006. **6**(5): p. 655-658.
83. Davis, J.A., *Microfluidic separation of blood components through deterministic lateral displacement*. 2008, Princeton University.
84. Kulrattanarak, T., et al., *Mixed motion in deterministic ratchets due to anisotropic permeability.* Journal of colloid and interface science, 2011. **354**(1): p. 7-14.
85. Kulrattanarak, T., et al., *Analysis of mixed motion in deterministic ratchets via experiment and particle simulation.* Microfluidics and Nanofluidics, 2011. **10**(4): p. 843-853.
86. Long, B.R., et al., *Multidirectional sorting modes in deterministic lateral displacement devices.* Physical Review E, 2008. **78**(4): p. 046304.
87. Zhang, Z., et al., *Behavior of rigid and deformable particles in deterministic lateral displacement devices with different post shapes.* The Journal of chemical physics, 2015. **143**(24): p. 243145.
88. Heller, M. and H. Bruus, *A theoretical analysis of the resolution due to diffusion and size dispersion of particles in deterministic lateral displacement devices.* Journal of Micromechanics and Microengineering, 2008. **18**: p. 75030.
89. Robertson, R.M., S. Laib, and D.E. Smith, *Diffusion of isolated DNA molecules: dependence on length and topology.* Proceedings of the National Academy of Sciences, 2006. **103**(19): p. 7310-7314.

90. Pyle, J.R. and J. Chen, *Photobleaching of YOYO-1 in super-resolution single DNA fluorescence imaging.* Beilstein journal of nanotechnology, 2017. **8**(1): p. 2296-2306.
91. Chen, Y., et al., *Concentrating genomic length DNA in a microfabricated array.* Physical Review Letters, 2015. **114**: p. 1-5.
92. Doggett, N.A., C.L. Smith, and C.R. Cantor, *The effect of DNA concentration on mobility i pulsed field gel electrophoresis.* Nucleic acids research, 1992. **20**(4): p. 859-864.
93. Ström, O.E., J.P. Beech, and J.O. Tegenfeldt, *High-Throughput Separation of Long DNA in Deterministic Lateral Displacement Arrays.* Micromachines, 2022. **13**(10): p. 1754.
94. Zeming, K.K., S. Ranjan, and Y. Zhang, *Rotational separation of non-spherical bioparticles using I-shaped pillar arrays in a microfluidic device.* Nature communications, 2013. **4**(1): p. 1-8.
95. Zeming, K.K., et al., *Real-time modulated nanoparticle separation with an ultra-large dynamic range.* Lab on a Chip, 2016. **16**(1): p. 75-85.
96. Jendrejack, R.M., et al., *DNA Dynamics in a Microchannel.* Physical Review Letters, 2003. **91**: p. 3-6.
97. Vernekar, R. and T. Krüger, *Breakdown of deterministic lateral displacement efficiency for non-dilute suspensions: A numerical study.* Medical engineering & physics, 2015. **37**(9): p. 845-854.
98. Holm, S.H., et al., *Microfluidic Particle Sorting in Concentrated Erythrocyte Suspensions.* Physical Review Applied, 2019. **12**(1): p. 014051.
99. Shui, L., et al., *Microfluidic DNA fragmentation for on-chip genomic analysis.* Nanotechnology, 2011. **22**(49): p. 494013.
100. Wu, S., et al., *DNA fragmentation in complicated flow fields created by micro-funnel shapes.* Soft Matter, 2021. **17**(40): p. 9047-9056.
101. Heo, Y. and R.G. Larson, *The scaling of zero-shear viscosities of semidilute polymer solutions with concentration.* Journal of Rheology, 2005. **49**(5): p. 1117-1128.
102. Dakhil, H., et al., *Buffered λ-DNA solutions at high shear rates.* Journal of Rheology, 2021. **65**(2): p. 159-169.
103. Pan, S., et al., *Shear thinning in dilute and semidilute solutions of polystyrene and DNA.* Journal of Rheology, 2018. **62**(4): p. 845-867.
104. Bhattacharjee, P., et al., *Extensional rheometry of entangled solutions.* Macromolecules, 2002. **35**(27): p. 10131-10148.
105. Poole, R., *The deborah and weissenberg numbers.* Rheol. Bull, 2012. **53**(2): p. 32-39.
106. Dealy, J., *Weissenberg and Deborah numbers—their definition and use.* Rheol. Bull, 2010. **79**(2): p. 14-18.
107. Petrie, C.J. and M.M. Denn, *Instabilities in polymer processing.* AIChE Journal, 1976. **22**(2): p. 209-236.
108. Datta, S.S., et al., *Perspectives on viscoelastic flow instabilities and elastic turbulence.* arXiv preprint arXiv:2108.09841, 2021.

109. Yuan, C., et al., *Nonlinear effects of viscoelastic fluid flows and applications in microfluidics: A review.* Proceedings of the Institution of Mechanical Engineers, Part C: Journal of Mechanical Engineering Science, 2020. **234**(22): p. 4390-4414.
110. Rodd, L.E., et al., *The inertio-elastic planar entry flow of low-viscosity elastic fluids in micro-fabricated geometries.* Journal of Non-Newtonian Fluid Mechanics, 2005. **129**(1): p. 1-22.
111. Rodd, L., et al., *Role of the elasticity number in the entry flow of dilute polymer solutions in micro-fabricated contraction geometries.* Journal of Non-Newtonian Fluid Mechanics, 2007. **143**(2-3): p. 170-191.
112. Lanzaro, A. and X.-F. Yuan, *Effects of contraction ratio on non-linear dynamics of semi-dilute, highly polydisperse PAAm solutions in microfluidics.* Journal of non-newtonian fluid mechanics, 2011. **166**(17-18): p. 1064-1075.
113. Gulati, S., S.J. Muller, and D. Liepmann, *Flow of DNA solutions in a microfluidic gradual contraction.* Biomicrofluidics, 2015. **9**(5): p. 054102.
114. Hemminger, O.L., et al., *Flow pattern and molecular visualization of DNA solutions through a 4: 1 planar micro-contraction.* Journal of non-newtonian fluid mechanics, 2010. **165**(23-24): p. 1613-1624.
115. Gulati, S., S.J. Muller, and D. Liepmann, *Direct measurements of viscoelastic flows of DNA in a 2: 1 abrupt planar micro-contraction.* Journal of Non-Newtonian Fluid Mechanics, 2008. **155**(1-2): p. 51-66.
116. Li, Z., et al., *Non-linear dynamics of semi-dilute polydisperse polymer solutions in microfluidics: A study of a benchmark flow problem.* Journal of non-newtonian fluid mechanics, 2011. **166**(16): p. 951-963.
117. Ekanem, E.M., et al., *Signature of elastic turbulence of viscoelastic fluid flow in a single pore throat.* Physical Review E, 2020. **101**(4): p. 042605.
118. Kenney, S., et al., *Large Deborah number flows around confined microfluidic cylinders.* Rheologica Acta, 2013. **52**(5): p. 485-497.
119. Shi, X., et al., *Mechanisms of onset for moderate Mach number instabilities of viscoelastic flows around confined cylinders.* Rheologica Acta, 2015. **54**(9): p. 805-815.
120. Zhao, Y., A.Q. Shen, and S.J. Haward, *Flow of wormlike micellar solutions around confined microfluidic cylinders.* Soft Matter, 2016. **12**(42): p. 8666-8681.
121. Qin, B., et al., *Upstream vortex and elastic wave in the viscoelastic flow around a confined cylinder.* Journal of fluid mechanics, 2019. **864**.
122. Haward, S.J., et al., *Flow of wormlike micellar solutions around microfluidic cylinders with high aspect ratio and low blockage ratio.* Soft Matter, 2019. **15**(9): p. 1927-1941.
123. Varshney, A. and V. Steinberg, *Elastic wake instabilities in a creeping flow between two obstacles.* Physical Review Fluids, 2017. **2**(5): p. 051301.
124. Varshney, A. and V. Steinberg, *Elastic Alfven waves in elastic turbulence.* Nature communications, 2019. **10**(1): p. 1-7.

125. Kawale, D., et al., *Elastic instabilities during the flow of hydrolyzed polyacrylamide solution in porous media: effect of pore-shape and salt.* Soft matter, 2017. **13**(4): p. 765-775.
126. Frisch, U. and A.N. Kolmogorov, *Turbulence: the legacy of AN Kolmogorov*. 1995: Cambridge university press.
127. Pan, L., et al., *Nonlinear elastic instability in channel flows at low Reynolds numbers.* Physical review letters, 2013. **110**(17): p. 174502.
128. Bonn, D., et al., *Large velocity fluctuations in small-Reynolds-number pipe flow of polymer solutions.* Physical Review E, 2011. **84**(4): p. 045301.
129. McKinley, G.H., P. Pakdel, and A. Öztekin, *Rheological and geometric scaling of purely elastic flow instabilities.* Journal of Non-Newtonian Fluid Mechanics, 1996. **67**: p. 19-47.
130. Pakdel, P. and G.H. McKinley, *Elastic instability and curved streamlines.* Physical Review Letters, 1996. **77**(12): p. 2459.
131. Varchanis, S., et al., *Asymmetric flows of complex fluids past confined cylinders: A comprehensive numerical study with experimental validation.* Physics of Fluids, 2020. **32**(5): p. 053103.
132. Hopkins, C.C., S.J. Haward, and A.Q. Shen, *Tristability in viscoelastic flow past side-by-side microcylinders.* Physical Review Letters, 2021. **126**(5): p. 054501.
133. Haward, S.J., et al., *Bifurcations in flows of complex fluids around microfluidic cylinders.* Lab on a Chip, 2021.
134. de Blois, C., S.J. Haward, and A.Q. Shen, *Canopy elastic turbulence: spontaneous formation of waves in beds of slender microposts.* arXiv preprint arXiv:2208.07651, 2022.
135. Qin, B. and P.E. Arratia, *Characterizing elastic turbulence in channel flows at low Reynolds number.* Physical Review Fluids, 2017. **2**(8): p. 083302.
136. Jha, N.K. and V. Steinberg, *Elastically driven Kelvin–Helmholtz-like instability in straight channel flow.* Proceedings of the National Academy of Sciences, 2021. **118**(34).
137. Browne, C.A. and S.S. Datta, *Elastic turbulence generates anomalous flow resistance in porous media.* Science advances, 2021. **7**(45): p. eabj2619.
138. Haward, S.J., C.C. Hopkins, and A.Q. Shen, *Stagnation points control chaotic fluctuations in viscoelastic porous media flow.* Proceedings of the National Academy of Sciences, 2021. **118**(38).
139. Haward, S.J., C.C. Hopkins, and A.Q. Shen, *Asymmetric flow of polymer solutions around microfluidic cylinders: Interaction between shear-thinning and viscoelasticity.* Journal of Non-Newtonian Fluid Mechanics, 2020. **278**: p. 104250.
140. Walkama, D.M., N. Waisbord, and J.S. Guasto, *Disorder suppresses chaos in viscoelastic flows.* Physical review letters, 2020. **124**(16): p. 164501.

141. De, S., et al., *Lane change in flows through pillared microchannels.* Physics of Fluids, 2017. **29**(11): p. 113102.
142. Shi, X. and G.F. Christopher, *Growth of viscoelastic instabilities around linear cylinder arrays.* Physics of Fluids, 2016. **28**(12): p. 124102.
143. Gulati, S., et al., *Elastic secondary flows in sharp 90 degree micro-bends: A comparison of PEO and DNA solutions.* Journal of Rheology, 2010. **54**(2): p. 375-392.
144. Vossoughi, S. and F. Seyer, *Pressure drop for flow of polymer solution in a model porous medium.* Can. J. Chem. Eng.;(Canada), 1974. **52**(5).
145. Loutherback, K., et al., *Improved performance of deterministic lateral displacement arrays with triangular posts.* Microfluidics and nanofluidics, 2010. **9**(6): p. 1143-1149.
146. Al-Fandi, M., et al., *New design for the separation of microorganisms using microfluidic deterministic lateral displacement.* Robotics and computer-integrated manufacturing, 2011. **27**(2): p. 237-244.
147. Groisman, A. and S.R. Quake, *A microfluidic rectifier: Anisotropic flow resistance at low Reynolds numbers.* Physical review letters, 2004. **92**(9): p. 094501.
148. Sousa, P.C., et al., *High performance microfluidic rectifiers for viscoelastic fluid flow.* RSC advances, 2012. **2**(3): p. 920-929.
149. Sousa, P., et al., *Efficient microfluidic rectifiers for viscoelastic fluid flow.* Journal of non-Newtonian fluid mechanics, 2010. **165**(11-12): p. 652-671.
150. Kawale, D., J. Jayaraman, and P.E. Boukany, *Microfluidic rectifier for polymer solutions flowing through porous media.* Biomicrofluidics, 2019. **13**(1): p. 014111.
151. Xia, Y., et al., *Replica molding using polymeric materials: A practical step toward nanomanufacturing.* Advanced Materials, 1997. **9**(2): p. 147-149.
152. Bélanger, M.C. and Y. Marois, *Hemocompatibility, biocompatibility, inflammatory and in vivo studies of primary reference materials low-density polyethylene and polydimethylsiloxane: A review.* Journal of Biomedical Materials Research: An Official Journal of The Society for Biomaterials, The Japanese Society for Biomaterials, and The Australian Society for Biomaterials and the Korean Society for Biomaterials, 2001. **58**(5): p. 467-477.
153. Xia, Y. and G.M. Whitesides, *Soft Lithography.* 1998.
154. Zhou, J., A.V. Ellis, and N.H. Voelcker, *Recent developments in PDMS surface modification for microfluidic devices.* Electrophoresis, 2010. **31**(1): p. 2-16.
155. Wong, I. and C.M. Ho, *Surface molecular property modifications for poly(dimethylsiloxane) (PDMS) based microfluidic devices.* Microfluidics and Nanofluidics, 2009. **7**: p. 291-306.
156. Amiji, M. and K. Park, *Prevention of protein adsorption and platelet adhesion on surfaces by PEO/PPO/PEO triblock copolymers.* Biomaterials, 1992. **13**: p. 682-692.

157. Wu, M.H., et al., *Development of PDMS microbioreactor with well-defined and homogenous culture environment for chondrocyte 3-D culture.* Biomedical microdevices, 2006. **8**(4): p. 331-340.
158. Eddington, D.T., J.P. Puccinelli, and D.J. Beebe, *Thermal aging and reduced hydrophobic recovery of polydimethylsiloxane.* Sensors and Actuators, B: Chemical, 2006. **114**: p. 170-172.
159. Hung, L. and A. Lee, *Optimization of droplet generation by controlling PDMS surface hydrophobicity.* ASME International Mechanical …, 2004: p. 1-2.
160. *Dimeric Cyanine Nucleic Acid Stains*. 2000. p. 22-25.
161. Rye, H.S., et al., *Stable fluorescent complexes of double-stranded DNA with bis-intercalating asymmetric cyanine dyes: properties and applications.* Nucleic acids research, 1992. **20**: p. 2803-2812.
162. *Fluorescence SpectraViewer*, T. Scientific, Editor.
163. Ström, O.E., J.P. Beech, and J.O. Tegenfeldt. *Long DNA isolation and imaging using lateral displacement arrays integrated with DNA combing*. in *23rd International Conference on Miniaturized Systems for Chemistry and Life Sciences, MicroTAS 2019*. 2019. Chemical and Biological Microsystems Society.
164. Ström, O.E., J.P. Beech, and J.O. Tegenfeldt, *Short and Long-range cyclic patterns in flows of DNA solutions in microfluidic obstacle arrays.* arXiv preprint arXiv:2211.16294, 2022.
165. Volpatti, L.R. and A.K. Yetisen, *Commercialization of microfluidic devices.* Trends in biotechnology, 2014. **32**(7): p. 347-350.
166. Chin, C.D., V. Linder, and S.K. Sia, *Commercialization of microfluidic point-of-care diagnostic devices.* Lab on a Chip, 2012. **12**(12): p. 2118-2134.
167. Peeling, R.W., et al., *Rapid tests for sexually transmitted infections (STIs): the way forward.* Sexually transmitted infections, 2006. **82**(suppl 5): p. v1-v6.
168. Tran, S.H.T., *Deterministic Lateral Displacement for Cell Separation*. 2019, Lund University.
169. Iarko, V., et al., *Extension of nanoconfined DNA: Quantitative comparison between experiment and theory.* Physical Review E - Statistical, Nonlinear, and Soft Matter Physics, 2015. **92**: p. 1-8.
170. Hsieh, C.-c., A. Balducci, and P.S. Doyle, *Ionic Effects on the Equilibrium Dynamics of DNA Confined in Nanoslits.* 2008. **3**: p. 2-7.
171. Cooley, J.W. and J.W. Tukey, *An algorithm for the machine calculation of complex Fourier series.* Mathematics of computation, 1965. **19**(90): p. 297-301.